COMPUTATIONAL FLUID DYNAMICS SIMULATIONS OF WIND TURBINE PERFORMANCE AND WAKE CHARACTERISTICS

A Dissertation

by

MAOKUN YE

Submitted to the Graduate and Professional School of
Texas A&M University
in partial fulfillment of the requirements for the degree of

DOCTOR OF PHILOSOPHY

Chair of Committee,	Hamn-Ching Chen
Committee Members,	Sharath Girimaji
	Moohyun Kim
	Paul Cizmas
Head of Department,	Sharath Girimaji

August 2023

Major Subject: Ocean Engineering

ABSTRACT

In this work, Computational Fluid Dynamics (CFD) simulations are performed for three wind tunnel experiments, i.e., the NREL S826 airfoil experiment, the NTNU BT1 experiment, and the NTNU BT2 experiment by using two in-house CFD codes, ReFRESCO and FANS. In ReFRESCO simulations, the Reynolds-Averaged Navier Stokes (RANS) equations with the $k-\omega$ SST turbulence model are adopted and the Moving-Grid-Formulation (MVG) approach with a sliding interface technique is leveraged to handle the relative motion between the rotating hub and turbine blades and the stationary tower and nacelle. In FANS simulations, the RANS equations are solved with a two-layer $k-\epsilon$ turbulence closure, and the overset grid capability of the code is leveraged to deal with the relative motion between different grid blocks.

As a benchmark case, CFD simulations for a wing section of the NREL S826 airfoil under the Reynolds number (Re) of 1.0×10^5 at three different Angles of Attack (AoA) are performed by the two adopted CFD codes. The CFD-predicted surface pressure distributions along the chord are compared against the experimental data directly, and good agreement between the predictions and the measurement is achieved.

Then, to quantify the spatial and temporal discretization uncertainties in the simulations targeting the performance of the BT1 wind turbine, simulation matrices for ReFRESCO and FANS are respectively established by using systematically refined computational grids and different time increments. In all the computational grids, the wind turbine geometry is fully resolved, including the blades, hub, nacelle, and tower. An inlet velocity of 10 m/s and a tip speed ratio (TSR) of 6 are used for the verification study. Unsteady RANS simulations are performed. By applying a modern verification procedure to the numerical predictions, the spatial and temporal numerical uncertainties of the predicted thrust (C_T) and power (C_P) coefficients are determined. In addition, simulations are performed over a range of TSRs by the two CFD codes, and a validation study is carried out by comparing the CFD results to the experimental data.

Afterward, CFD simulations targeting the wake characteristics of the NTNU BT1 wind turbine

are performed by using ReFRESCO and FANS. In ReFRESCO simulations, a thorough verification and validation (V&V) study is performed first to quantify the numerical uncertainties in the CFD-predicted wake characteristics. A simulation matrix consisting of three systematically refined grids coupled with three different time increments is established. The numerical uncertainties for the predicted velocity and turbulent kinetic energy at different downstream locations are then obtained by applying a systematic verification procedure to the CFD results. Then, a validation study is carried out by comparing the CFD results against the experimental data. It is shown that the CFD predictions are in good agreement with the measurements. In FANS simulations, the results are directly compared against the measurements and other numerical results. In general, good agreement between the prediction and measurement is achieved while under-predictions in the turbulence levels are identified. In addition, the details of the wind turbine wake are visualized and discussed. It is found that the tower wake is skewed by the rotating turbine blades. As a result, the wake profiles at downstream locations are asymmetric. Further, the tower wake is carried upwards by the rotating blade wakes, and thus the location of the asymmetry peak at different downstream distances is changing. We therefore confirm that the asymmetry of the wake profile is physical and it is not a measurement error in the experiment as suspected by some researchers in previous studies.

Further, CFD simulations are performed for the NTNU BT2 experiment in which two wind turbines are tandemly arrayed. In both ReFRESCO and FANS simulations, the CFD-predicted wake characteristics are compared against the experimental data and with other representative numerical results. It was found that the CFD-predicted velocity profiles behind the downstream wind turbine are in generally good agreement with the experimental data. However, challenges are also identified in the predictions of turbulent fluctuation profiles.

Lastly, conclusions are drawn based on the results of the current study, and recommendations are proposed for future research.

DEDICATION

This Dissertation is dedicated to

my parents, Xiangjun Liu and Zhongbin Ye,
for their unswerving love and support;

and my wife, Wan Huang,
for her unwavering love and encouragement;

and my grandparents, Zhengxian Peng and Bisong Liu,
who have provided me with unconditional acceptance since I was born;

and my daughter, Congyu Ye,
who has pushed me beyond my limits and made me a better person since she was born.

ACKNOWLEDGMENTS

I cannot express enough thanks to my Ph.D. advisor and committee chair, Prof. Hamn-Ching Chen, for his invaluable guidance throughout the duration of my doctoral research. Without his sharp intuition and accurate judgment on the asymmetric wake profiles observed in the NTNU BT1 experiment, this work would not have even started.

I would like to extend my gratitude to my committee members, Prof. Sharath Girimaji, Prof. Moo-Hyun Kim, and Prof. Paul Cizmas, for generously offering their valuable time, suggestions, and excellent courses that greatly enhanced my understanding of my research.

I would also like to express my gratitude to Dr. Arjen Koop at MARIN and Dr. Guilherme Vaz at BlueOASIS for their guidance, suggestions, and assistance in the use of ReFRESCO. I learned a lot from every discussion with them.

Thanks to the High-Performance Research Computing (HPRC) center of Texas A&M University for their support of computational resources.

Last but not the least, I would like to thank my friends, the department faculty, and the staff for contributing to a great experience at Texas A&M University.

CONTRIBUTORS AND FUNDING SOURCES

Contributors

This work was supported by a dissertation committee consisting of Professor Hamn-Ching Chen, Sharath Girimaji, and Moo-Hyun Kim of the Department of Ocean Engineering, and Professor Paul Cizmas of the Department of Aerospace Engineering. The computational resource is granted by Texas A&M University High Performance Research Computing center. All work for the dissertation was completed by the student, under the advisement of Professor Hamn-Ching Chen of the Department of Ocean Engineering.

Funding Sources

There are no outside funding contributions to acknowledge related to the research and compilation of this document.

TABLE OF CONTENTS

Page

LIST OF FIGURES

FIGURE Page

LIST OF TABLES

TABLE Page

1. INTRODUCTION

1.1 Wind Turbine Aerodynamics

To be a major clean energy source that is expected to supply around one-third of the global electricity demand by 2050, power generated by wind will need a several-fold increase from the amount it generates today [7]. In an effort to meet this expectation, more wind farms need to be deployed both onshore and offshore.

In modern wind farms both onshore and offshore, wind turbines are grouped in clusters, and thus the wind turbines in a wind farm will be inevitably operating in the wakes of upstream turbines, as shown in Fig. 1.1. This phenomenon leads to a reduction of the power generation efficiency of the downstream wind turbines while increasing the fatigue loading on their blades, and eventually reduces the overall power generation of that wind farm [8]. Data has shown that the total power loss of a large wind farm is between 10% to 25% [9]. Therefore, to further reduce the levelized cost of energy (LCOE) of wind farms and to fulfill the potential of wind energy, more efficient wind turbines and wind farms need to be designed. To achieve this goal, accurate predictions of the wind turbine performance and wake characteristics are of primary importance since they form the backbone of wind farm layout optimizations.

However, due to the multi-scale nature of the wind turbine flow, from mesoscale processes which is in the order of 100 to 1000 km to turbine aerodynamics of 1 to 1000 m [7], a comprehensive understanding of the wind turbine flow is still challenging. This complexity is further amplified in two partially connected trends. The first one is that the commercial turbine blades are increasingly larger, slender, and lighter, and thus the blades may have larger deformation during operation [10]. The second trend is the rapidly growing offshore wind market and the maturing of floating offshore wind turbines (FOWTs), in that additional degrees of freedom will be experienced by the wind turbine blades in the sea environment [11].

In general, a horizontal-axis wind turbine will affect the airflow around it both in the upstream

Figure 1.1: Wake turbulence in Horns Rev offshore wind farm, Denmark. Reprinted from [1].

and downstream directions. The upwind flow region influenced by a HAWT is known as the induction region, and it is characterized mainly by a reduction of wind speed [12]. The airflow downstream of a HAWT is called turbine wake, and it is characterized by a decreased wind velocity and an increased level of turbulence compared to the free stream condition [13]. Furthermore, the turbine wake can be subdivided into two regions: 1) the near-wake region in which the flow structures can be affected by the turbine geometries, i.e. the blades, hub, nacelle, and tower; and 2) the far-wake region where the flow characteristics are mainly dominated by global HAWT parameters, i.e. the thrust and power coefficients [14].

As an effort to contribute to shed more light on the complicated wind turbine aerodynamics, in the current work, state-of-the-art Computational Fluid Dynamics (CFD) techniques will be leveraged to simulate the performance and the wake characteristics of a single wind turbine and two in-line arrayed wind turbines.

1.2 Literature Review

In the past several years, CFD methods with different levels of complexity and accuracy were developed for wind engineering applications and have been extensively used in the predictions of wind turbine wakes. Due to the multi-scale nature of the wind turbine wakes, simultaneously revolving the blade boundary layers and the wake regions is challenging. In this section, existing literature will be reviewed and grouped into two major categories according to the way the boundary layers of wind turbines were handled in the CFD simulations.

1.2.1 CFD Simulations with Simplified Rotor Models

As mentioned earlier, simultaneously revolving the blade boundary layers and the wake is resource-demanding in CFD simulations. To circumvent this difficulty, the blade element method (BEM) and its improved methods [15, 16], i.e., the actuator disc (AD) [17, 18], and the actuator line (AL) [19, 20] methods, have been leveraged in the CFD simulations. In those approaches, the rotating blades were simplified as equivalent forces acting in the fluid field. Then, those models were coupled with the Reynolds-Averaged Navier-Stokes (RANS) or Large Eddy Simulation (LES) solvers to calculate the airflow around the wind turbines.

This category of approaches has been extensively used in the analysis of wind turbine aerodynamics including the wake generated from single or two turbines [21–25], wind turbine arrays or wind farms [13, 26–29], floating offshore wind turbines (FOWTs) [30–32], the interaction between wind turbine wake and the atmospheric boundary layers [9, 33–38], etc. To account for the effects of the nacelle and the tower, immersed boundary method (IB) was also integrated into the BEM-RANS/LES simulations [6, 39].

However, due to the embedded assumptions of the BEM-based methods, e.g., the flow on the blade surface is two-dimensional, the credibility of this approach is questioned in real-world applications where the flow in the vicinity of the blades is three-dimensional [40, 41]. Especially for FOWTs, the disadvantage of this approach is more prominent due to the fact that the three-dimensional nature of the airflow around the rotor cannot be neglected [42], and as a result, the

details of the flow in the vicinity of the blades are of importance to the accurate predictions of the wind turbine performance, the platform response, and the turbine-generated wakes.

1.2.2 CFD Simulations with Fully-Resolved Rotor Geometry

With the continual decrease of computational cost in recent years, wind turbine simulations with fully resolved geometries have become more popular [40, 43–47]. This approach is in particular preferable in situations where the flow details in the vicinity of the wind turbines are critical [48–52].

In addition, scholars have demonstrated that the effect of the tower and the rotor-tower interaction is not negligible on the wake characteristics of a wind turbine [53–57], thus correctly resolving the rotor and tower geometries is necessary. Gómez and Seume [58] clearly showed the effect of the rotating blades on the tower wake by using a two-dimensional RANS calculation. It was found that due to the rotation of the turbine blades, the tower wake was skewed, and this phenomenon cannot be accounted for by using traditional BEM methods. Later, by adopting fully resolved rotor and tower geometries in CFD simulations, the interactions between the rotor and tower wakes were further elucidated for both upwind [59, 60] and downwind [61–65] types of HAWTs.

1.3 Objectives of this Dissertation

Floating Offshore Wind Turbines (FOWTs) are complex structures and the structure of the airflow around the FOWTs is complicated. The modeling of the FOWTs depends on the researchers' perspective. Researchers from ocean engineering treat the modeling problem, naturally, as an extension of offshore oil and gas applications focusing primarily on the dynamics of FOWTs. In those research works, airflow in the vicinity of wind turbines is of interest while the turbine wakes are not resolved. On the contrary, in the wind energy community, the most concerning part of this problem is the modeling of the wake generated by wind turbines and the overall efficiency of wind farms. This is crucial because offshore wind energy faces intensive competition from other energy industries thus the prediction of the efficiency of an offshore wind farm is of primary interest. Therefore, flow in the wake regions needs to be resolved while simplified rotor models are often

used to circumvent the difficulty of resolving rotor boundary layers.

However, both aforementioned perspectives may not be sufficient to model the airflow in an offshore wind farm. On one hand, the airflow around a FOWT needs to be precisely resolved in order to perform an accurate analysis for the aerodynamics of the FOWT in the ocean environment [66–69], i.e. waves and currents. Under certain conditions, the turbine blades will even operate in their own wake due to the platform motions [41, 70, 71]. On the other hand, wake characteristics in the far wake also need to be resolved and the interactions between upstream and downstream turbines need to be understood since it forms the backbone of wind farm layout optimization algorithms.

As the first step to closing this gap, the current work will aim at the aerodynamics of FOWTs. High-fidelity and trustworthy CFD simulations with fully resolved turbine geometries will be performed for two wind tunnel experiments by leveraging state-of-the-art CFD approaches, i.e., the sliding mesh and overset-grid techniques. The goal of this work is to improve the understanding of the wake development of a single wind turbine and the wake interactions between two tandemly arrayed wind turbines. Particularly, the proposed research has the following sub-objectives:

- To quantify the numerical uncertainties in the CFD simulations of wind turbine performance;
- To quantify the numerical uncertainties in the CFD simulations of wind turbine wake characteristics;
- To illustrate the underlying mechanisms of the asymmetric wake profiles in the selected wind tunnel experiments.
- To provide a better understanding of the interaction between two wind turbine wakes.

1.4 Dissertation Organization

The following chapters of this dissertation are organized as follows.

Chapter 2 introduces the numerical methods, i.e., the governing equations, the turbulence models, the two flow solvers used in the simulations, and the verification and validation (V&V) proce-

dure adopted in the current work.

Chapter 3 describes the test cases adopted in the current work, including the three wind tunnel experiments performed at the Norwegian University of Science and Technology (NTNU), i.e., the NTNU Blind Test 1 and 2 experiments, and the NREL S826 airfoil experiment.

Chapter 4 presents the CFD results of the NREL S826 airfoil experiment by using ReFRESCO and FANS. As a benchmark case, CFD simulations for the S826 airfoil at different Angles of Attack (AoA) are performed prior to the calculations for the NTNU BT1 turbine, and the results are validated against the experimental data.

Chapter 5 shows the results of the V&V study targeting the CFD-predicted performance, i.e., the thrust and power coefficients, of the NTNU BT1 wind turbine. By using both ReFRESCO and FANS, simulations of the BT1 wind turbine at the tip speed ratio (TSR) of 6 are performed by using a matrix with 16 cases established by using 4 systematically refined grids and 4 different time increments. The adopted verification procedure is then applied to the CFD results and the total numerical uncertainty is obtained. That numerical uncertainty is then applied to the simulations of the BT1 wind turbine over a range of TSR values and the thrust and power coefficients are validated against the experimental data.

Chapter 6 presents the CFD simulations targeting the wake characteristics of the NTNU BT1 wind turbine by using ReFRESCO and FANS. The computational domain and grid strategy, the numerical settings in both solvers are described in detail, and the flow details are shown and discussed.

Chapter 7 shows the CFD results of the NTNU BT2 experiment in which two wind turbines are placed in line. CFD simulations under three different operating conditions are performed by using both ReFRESCO and FANS. The performance of both the upstream and downstream wind turbines and the wake characteristics behind the downstream wind turbine are shown and discussed in detail.

Finally, chapter 8 summarizes the current work and draws conclusions according to the CFD simulations and results.

2. METHODOLOGY

2.1 Reynolds-Averaged Navier-Stokes Equations

In the present study, the incompressible Reynolds-Averaged Navier-Stokes (RANS) equations are solved in the simulations:

$$\nabla \cdot \vec{V} = 0 \tag{2.1}$$

$$\frac{\partial \vec{V}}{\partial t} + \nabla \cdot \left(\vec{V}\vec{V}\right) = \nabla \cdot \left[(\nu + \nu_t)\left(\nabla \vec{V} + (\nabla \vec{V})^T\right)\right] - \nabla\left(\frac{p}{\rho} + \frac{2}{3}k\right) + \vec{B} \tag{2.2}$$

where $\vec{V}$ represents the velocity field, t the time, ρ the density, p the pressure, $\vec{B}$ the body force vector, and k the turbulence kinetic energy. ν denotes the kinematic viscosity of air, and ν_t is the so-called eddy viscosity.

2.2 Flow Solvers

Two CFD solvers will be adopted in the simulations of the current work, i.e. ReFRESCO and FANS. Introductions to those two CFD solvers are provided in this section.

2.2.1 ReFRESCO

ReFRESCO (www.refresco.org) is a multi-phase viscous CFD code developed by Maritime Research Institute Netherlands (MARIN). The code solves unsteady incompressible flows using the Navier-Stokes equations, and the Finite-Volume Method (FVM) is used in the discretization of the equations. Turbulence closure models based on the Reynolds-Averaged Navier-Stokes (RANS), Detached Eddy Simulation (DES), Partially-Averaged Navier-Stokes (PANS), and Large Eddy Simulation (LES) can be used in ReFRESCO. The code is parallelized and can run on high-performance computation (HPC) clusters.

2.2.1.1 Rotor Motion Handling in ReFRESCO

The rotating wind turbine is handled by leveraging the Moving-Grid-Formulation (MVG) method with a sliding interface technique. For the MVG approach, the integral form of the RANS equations that are applied to a control volume are written as:

$$\int_{\mathcal{S}} \left(\vec{V} - \vec{V}_g\right) \cdot \vec{n}\, d\mathcal{S} = 0 \tag{2.3}$$

$$\begin{aligned}\int_{\mathcal{V}} \frac{\partial \vec{V}}{\partial t}\, d\mathcal{V} + \int_{\mathcal{S}} \left[\vec{V}\left(\vec{V} - \vec{V}_g\right) \cdot \vec{n}\right]\, d\mathcal{S} = \int_{\mathcal{S}} (\nu + \nu_t) \left[\left(\nabla\vec{V} + \nabla\vec{V}^T\right)\right] \cdot \vec{n}\, d\mathcal{S} \\ - \int_{\mathcal{V}} \nabla\left(\frac{p}{\rho} + \frac{2}{3}k\right)\, d\mathcal{V} + \int_{\mathcal{V}} \vec{B}\, d\mathcal{V}\end{aligned} \tag{2.4}$$

where $\vec{V}_g$ is the motion of grid. In the MVG method, all the variables are defined in the earth-fixed reference system.

2.2.2 FANS

The Finite-Analytic Navier-Stokes (FANS) code is developed by Dr. Hamn-Ching Chen and his research group at Texas A&M University [72, 73]. The code solves the unsteady incompressible Navier-Stokes equations by using the Finite-Analytic method [74] and is integrated with overset-grid capability.

2.2.2.1 Rotor Motion Handling in FANS

The FANS code is integrated with overset-grid capability. The relative motion among different computational blocks can be achieved by moving arbitrary blocks and the flow information can be exchanged among the blocks through interpolation.

2.3 Turbulence Closure Models

In Eq. (2.2), ν_t is the eddy viscosity in the Boussinesq hypothesis and it is obtained by solving two additional transport equations in two-equation turbulence models. In the current work, two

different two-equation models are used by ReFRESO and FANS, respectively, to close the RANS equations, i.e., the $k-\omega$ SST model and the two-layer $k-\epsilon$ model.

2.3.1 $k-\omega$ SST Model

In ReFRESCO, the $k-\omega$ SST model [75] is used for turbulence closure. The two additional transport equations for the turbulence kinetic energy k and specific dissipation rate ω are shown as follows:

$$\frac{\partial \rho k}{\partial t}+\frac{\partial}{\partial x_j}(\rho U_j k)=\tilde{P}_k-\beta^*\rho k\omega+\frac{\partial}{\partial x_j}\left[(\mu+\sigma_k\mu_t)\frac{\partial k}{\partial x_j}\right] \tag{2.5}$$

$$\frac{\partial \rho \omega}{\partial t}+\frac{\partial}{\partial x_j}(\rho U_j \omega)=P_\omega-\beta\rho\omega^2+\frac{\partial}{\partial x_j}\left[(\mu+\sigma_\omega\mu_t)\frac{\partial \omega}{\partial x_j}\right]+2\rho(1-F_1)\frac{\sigma_{\omega 2}}{\omega}\frac{\partial k}{\partial x_j}\frac{\partial \omega}{\partial x_j} \tag{2.6}$$

where $\tilde{P}_k$ is the corrected production term of k defined by:

$$\tilde{P}_k=\min(P_k,10\beta^*\rho k\omega) \tag{2.7}$$

with

$$P_k=\mu_t\frac{\partial U_i}{\partial x_j}\left(\frac{\partial U_i}{\partial x_j}+\frac{\partial U_j}{\partial x_i}\right) \tag{2.8}$$

and P_k is the production term of ω defined by:

$$P_\omega=\frac{\alpha}{\nu_t}P_k \tag{2.9}$$

F_1 is the blending function which is defined by:

$$F_1=\tanh\left\{\left\{\min\left[\max\left(\frac{\sqrt{k}}{\beta^*\omega d},\frac{500\nu}{d^2\omega}\right),\frac{4\rho\sigma_{\omega 2}k}{CD_{k\omega}d^2}\right]\right\}^4\right\} \tag{2.10}$$

where

$$CD_{k\omega} = \max\left(2\rho\sigma_{\omega 2}\frac{1}{\omega}\frac{\partial k}{\partial x_i}\frac{\partial \omega}{\partial x_i}, 10^{-10}\right) \tag{2.11}$$

and d is the distance to the nearest wall. Note that F_1 switches from 1 to 0 while the distance to the wall increases, and the behavior of the turbulence model changes from the $k-\omega$ to $k-\epsilon$ accordingly.

All the constants in above equations are derived from blending corresponding constants of the standard $k-\epsilon$ and the $k-\omega$ turbulence models as follows,

$$\alpha = F_1\alpha_1 + (1-F_1)\alpha_2 \tag{2.12}$$

$$\beta = F_1\beta_1 + (1-F_1)\beta_2 \tag{2.13}$$

$$\sigma_k = F_1\sigma_{k1} + (1-F_1)\sigma_{k2} \tag{2.14}$$

$$\sigma_\omega = F_1\sigma_{\omega 1} + (1-F_1)\sigma_{\omega 2} \tag{2.15}$$

where $\beta^* = 0.09$, $\alpha_1 = 5/9$, $\beta_1 = 0.075$, $\sigma_{k1} = 0.85$, $\sigma_{\omega 1} = 0.5$, $\alpha_2 = 0.44$, $\beta_2 = 0.0828$, $\sigma_{k2} = 1.0$, and $\sigma_{\omega 2} = 0.856$.

Finally, the eddy viscosity ν_t is defined by:

$$\nu_t = \frac{a_1 k}{\max(a_1\omega, F_2\Omega)} \tag{2.16}$$

where $a_1 = 0.31$, and F_2 is a second blending function and is defined by:

$$F_2 = \tanh\left\{\left[\max\left(\frac{2\sqrt{k}}{\beta^*\omega d}, \frac{500\nu}{d^2\omega}\right)\right]^2\right\} \tag{2.17}$$

and Ω is the absolute value of vorticity.

2.3.2 Two-Layer $k-\epsilon$ Model

In FANS, the two-layer $k-\epsilon$ model is used in the simulations. The two-layer $k-\epsilon$ is proposed by Chen and Patel [76]. In the outer layer, i.e., the region away from the wall, the standard $k-\epsilon$ turbulence model [77, 78] is used.

$$\frac{\partial k}{\partial t} + U_j \frac{\partial k}{\partial x_j} = P_k - \epsilon + \frac{\partial}{\partial x_j}\left[\left(\nu + \frac{\nu_t}{\sigma_k}\right)\frac{\partial k}{\partial x_j}\right] \tag{2.18}$$

$$\frac{\partial \epsilon}{\partial t} + U_j \frac{\partial \epsilon}{\partial x_j} = C_{\epsilon 1}\frac{\epsilon}{k}\tau_{ij}\frac{\partial U_i}{\partial x_j} - C_{\epsilon 2}\frac{\epsilon^2}{k} + \frac{\partial}{\partial x_j}\left[\left(\nu + \frac{\nu_t}{\sigma_\epsilon}\right)\frac{\partial \epsilon}{\partial x_j}\right] \tag{2.19}$$

where P_k is the rate of production of turbulent kinetic energy and is defined by:

$$P_k = \tau_{ij}\frac{\partial U_i}{\partial x_j} = \nu_t\left(\frac{\partial U_i}{\partial x_j} + \frac{\partial U_j}{\partial x_i}\right)\frac{\partial U_i}{\partial x_j} \tag{2.20}$$

and the values of the closure constants are $C_{\epsilon 1} = 1.44$, $C_{\epsilon 2} = 1.92$, $C_\mu = 0.09$, $\sigma_k = 1.0$, $\sigma_\epsilon = 1.3$.

In the inner layer, i.e., the region near the wall, the rate of energy dissipation ϵ is specified by an explicit algebraic relation as

$$\epsilon = \frac{k^{3/2}}{l_\epsilon} \tag{2.21}$$

and the eddy-viscosity is given by

$$\nu_t = C_\mu \sqrt{k} l_\mu \tag{2.22}$$

In Eqs. (2.21) and (2.22), l_ϵ and l_μ are the length scales of ϵ and ν_t, respectively, and is defined as and the eddy-viscosity is given by

$$l_\epsilon = C_l y\left[1 - \exp\left(\frac{-R_y}{A_\epsilon}\right)\right] \tag{2.23}$$

and

$$l_\mu = C_l y \left[1 - \exp\left(\frac{-R_y}{A_\mu}\right)\right] \tag{2.24}$$

where R_y is the turbulence Reynolds number defined by

$$R_y = \frac{\sqrt{k}y}{\nu} \tag{2.25}$$

and C_l is a constant which is defined as $C_l = \kappa C_\mu^{-3/4}$ with κ being the von Karman constant to achieve a smooth eddy-viscosity distribution at the connection between the inner and outer regions. A_μ is equal to 70 as a result of calibration to recover the log-law constant $B = 5.45$. Furthermore, $A_\epsilon = 2C_l$ is specified to maintain the proper asymptotic behavior of ϵ, i.e., $\epsilon = 2\nu k/y^2$, in the viscous sublayer.

2.4 Verification and Validation

In this section, the verification and validation (V&V) procedure adopted in the current work and its related concepts will be introduced in detail.

In order to get trustworthy solutions from CFD simulations, systematic V&V studies need to be performed to evaluate the numerical uncertainties of the results. Although they are frequently mentioned together, verification and validation are two distinct processes. Verification serves to show that the equations we chose are correctly solved, whereas validation serves to demonstrate whether the right equations are selected to characterize the problem by directly comparing the simulation results to the experimental data. Verification is strictly a mathematical exercise while validation is an engineering/science effort [79].

2.4.1 Numerical errors and uncertainties

The terms "numerical errors" and "numerical uncertainties" are closely related but conceptually different. The "error" is the difference between the simulation results and the "exact" solution, whereas the "uncertainty" defines an interval that contains the "exact" solution with a certain level

of confidence [80]. Here, under most circumstances, the "exact" solution is not known for fluid flow and thus a procedure to estimate it from the available simulation data is needed.

In general, there are three types of numerical errors present in a CFD calculation, which are round-off, iterative, and discretization errors [81]. Therefore, the total numerical error ϵ_n can be calculated as:

$$\epsilon_n = \epsilon_{ro} + \epsilon_{it} + \epsilon_d \tag{2.26}$$

The round-off error ϵ_{ro} comes with the fact that computers only have a finite floating-point precision, but it is assumed negligible when double-precision machines are used. The iterative error ϵ_{it} is the consequence of the nonlinearity of the governing equations, and it is also considered small when the solution is well converged. The discretization error ϵ_d, however, is the result of discretizing the governing partial differential equations into algebraic equations and is considered dominant among the numerical errors in CFD simulations.

The practice to quantify the numerical uncertainty related to the discretization error is called verification, in which the discretization uncertainty U_d of a result ϕ_i is estimated while the exact solution ϕ_0 is unknown [48].

2.4.2 Verification

The verification procedure adopted in this proposed research is proposed by Eça and Hoekstra [79]. For unsteady simulations, the discretization error can be expressed by a power series as:

$$\epsilon_d \simeq \delta_d = \phi_{ij} - \phi_0 = \alpha_x h_i^{p_x} + \alpha_t t_j^{p_t} \tag{2.27}$$

In the above equation, ϕ_{ij} represents a selected quantity obtained from the simulation using grid i and time increment j. ϕ_0 denotes the estimated "exact" solution obtained by fitting a set of ϕ_{ij} (e.g. ϕ_{11}, ϕ_{12}, and ϕ_{13}) in a certain manner. p_x and p_t are the observed orders of convergence in space and time, respectively. h_i is the relative grid size and t_j is the relative time increment. h_i

and t_i are defined as:

$$h_i = \left(\frac{N_{cell_1}}{N_{cell_i}} \right)^{\frac{1}{n_d}} \tag{2.28}$$

$$t_j = \frac{\Delta t_j}{\Delta t_1} \tag{2.29}$$

In Eqs. (2.28) and (2.29), N_{cell_i} denotes the number of cells in grid i, and Δt_j the time step size of the time increment j. The finest grid and time increment are denoted by subscript 1. Therefore, h_i and t_j are both equal to 1 for the simulation which uses the finest grid spacing and time step size. n_d represents the dimension of the calculation, i.e. $n_d = 3$ in the present study.

It should be pointed out that in Eq. (2.27) there exist 5 unknowns, thus at least 5 simulations with different pairs of h_i and t_j are required to determine those unknowns. However, more simulations are recommended to perform the error estimation by using the method of least-squares [79]. By using the method, ϕ_0, α_x, p_x, α_t, and p_t, are determined by minimizing the following equation:

$$S_{RE}\left(\phi_0, \alpha_x, p_x, \alpha_t, p_t\right) = \sqrt{\sum_{i=1}^{n_g} \sum_{j=1}^{n_t} w_{ij} \left[\phi_{ij} - \left(\phi_0 + \alpha_x h_i^{p_x} + \alpha_t t_j^{p_t}\right)\right]^2} \tag{2.30}$$

where n_g and n_t are respectively the number of grids and time increments used in the verification study. w_{ij} denotes the weight assigned to a given solution such that the relative importance of different pairs of h_i and t_j can be distinguished, e.g., larger weights are given to solutions obtained by finer sets of h_i and t_j. By solving Eq. (2.30), the estimated exact solution ϕ_0 can be obtained, and the standard deviation of the least-squares fit which will be used as a measure of the quality of the fitting procedure can be written as:

$$\sigma_d = \sqrt{\frac{\sum_{i=1}^{n_g} \sum_{j=1}^{n_t} n_g n_t w_{ij} \left[\phi_{ij} - \phi_0 + \alpha_x h_i^{p_x} + \alpha_t t_j^{p_t}\right]^2}{n_g n_t - 5}} \tag{2.31}$$

Further, a data range parameter is defined as:

$$\Delta_\phi = \frac{(\phi_{ij})_{max} - (\phi_{ij})_{min}}{n_g n_t - 1} \tag{2.32}$$

where $(\phi_{ij})_{max}$ and $(\phi_{ij})_{min}$ are the maximum and minimum values of ϕ_{ij} among all the simulations. The error estimation is considered reliable if $\sigma_d < \Delta_\phi$ is valid, and a safety factor $F_S = 1.25$ will be used. Else, a safety factor $F_S = 3$ will be used. Finally, the discretization uncertainty U_d can be calculated as follows,

For $\sigma_d < \Delta_\phi$,

$$U_d(\phi_{ij}) = F_S \epsilon_d(\phi_{ij}) + \sigma_d + |\phi_{ij} - \phi_{fit}| \tag{2.33}$$

For $\sigma_d \geq \Delta_\phi$,

$$U_d(\phi_{ij}) = F_S \frac{\epsilon}{\Delta_\phi} \left[\sigma_d(\phi_{ij}) + \sigma_d + |\phi_{ij} - \phi_{fit}|\right] \tag{2.34}$$

where ϕ_{fit} is the value obtained from the fitting procedure corresponding to the grid i and time increment j.

2.4.3 Validation

The validation procedure proposed by [82] is adopted in the validation study of this proposed research. In the procedure, the comparison error E_c is defined as:

$$E_c = \frac{\phi_{exp} - \phi_{ij}}{\phi_{exp}} \tag{2.35}$$

where ϕ_{exp} is the quantity of interest measured from experiments and ϕ_{ij} obtained by simulations. Eq. (2.35) represents the absolute difference between the simulation results and the experimental data.

Then, the validation uncertainty U_v which includes both experimental and numerical uncertainties is expressed as:

$$U_v^2 = U_{exp}^2 + U_{sim}^2 + U_{mod}^2 \tag{2.36}$$

If $|E_c| < U_v$, we then say that the validation is achieved at the U_v level. In Eq. (2.36), U_{exp} denotes the uncertainty of the experimentally-measured data while U_{sim} denotes the uncertainties in the numerical simulations and can be estimated from verification study. U_{mod} is the simulation modeling uncertainty arising from modeling assumptions and it is not practical to be estimated [82], hence will be neglected in this research. U_{exp} is determined typically by performing repeated experiments and provided by the experiment. However, this information is absent in the initial campaign of the NTNU BT1 and BT2 experiments, thus will not be taken into account in the validation study in the proposed research.

2.5 Chapter Summary

In this chapter, the methodologies, i.e., the governing equations, the flow lovers, the turbulence closure models used in the simulations, and the adopted V&V procedure are described.

3. TEST CASE DESCRIPTION

3.1 Overview

In the current work, three individual but related wind tunnel experiments performed at the Norwegian University of Science and Technology (NTNU) were adopted in the CFD simulations, i.e., the NREL S826 airfoil experiment [2], the NTNU Blind Test (BT) 1 experiment [3], and the NTNU BT2 experiment [4].

A series of wind tunnel experiments with different configurations and operating conditions was launched by NTNU in 2008. Blind comparison workshops, i.e., the NTNU BT workshops, were hosted before the data was released to find out how computational models would perform if only the geometry of the turbine was provided [3]. The NTNU BT workshops contain 5 individual experiments, i.e., wind tunnel tests for a single turbine, two in-line arrayed turbines, two in-line but offset turbines, two in-line turbines under different inflow conditions, and a yawed turbine. Compared to the other wind tunnel tests, the NTNU blind test series is preferable because it contains not only experiments for a single wind turbine but also experiments for two turbines, making it an ideal benchmark for numerical simulations aiming at wind turbine aerodynamics and has been widely adopted by researchers.

In the NTNU BT series, global performances, i.e., the thrust and power coefficients, as well as the wake characteristics of the turbines were recorded. However, the force distributions on the surfaces of the wind turbine blades were not directly measured. Therefore, considering the fact that the blades of the wind turbines use the NREL S826 airfoil along the entire span, later, a separate test specifically targeting the performance of the NREL S826 airfoil was conducted in the same wind tunnel at NTNU. This particular experiment is referred to as the NREL S826 airfoil experiment in the current work. The shape of the NREL S826 airfoil is shown in Fig. 3.1.

In the current work, for both ReFRESCO and FANS simulations, the NREL S826 airfoil experiment will be selected as the benchmark case and the CFD simulations targeting this experiment

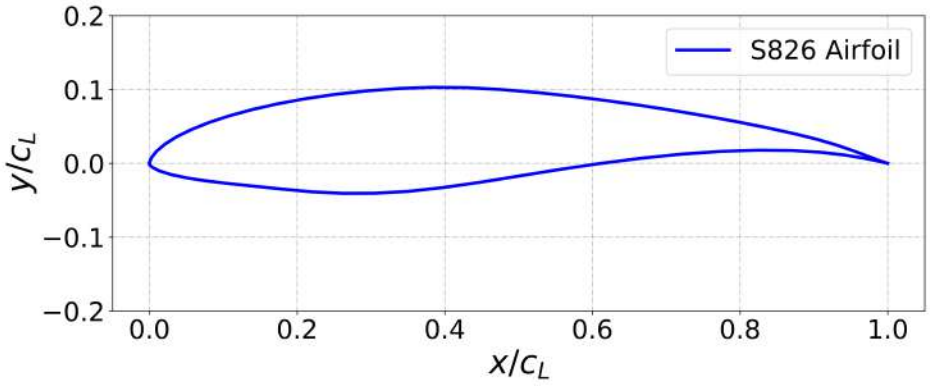

Figure 3.1: Shape of the NREL S826 airfoil.

will be performed first before we move further to the full turbine simulations.

3.2 NREL S826 Airfoil Experiment

First, as a benchmark case for both ReFRESCO and FANS simulations, CFD calculations are performed for the NREL S826 airfoil experiment [2].

3.2.1 Experiment Setup

In this experiment, a wing section of the S826 airfoil was placed in the NTNU closed-loop wind tunnel. The pressure distribution on the surface of the wing section was measured under different Angles of Attack (AoA) at different values of inflow velocity. The setup of the wing section in the wind tunnel experiment is shown in Fig. 3.2.

The chord length of the wing section, c_L, is 0.45 m and the total span length is 1.78 m. The pressure distribution on the middle wing section was measured at four values of AoA, i.e. $0°$, $4°$, $8°$, and $12°$, in the experiment. The authors argued that the errors in pressure measurement are within $\pm 0.03\%$. For each of the four AoA values, pressure measurements were performed for 8 different inflow conditions. The inflow velocity was increased from 1.47 m/s to 22.27 m/s and the corresponding turbulence intensity (TI) level dropped from 0.71% to 0.26%. As a result, the corresponding chord-based Reynolds numbers (Re) increased from 0.5×10^5 to 6.0×10^5. For more details on this experiment, the readers are encouraged to reference the original report [2].

Figure 3.2: Setup of the NREL S826 airfoil experiment, adopted from [2].

3.2.2 Simulation Conditions

In the experiment conducted by Bartl et al. [2], a wing section of the NREL S826 airfoil was tested in the NTNU wind tunnel. The pressure distribution on the wing section was measured under four different values of AoA, i.e. $0°$, $4°$, $8°$, and $12°$, with a range of Re from 0.5×10^5 to 6.0×10^5.

The purpose of performing simulations for the NREL S826 airfoil experiment is to provide additional validation for the verification and validation (V&V) study targeting the performance of the NTNU BT1 wind turbine. Therefore, in the simulations of the S826 airfoil, only CFD simulations with selected values of Re and AoA will be performed. The results from the CFD simulations will then be compared against the measurement. More details of the simulation conditions will be given in Chapter 4.

3.3 NTNU BT1 Experiment

In the NTNU BT1 experiment, a horizontal-axis wind turbine designed using the NREL S826 airfoil was evaluated in a closed-loop wind tunnel. Different wind turbine modeling strategies with varying accuracy were applied to the simulations of the wind turbine in previous studies.

The actuator line (AL) method coupled with LES solvers was adopted by many researchers in the simulations of NTNU BT1 turbine [3, 83, 84]. To capture the effect of the tower and nacelle, the immersed boundary (IB) method was leveraged and coupled with the traditional AL method in the LES calculations. Santoni et al. [39] performed LES simulations for the NTNU BT1 wind turbine. The authors leveraged the AL method to model the rotor blades and the IB method to model the tower and nacelle. Simulations were performed with and without the tower structure to highlight the tower effect. Ji et al. [6] developed a similar AL-IB method which was coupled with an LES solver to simulate the NTNU BT1 wind turbine. A good agreement between the CFD predictions and the measured data was achieved. In addition to LES, partially-averaged Navier-Stokes (PANS) equations were also used in the simulations of the BT1 turbine, and less computational resource was used in the PANS calculations than in LES [85]. RANS calculations with fully resolved geometries were also performed by researchers in the simulations of the NTNU BT1 wind turbine. Mittal et al. [86] performed CFD simulations for the turbine under three selected tip-speed ratios (TSR). In that study, the wind turbine geometries including the blades, nacelle, and tower were resolved and three different turbulence models were investigated. The temporal convergence of the simulations was also discussed. In addition, in a comparison study of several wind turbine modeling strategies using the NTNU BT1 turbine, Ye et al. [87] found that the tower effect was responsible for the asymmetry of the wake profiles behind the rotor. Other examples of the CFD simulations for this turbine with fully resolved geometries can be found in [88–90].

3.3.1 Experiment Setup

First, the definitions of the blades of the NTNU BT1 wind turbine are given in Table 3.1. It can be clearly seen that near the root of the blade, i.e., $0.1425\ m < r < 0.055\ m$, the twist angle (ϕ)

of the blade changes dramatically from approximately $40°$ to $20°$. This sudden change in ϕ makes the blade highly twisted.

Radius (r)	Chord Length (c)	Twist Angle (ϕ)
$[m]$	$[m]$	$[deg]$ ([°])
0.00750	0.013500	120.00
0.02250	0.013500	120.00
0.04900	0.013500	120.00
0.05500	0.049500	38.000
0.06750	0.081433	37.055
0.08250	0.080111	32.544
0.09750	0.077012	28.677
0.11250	0.073126	25.262
0.12750	0.069008	22.430
0.14250	0.064952	19.988
0.15750	0.061102	18.034
0.17250	0.057520	16.349
0.18750	0.054223	14.663
0.20250	0.051204	13.067
0.21750	0.048447	11.829
0.23250	0.045931	10.753
0.24750	0.043632	9.8177
0.26250	0.041529	8.8827
0.27750	0.039601	7.9877
0.29250	0.037831	7.2527
0.30750	0.036201	6.5650
0.32250	0.034697	5.9187
0.33750	0.033306	5.3045
0.35250	0.032017	4.7185
0.36750	0.030819	4.1316
0.38250	0.029704	3.5439
0.39750	0.028664	2.9433
0.41250	0.027691	2.2185
0.42750	0.026780	1.0970
0.44250	0.025926	-0.7167

Table 3.1: Definitions of chord length and twist angle as functions of blade radius of the NTNU BT1 wind turbine.

In the experiment, the total length and width of the wind tunnel are 11.15 m and 2.71 m, re-

spectively, and the height is $1.801m$ at the inlet and 1.851 m at the outlet. Note that the dimension of the wind tunnel is identical to the wind tunnel in which the NREL S826 experiment was performed. The rotor diameter is $D = 0.894\ m$ and the rotor axis is 0.817 m above the ground. The rotor center is placed at the center line of the wind tunnel and is 3.66 m away from the inlet. An illustration of the experimental setup is shown in Fig. 3.3. A uniform inflow velocity of 10 m/s and a turbulence intensity level (TI) of 0.3% were used, and the turbine was rotating at a range of TSR values from 1 to 12.

Figure 3.3: Setup of the NTNU BT1 experiment, adopted from [3].

3.3.2 Simulation Conditions

In the current work, two groups of simulations are performed for the NTNU BT1 experiment by using each of the two flow solvers, i.e., ReFRESCO and FANS.

The first group of simulations is a verification and validation (V&V) study which aims at the performance of the wind turbine, i.e., the thrust and the power coefficients, and thus the fine resolution of the computational cells close to the wind turbine will be achieved while the resolution in the wake regions will remain coarse. In this V&V study, first, numerical uncertainties of the CFD-

predicted turbine performances will be quantified through a systematic verification procedure at the TSR of 6. Then, a validation study will be conducted by performing CFD simulations at a range of TSR values, i.e., $1 - 12$, and comparing the CFD-predicted values against the experimental data considering the uncertainties obtained from the verification study. More details of the simulation conditions of this group of simulations will be given in Chapter 5.

The second group of simulations targets the wake characteristics of the wind turbine. In the wake simulations, the resolution of the computational cells in the near field of the wind turbine will be selected according to the performance V&V study. For ReFRESCO simulations, an additional V&V study aiming at the wake characteristics will be performed at $TSR = 6$ to determine the required resolution in space and time, and this knowledge will be inherited and thus the V&V study will not be repeated by using FANS. More details of the simulation conditions of this group of simulations will be given in Chapter 6.

3.4 NTNU BT2 Experiment

In the NTNU BT2 experiment, two horizontal-axis wind turbines were operating in line in the same wind tunnel at NTNU. The performances of the two turbines and the wake characteristics at three different downstream distances were measured and reported. The blades of the two wind turbines are identical, and they are the same as the blade geometry used in the BT1 experiment, while their nacelles and towers are different. And as a result, the rotor diameter of the upstream wind turbine is slightly larger than that of the downstream wind turbine. Note that the rotor diameter of the downstream wind turbine is the same as the one of the NTNU BT1 wind turbine.

Different wind turbine modeling strategies with varying accuracy were also applied to the simulations of the NTNU BT2 experiment in previous studies. In the original release of the results obtained from different research groups [4], distinct modeling strategies including steady RANS calculations using fully resolved rotor geometry, unsteady RANS calculations using Actuator Disc (AD) methods, LES simulations using Actuator Line (AL) methods, and free vortex wake simulations were leveraged in the studies. Considerable scatter in the numerical predictions obtained by different methods was identified.

Sreenivas et al. [91] performed detached eddy simulations (DES) for the NTNU BT2 experiment, and good agreement between the CFD prediction and experimental measurement was reported. Veisi and Mayam [92] investigated the effect of the rotational direction on the power efficiency of the downstream turbine in the NTNU BT2 experiment by using LES. It was observed that larger power efficiency was achieved when the downstream wind turbine was rotating in the opposite direction than in the same direction as the upstream wind turbine. Duan et al. [93] coupled an AL model with an LES solver and a good agreement between the CFD results and the experimental data was reported. Then, the same framework of simulation strategy was leveraged to investigate the wake interactions among 14 wind turbines.

3.4.1 Experiment Setup

The wind turbine geometry used in this research is described by Pierella et al. [4] in detail. The blades of both the upstream and the downstream turbines are constructed by using the NREL S826 airfoil along the entire span. Note that as mentioned earlier, the blades of the two wind turbines in the NTNU BT2 experiment are identical to the blade used in the BT1 experiment. The rotor diameter of the upstream turbine is 0.944 m and 0.894 m for the downstream turbine. The downstream wind turbine is placed at 3 D downstream of the upstream turbine, where D is defined as the rotor diameter of the downstream wind turbine, i.e., 0.894 m. The setup of the BT2 experiment is shown in Fig. 3.4.

3.4.2 Test Conditions

Three different operating configurations were tested in the BT2 experiment: 1) Test case A, in which the upstream wind turbine is operating at its design condition of $TSR = 6$ and the downstream wind turbine is operating at $TSR = 4$; 2) Test case B, in which the upstream turbine is operating at $TSR = 6$ while the downstream wind turbine is operating at $TSR = 7$; and 3) Test case C, in which the upstream turbine is still operating at $TSR = 6$ but the downstream wind turbine is operating at $TSR = 2.5$. All three cases will be simulated by using ReFRESCO while only test case A will be simulated by FANS in the current work. More details of the simulation

Figure 3.4: Setup of the NTNU BT2 experiment, adopted from [4].

conditions of this group of simulations will be given in Chapter 7.

3.5 Chapter Summary

In this chapter, the three wind tunnel experiments adopted in the current work, i.e., the NREL S826 airfoil experiment, the NTNU BT1 experiment, and the NTNU BT2 experiment, are introduced. The experimental setup of each of the experiments is described. The selected conditions under which the CFD simulations will be performed in the current work are also briefly described. More details will be given in the corresponding chapters.

4. CFD SIMULATIONS OF NREL S826 AIRFOIL *

In this chapter, CFD simulations using both ReFRESCO and FANS are performed aiming at the performance of the NREL S826 airfoil. As mentioned earlier, these simulations of the NREL S826 airfoil serve as the prerequisite and benchmark case for the verification and validation (V&V) study targeting the performance of the NTNU BT1 wind turbine. Therefore, only selected experimental configurations in the original report [2] are reproduced numerically in the current study by CFD calculations.

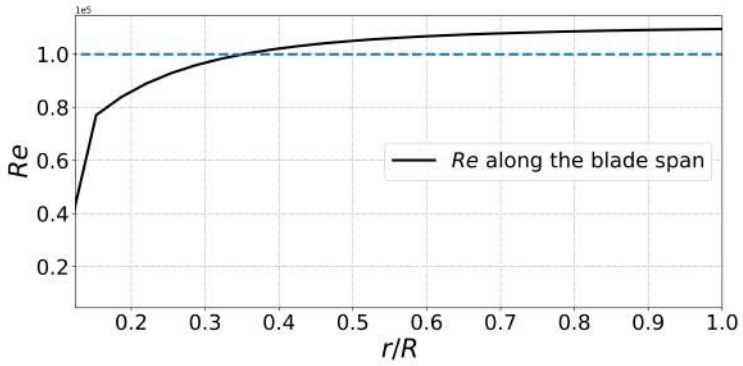

Figure 4.1: Re along the blades of NTNU BT1 wind turbine at $TSR = 6$.

It is worth emphasizing again that in the performance V&V study of the NTNU BT1 wind turbine, the rotor of the wind turbine rotating at the tip-speed ratio (TSR) of 6 is selected to be the representative operating condition. Therefore, the local Reynolds number (Re) and the Angle of Attack (AoA) of the turbine blades operating at $TSR = 6$ are plotted as functions of normalized radius r/R, as shown in Figs. 4.1 and 4.2, respectively. It can be observed that at $TSR = 6$, the value of Re for the majority of the blade span is approximately 1.0×10^5, and the range of AoA of the blades is roughly from $7°$ to $16°$.

*Reprinted with permission from "Verification and validation of CFD simulations of the NTNU BT1 wind turbine" by Ye, Maokun, Hamn-Ching Chen, and Arjen Koop, 2023. *Journal of Wind Engineering and Industrial Aerodynamics*, 234 (2023): 105336, Copyright [2023] by Elsevier.

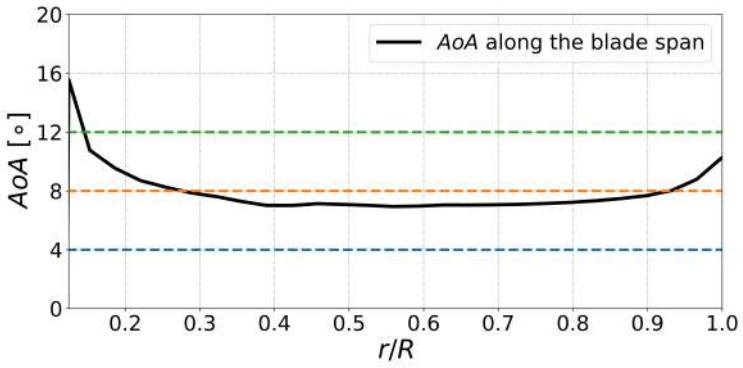

Figure 4.2: AoA along the blades of NTNU BT1 wind turbine at $TSR = 6$.

Because the BT1 wind turbine blades are designed using the NREL S826 airfoil along the entire span, in this chapter, CFD simulations under Re of 1.0×10^5 and AoA of $4°$, $8°$, and $12°$ will be performed by ReFRESCO and FANS. The results obtained in the CFD simulations will then be compared against the experimental measurement.

4.1 Computational Domain

The computational domain and the corresponding boundaries of this benchmark case to be used in both ReFRESCO and FANS simulations are illustrated in Fig. 4.3. The computational domain is designed to ensure that its outer boundaries match the wind tunnel walls in the NTNU S826 airfoil experiment.

4.2 ReFRESCO Simulations

In ReFRESCO simulations, the calculations performed for this benchmark case were run on the Terra cluster of the High Performance Research Computing (HPRC) at Texas A&M University (TAMU) using the Intel Xeon E5-2680 v4 2.40 GHz 14-core processors. For each of the simulations, 224 cores were used and the clock time was around 3 hours. More details of the computational resources consumed in the ReFRESCO simulations will be provided in Section 4.4.

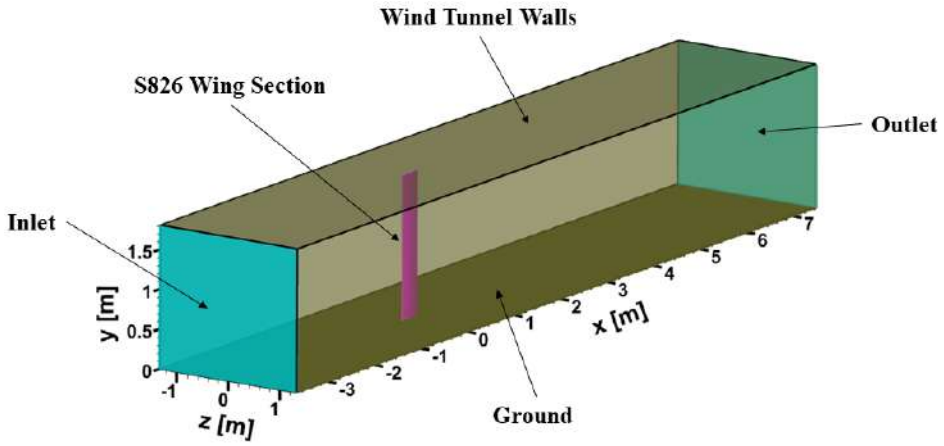

Figure 4.3: Illustration of the computational domain and its boundary names.

4.2.1 Computational Grids

For ReFRESCO simulations, hexahedral cells are generated in the computational domain. An illustration of the computational grid generated for the AoA of 12° is shown in Fig. 4.4. As can be observed in Fig. 4.4, three refinement boxes with increasing grid resolutions are used in order to generate finer computational cells near the surface of the wing section, while relatively coarser grid spacing is used in the far field. In addition, more levels of refinement are defined for the surface of the wing section. As shown in Fig. 4.5, the computational cells at the leading and trailing edges are further refined to capture the high curvature of the geometry. Viscous layers are inserted in the vicinity of the wing section wall with the criterion of non-dimensional wall distance $y^{+} < 1$, and the cell expansion ratio normal to the wall in the viscous layers is set to 1.2. The total number of cells in each of the computational grids used in the ReFRESCO simulations is approximately 4 million.

4.2.2 Numerical settings

In addition to the wind tunnel measurement, Bartl et al. [2] also performed simulations for the S826 airfoil over a range of different AoA, Re, and TI. Steady-state simulations were carried out and good agreement was found between the CFD predictions and the measured data. Oscillatory convergence was found only for the case in which the highest value of AoA (12°) combined

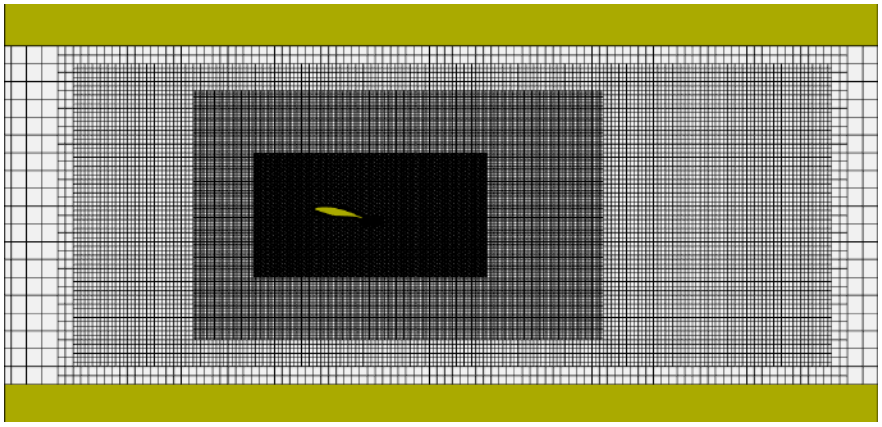

Figure 4.4: Mid-cross-section view of the computational grid for the S826 airfoil wing section. The AoA of the grid in this figure is $12°$.

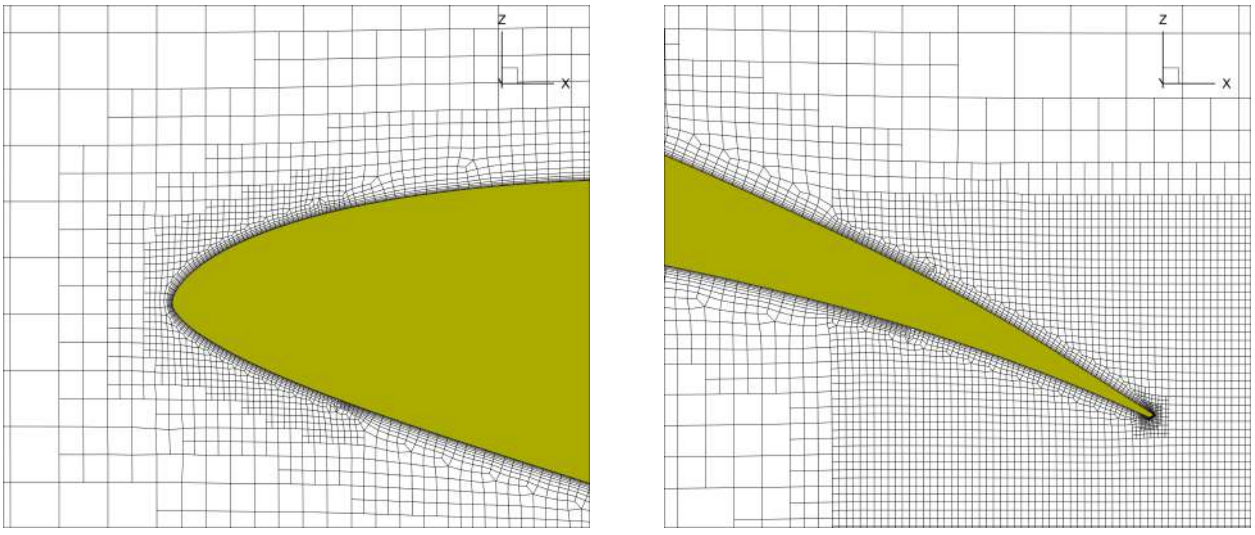

(a) Computational cells at the leading edge.

(b) Computational cells at the trailing edge.

Figure 4.5: Detail view near the leading edge and the trailing edge of the airfoil section.

with the lowest TI (0.22%) was used, while other cases were well converged. Therefore, in the current benchmark study, calculations are also carried out in a steady-state framework in order to reduce computational costs. The momentum and turbulence equations are discretized by using the HARMONIC scheme [94], and the FRESCO [95] algorithm in ReFRESCO is used for the mass-momentum coupling. The $k-\omega$ SST turbulence model is adopted in the current simulations, as described in Chapter 2. A uniform inflow velocity of 3.17 m/s and a TI of 0.7$\%$ are specified at the inlet boundary, as described in the experiment [2]. The fixed pressure boundary condition is applied to the outlet, and the no-slip condition is applied to all the wall boundaries including the wing section and the wind tunnel walls. The value of Re used in the present study is calculated based on the chord length of the wing section, which is approximately 1.0×10^5.

4.2.3 CFD Results

The normalized velocity magnitude contours (defined by U_{Mag}/U_{ref}) and the normalized pressure contours (defined by Eq. (4.1)) of the wing section at the mid-span are shown in Fig. 4.6.

On the contours of normalized velocity magnitude, which are the figures in the left column, the stagnation point is identified as a low-speed region at the leading edge of the airfoil. As the value of AoA increases from 4° to 12°, the stagnation point gradually moves towards the suction side. Further, at an AoA value of 12°, the airflow on the upper surface of the airfoil, i.e., the suction side, is more prominently accelerated than at an AoA value of 4°. In addition, it can be seen that the airflow is well attached to the surface at $AoA = 4^\circ$ while starting to separate from the surface at higher values of AoA.

On the normalized pressure contours, i.e., the figures on the right-hand side, the low-pressure region around the leading edge of the airfoil, becomes darker and larger while the value of AoA increases from 4° to 12°, meaning that the airfoil is generating more lift.

The pressure distributions at the mid-span of the wing section obtained from the CFD simulations are presented and compared against the experimental data, as shown in Fig. 4.7. Note that

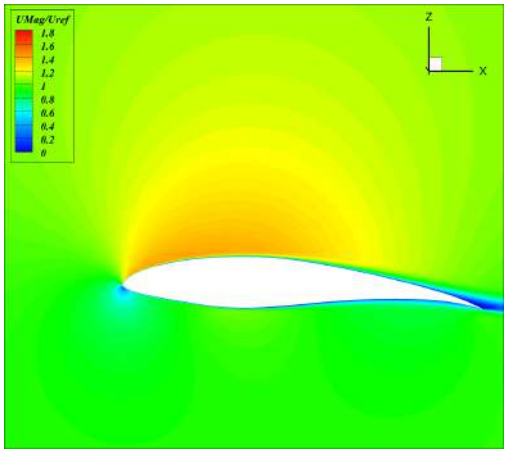

(a) U_{Mag}/U_{ref} contour at $AoA = 4°$

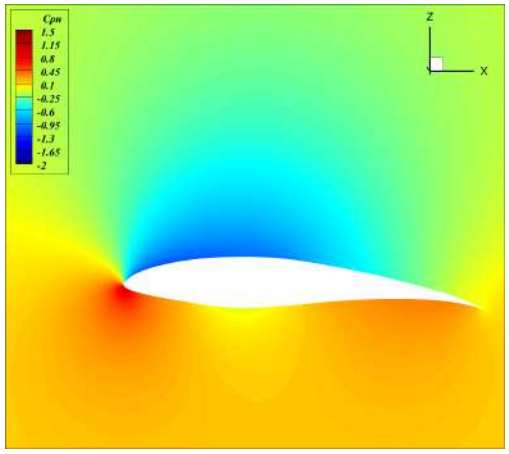

(b) C_{pn} contour at $AoA = 4°$

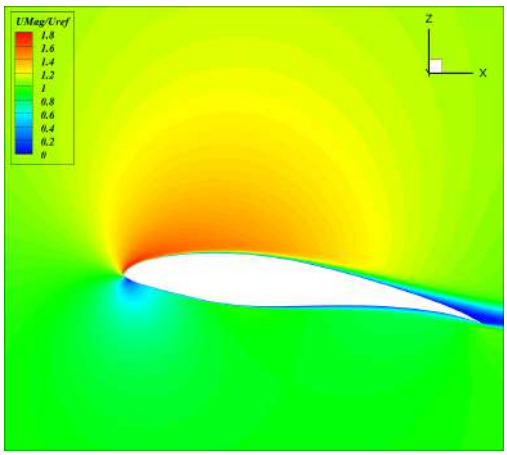

(c) U_{Mag}/U_{ref} contour at $AoA = 8°$

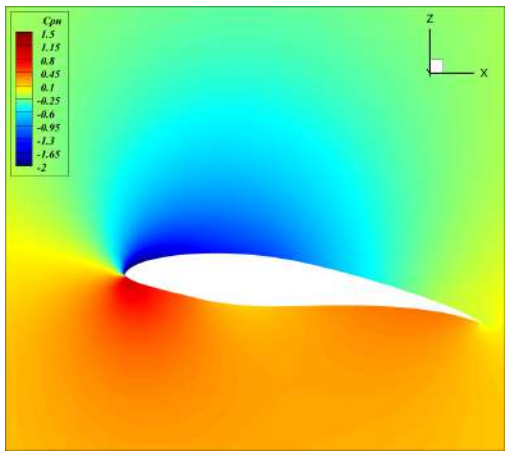

(d) C_{pn} contour at $AoA = 8°$

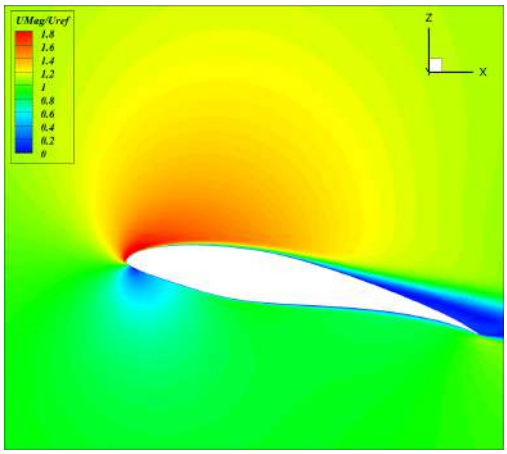

(e) U_{Mag}/U_{ref} contour at $AoA = 12°$

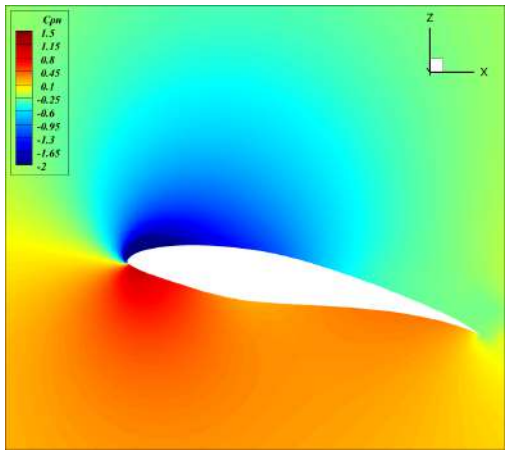

(f) C_{pn} contour at $AoA = 12°$

Figure 4.6: Normalized velocity magnitude contours (left column) and normalized pressure contours (right column) obtained from ReFRESCO simulations at the mid-span of the wing section for $Re = 1.0 \times 10^5$. The normalized velocity magnitude is defined by U_{Mag}/U_{ref} where U_{ref} is the inlet velocity. The normalized pressure is defined by Eq. (4.1).

C_{pn} is the pressure coefficient and is defined by the following equation:

$$C_{pn} = \frac{p}{\frac{1}{2}\rho U^2} \tag{4.1}$$

It can be observed that the CFD-predicted pressure distribution on the surface of the S826 airfoil is in good agreement with the measured data. Therefore, it can be concluded that the CFD code, ReFRESCO, used in this research is capable of accurately predicting the pressure on the surface of the S826 airfoil for the value of Re around 1.0×10^5.

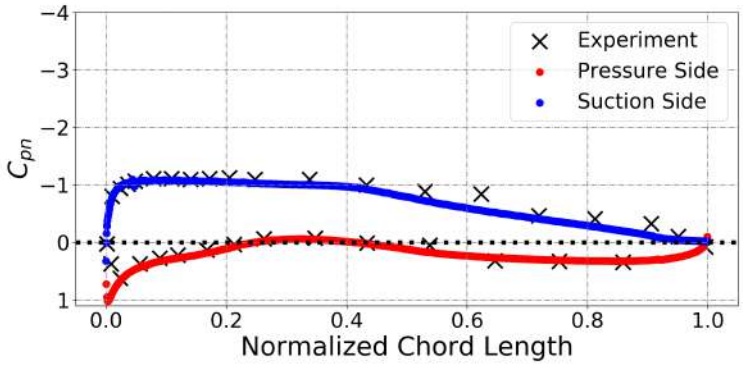

(a) $AoA = 4°$

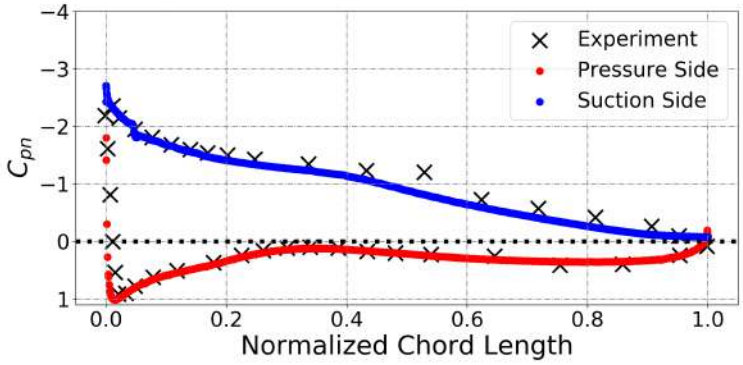

(b) $AoA = 8°$

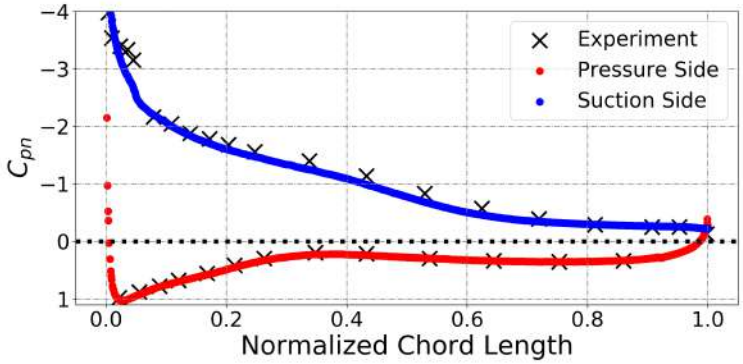

(c) $AoA = 12°$

Figure 4.7: Pressure distribution at the mid-span of the wing section under $Re = 1.0 \times 10^5$.

4.3 FANS Simulations

The simulations for this benchmark case were conducted on the Grace cluster of the HPRC at TAMU using the Intel Xeon 6248R (Cascade Lake) 3.0 GHz 24-core processors. For each simulation, 28 cores were requested and each simulation was completed within 4 hours. More details of the computational resources consumed in the FANS simulations will be provided in Section 4.4.

4.3.1 Computational Grids

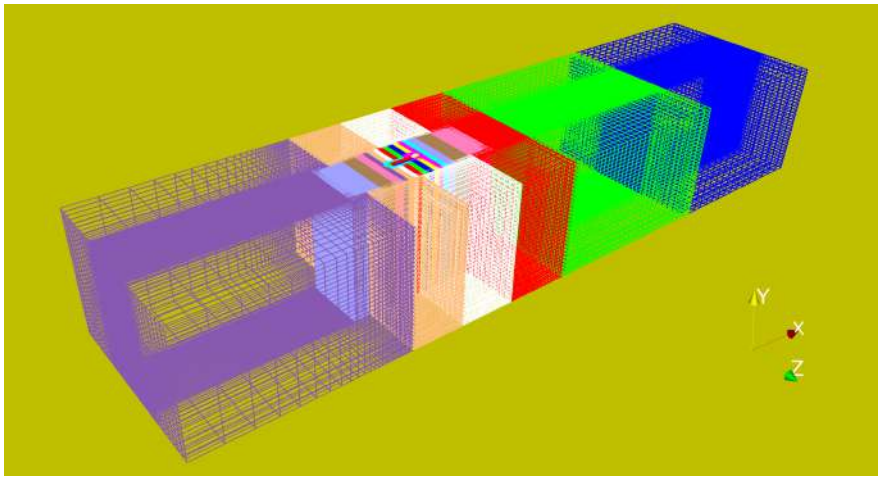

Figure 4.8: Overview of the overset grid of the S826 airfoil wing section used in FANS simulations. Different colors are used to distinguish the different grid blocks. The AoA of this example grid is $4°$.

For FANS simulations, structured overset grids are generated. An overview of the computational grids is shown in Fig. 4.8. Different colors were utilized to distinguish the different grid blocks. In the grid generation process, the following steps were followed:

1. Three mutually overlapped structured computational grid blocks are generated, i.e., the background block, the intermediate block, and the boundary-layer block. The boundary layer block is generated such that the thickness of the fist-layer cell satisfies the criterion of

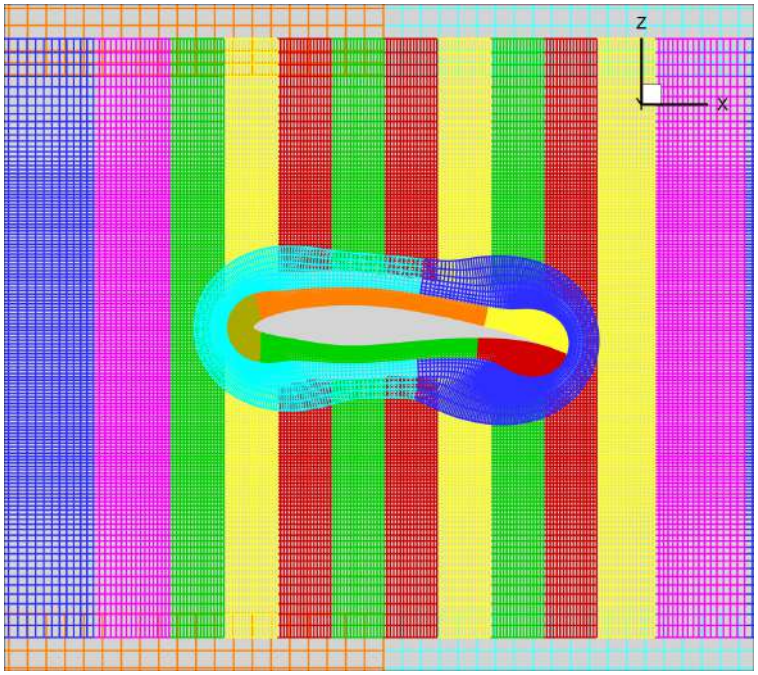

Figure 4.9: Detail view of the overset grid of the S826 airfoil wing section used in FANS simulations. Different colors are used to distinguish the different grid blocks. The AoA of this example grid is $4°$.

$y^+ < 1$, where y^+ is the non-dimensional wall distance. The cell expansion ratio normal to the wall in the boundary-layer block is set to 1.2.

2. The total number of processors to be used is determined. For example, in this case, in total 28 cores are used.

3. The three blocks are re-blocked to 28 smaller blocks and each small block has a similar number of grid points. By doing this, we can ensure that the processors will complete their calculations within a similar amount of computational time in parallel computations.

4. Boundary conditions for the 28 blocks are prepared separately.

5. The 28 computational blocks are distributed into the 28 processors for parallel computation.

Therefore, it can be observed that in Figs. 4.8 and 4.9, the original background block is re-blocked to 6 blocks, the original intermediate block is re-blocked to 15 blocks, and the original

boundary-layer block is re-blocked to 7 blocks. It is worth mentioning that in FANS simulations, computational grids at different values of AoA can be easily obtained by rotating the boundary-layer blocks. This is more efficient and time-conserving compared to the ReFRESCO simulations, in which computational grids at different AoA need to be generated respectively. The total number of grid points in each of the computational grids used in the FANS simulations is approximately 2 million.

4.3.2 Numerical settings

In FANS simulations of the NREL S826 airfoil, the two-layer $k-\epsilon$ turbulence model is adopted, as described in Chapter 2. A uniform inflow is specified at the inlet, and the linear-extrapolation boundary condition in FANS is specified at the outlet. No-slip condition is applied to the surface of the wing section, and a slip-wall condition is applied to the wind tunnel walls. The boundary condition for the surfaces of overset grid blocks that overlap with other blocks is set to "interior boundary surfaces". Interpolation will be performed using the flow information from the donor grids.

4.3.3 CFD Results

Just like in the previous ReFRESCO simulations, the normalized velocity magnitude contours and the normalized pressure contours obtained from FANS simulations are shown in Fig. 4.10. In general, both the velocity and the pressure fields at different AoA are smooth, demonstrating that the transfer of flow information among different overset computational grid blocks is working properly. Comparing Fig. 4.10 with Fig. 4.6, it can be seen that the contours obtained from FANS and ReFRESCO are similar.

The pressure distributions at different AoA on the surface of the mid-span of the wing section obtained from FANS simulations are shown in Fig. 4.11. Different colors are used to indicate the different grid blocks surrounding the wing section. It can be clearly seen that the pressure distributions on the surface of the wing section at all three values of AoA are smooth, suggesting that the flow information is exchanged correctly among those mutually overlapped grid blocks.

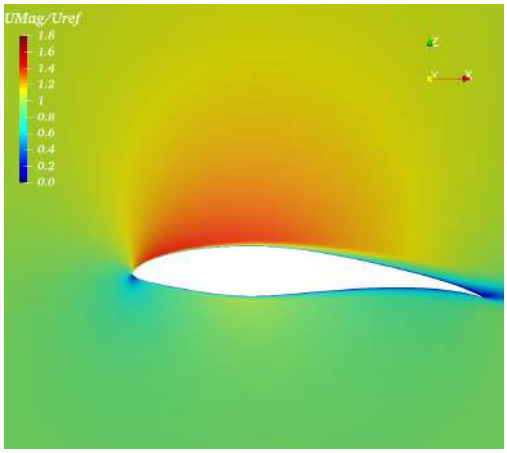

(a) U_{Mag}/U_{ref} contour at $AoA = 4°$

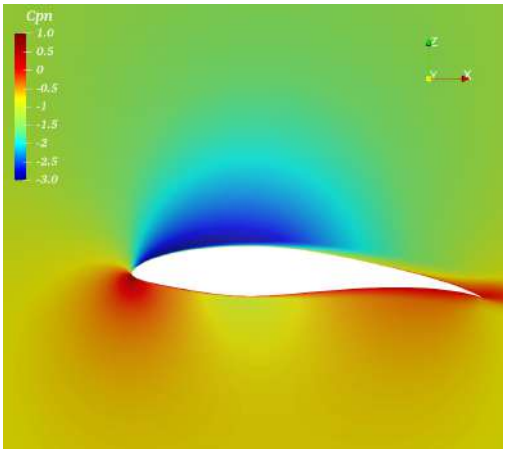

(b) C_{pn} contour at $AoA = 4°$

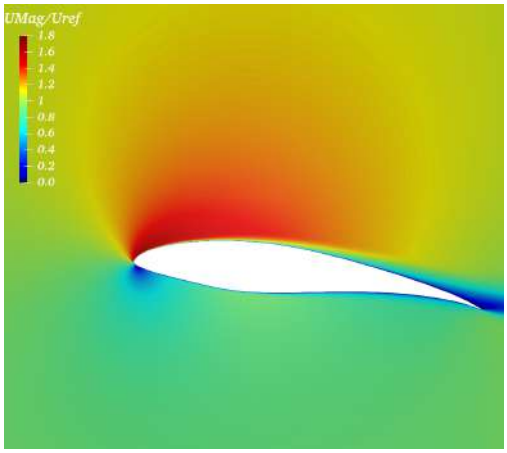

(c) U_{Mag}/U_{ref} contour at $AoA = 8°$

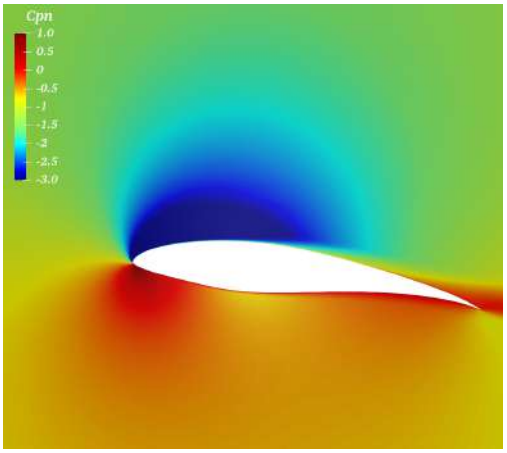

(d) C_{pn} contour at $AoA = 8°$

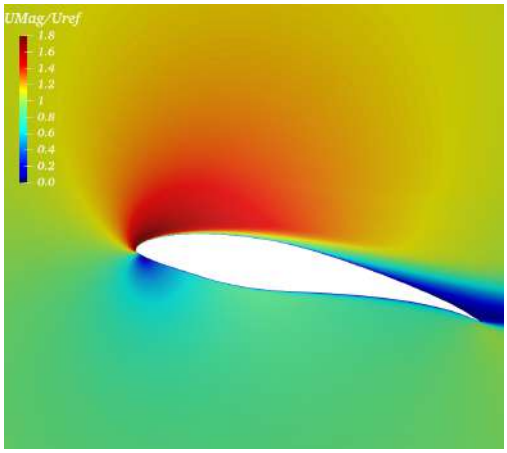

(e) U_{Mag}/U_{ref} contour at $AoA = 12°$

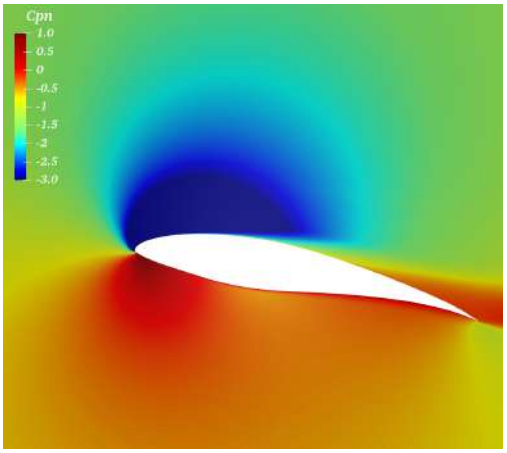

(f) C_{pn} contour at $AoA = 12°$

Figure 4.10: Normalized velocity magnitude contours (left column) and normalized pressure contours (right column) obtained from FANS simulations at the mid-span of the wing section for $Re = 1.0 \times 10^5$. The normalized velocity magnitude is defined by U_{Mag}/U_{ref} where U_{ref} is the inlet velocity. The normalized pressure is defined by Eq. (4.1).

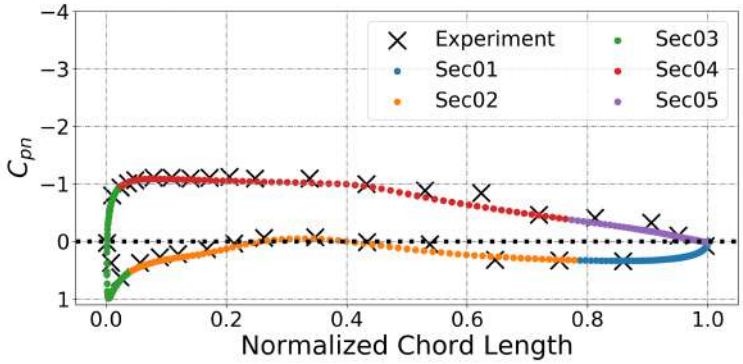

(a) $AoA = 4°$

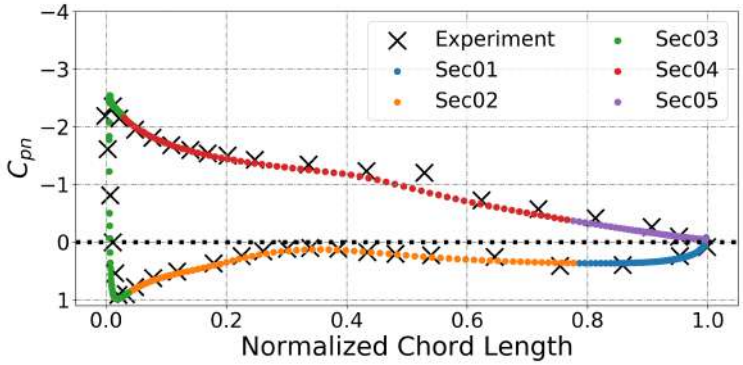

(b) $AoA = 8°$

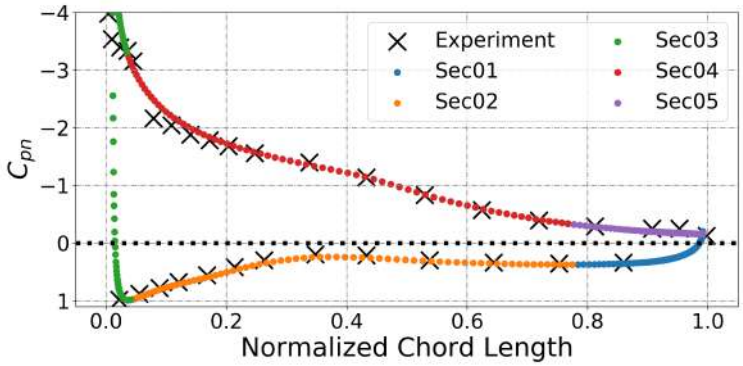

(c) $AoA = 12°$

Figure 4.11: Pressure distribution obtained from FANS simulations at the mid-span of the wing section under $Re = 1.0 \times 10^5$. Different colors are used to indicate the different grid blocks surrounding the wing section.

4.4 Chapter Summary

In this chapter, the numerical results of the NREL S826 experiment were obtained by the two CFD codes used in the current work, i.e., ReFRESCO and FANS. The simulations of the NREL S826 experiment will serve as a benchmark case for the following NTNU BT1 experiment. According to the operating conditions of the NTNU BT1 wind turbine, CFD simulations were performed under $Re = 1.0 \times 10^5$ at three different AoA values, i.e., $AoA = 4°$, $8°$, and $12°$. It is shown that both ReFRESCO and FANS were capable of accurately predicting the pressure distributions on the surface of the airfoil wing section at different values of AoA.

Table 4.1 summarizes the computational resources consumed in the CFD simulations of the NREL S826 experiment. The total number of cells in the ReFRESCO simulations is nearly double that of the number in the FANS simulations while the computational time is 20% lesser than that of the FANS simulations. However, the number of processors requested for the ReFRESCO simulations is 7 times greater than the number of processors used in the FANS simulations. Consequently, in the current benchmark case of the NREL S826 airfoil experiment, the FANS simulations consumed fewer service units (SUs) than the ReFRESCO simulations.

	ReFRESCO				**FANS**			
Cases	No. Cells	Cores	Time	SUs	No. Points	Cores	Time	SUs
	$[Million]$	[/]	$[Hour]$	[/]	$[Million]$	[/]	$[Hour]$	[/]
$AoA = 4°$	4.3	224	2.7	605	2.0	28	3.6	100.8
$AoA = 8°$	4.4	224	2.9	650	2.0	28	3.6	100.8
$AoA = 12°$	4.4	224	2.9	650	2.0	28	3.6	100.8

Table 4.1: Computational resources consumed in the CFD simulations of the NREL S826 airfoil experiment. Service Units (SUs) are defined by SUs = Cores $\times$ Time.

5. CFD SIMULATIONS FOR THE PERFORMANCE OF THE NTNU BT1 WIND TURBINE *

In this chapter, the CFD simulations aiming at the performance, i.e., the thrust coefficient (C_T) and the power coefficient (C_P), of the NTNU BT1 wind turbine using ReFRESCO and FANS will be presented respectively. Systematic verification and validation (V&V) studies are performed to quantify the numerical uncertainties in the CFD-predicted wind turbine performance.

5.1 ReFRESCO Simulations

In this section, the CFD simulations performed using ReFRESCO are presented. First, the computational grid generation is provided and discussed in detail. Then, the numerical settings used in the simulations are introduced. Further, a systematic V&V study aiming at the CFD-predicted performance of the NTNU BT1 wind turbine (referred to as performance V&V hereafter) is presented. In the performance V&V, first, the simulation matrix used in the verification study will be described in detail, and the effect of the selection of the results on the estimation of the discretization uncertainty will also be discussed. Then, CFD simulations are carried out for various TSR values using a chosen combination of grid and time increments based on the results of the verification study. The numerical uncertainty obtained in the verification study at $TSR = 6$ will be applied to all the TSR values. Finally, the validation study will be presented and discussed.

The CFD simulations for this verification study using ReFRESCO are performed on the Terra cluster of the HPRC at TAMU with the Intel Xeon E5-2680 v4 2.40 GHz 14-core processors. 588 cores are used for each of the simulations and the computational time ranges from roughly 18 hours to 6 days for a single case. More details on the consumed computational resources will be given in Section 5.3.

*Reprinted with permission from "Verification and validation of CFD simulations of the NTNU BT1 wind turbine" by Ye, Maokun, Hamn-Ching Chen, and Arjen Koop, 2023. *Journal of Wind Engineering and Industrial Aerodynamics*, 234 (2023): 105336, Copyright [2023] by Elsevier.

5.1.1 Computational Domain and Grid Generation

The computational grids used in the ReFRESCO simulations are generated by leveraging the multi-block technique. In the grid generation step, in total 4 different computational grids with varying resolutions are generated for the V&V study. Each of the computational grids consists of two separately generated parts: the inner rotating part which is a short cylinder containing the rotating blades and hub, and the outer stationary part which is constructed such that it reproduces the wind tunnel in the experiment. As described in Chapter 2, those two domains are connected by interfaces through which the solution of a domain is extrapolated to pass the flow information to the other. By dividing the entire computational domain into two parts, we can refine either the inner part or the outer part without altering the other. This strategy is useful in the current study that for the quantities we are interested in, C_T and C_P, only the grid resolution in the vicinity of the rotor surfaces is critical, while the effect of the resolution in the wake region on the performance of the wind turbine is negligible [87]. Therefore, computational resources can be significantly saved by relaxing the grid resolution in the wake region of the outer stationary part. An illustration of the described computational domain including the boundary names is shown in Fig. 5.1.

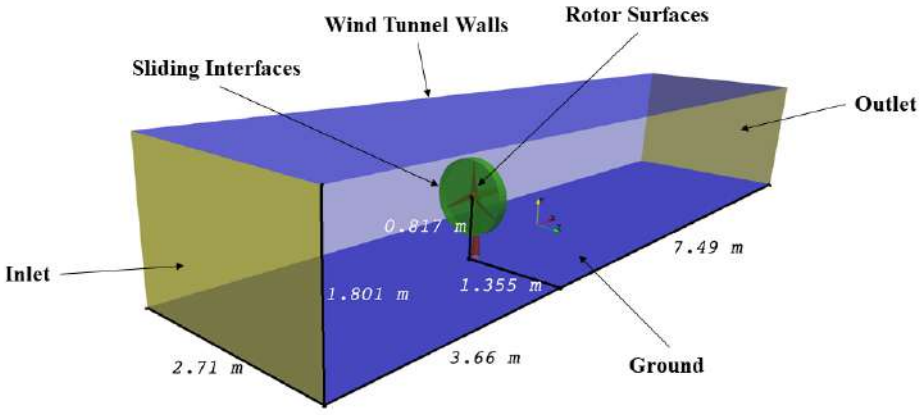

Figure 5.1: Illustration of the computational domain used in the ReFRESCO simulations aiming at the performance of the NTNU BT1 wind turbine.

Then, two different grid generation techniques are used to generate computational cells in those two separate domains: unstructured hexahedral cells are generated for the inner rotating part which contains the highly twisted blade geometry, while structured grids are generated for the outer stationary domain. For the wind turbine wall boundaries, including the blades, hub, nacelle, and tower, viscous layers are generated with the criterion of $y^+ \leq 1$, and the cell expansion ratio normal to the wall is 1.2. Similar to the computational grids used in the ReFRESCO simulations of the NREL S826 airfoil, additional refinement is applied to the leading and trailing edges as well as other high-skew regions of the wind turbine blades. In addition, the cells at the tip region and at the root of the wind turbine blades are further refined to capture the tip and root vortices.

Four computational grids with different resolutions are generated for the inner rotating part. Those 4 computational grids are denoted as G1 to G4, in which G1 represents the finest grid while G4 the coarsest. It is worth explaining that in the grid generation process, an initial grid dimension is defined for each of the three directions of the inner rotating part, i.e., the axial direction, the radial direction, and the circumferential direction, and then the initial grid is refined according to the prescribed refinement levels toward the rotor surfaces to capture the rotor geometry. Higher refinement levels, i.e., the number of times the cells will be refined, are assigned to surfaces with sharper edges, e.g., 4 for the pressure and suction sides, 6 for the leading edges, 8 for the trailing edges, and 10 for the blade tips. The initial cell numbers in each direction of the computational grids of the inner rotating part are summarized in Table 5.1. Note that the refinement levels for the rotor surfaces are the same for the four grids, only the initial grids are different.

	Axial	Radial	Circumferential
G1	281	101	360
G2	200	85	256
G3	140	51	180
G4	140	51	180

Table 5.1: Initial cell numbers in each direction of the computational grids for the inner rotating part.

As an illustration of the generated grids, the surface meshes of the blades, hub, and cylinder boundaries of the inner rotating part, and the surface meshes of the nacelle and tower of the outer stationary part are shown in Fig. 5.2. A zoomed-in view of the computational cells is also provided in Fig. 5.3. As can be observed in Fig. 5.3, higher refinement levels are defined for the leading and trailing edges, and the intersections between the blades and hub. For the outer stationary part, the high resolution of the grid is, however, still maintained in the near wake region, i.e. within 1 rotor diameter downstream, for the purpose of smooth transformation of the fluid information between the inner and outer parts.

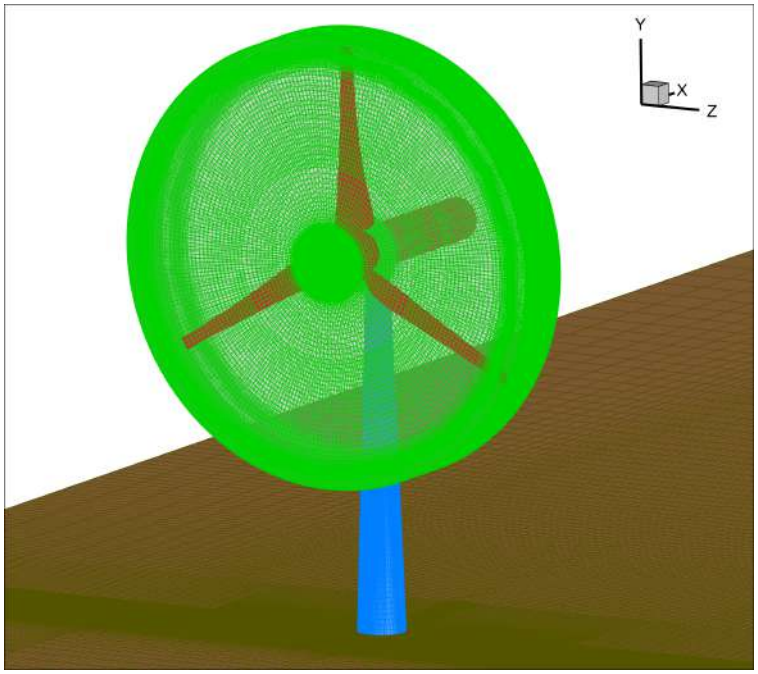

Figure 5.2: Surface mesh of the wind turbine.

5.1.2 Numerical Settings

A uniform inflow velocity of 10 m/s and a TI of 0.3% are specified at the inlet boundary. The interfaces between the inner rotating and outer stationary regions are set as BCInterface in ReFRESCO, which allows the flow information to be transferred from one to another. A fixed

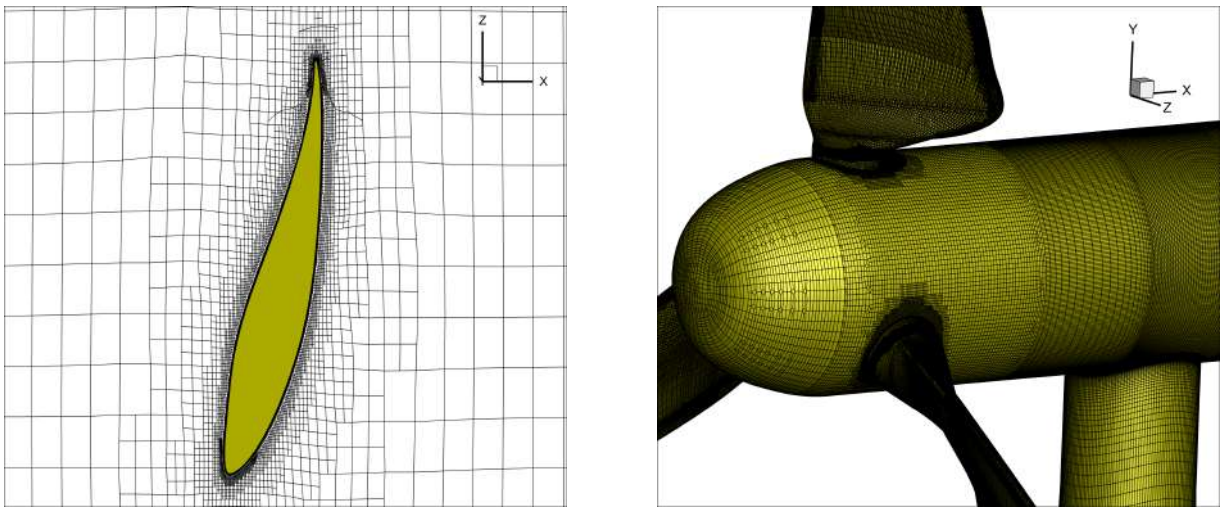

(a) Computational cells around the blade at half blade span.

(b) Surface meshes at the connection between the blade and the hub.

Figure 5.3: Detail view of the computational grids for selected locations.

pressure boundary condition is adopted for the outlet, and the no-slip condition is applied to all the wall boundaries including the surfaces of the wind turbine and the wind tunnel walls. The value of Re used in the present study is calculated at the blade tip. As a result, the chord-based Re is 1.036×10^5.

5.1.3 Performance V&V of the NTNU BT1 Wind Turbine

In the present verification study, to quantify the spatial and temporal discretization uncertainties of the CFD predictions, a simulation matrix consisting of 4 systematically refined computational grids combined with 4 different time increments is established. The basic information of the 4 computational grids used in the verification study is summarized in Table 5.2. h_i is the relative grid size and is defined by Eq. (2.28). N_R^i is the number of cells in the inner rotating part, and N_T^i denotes the total number of cells in the computational grids. It is worth emphasizing that only the cells in the inner rotating part are refined in the verification study, while the grid of the outer stationary part is kept the same for all the calculations, hence the calculation of h_i is based on the inner rotating part only.

The information regarding the four different time increments used in the calculations is pro-

Grids	h_i	N_R^i $[million]$	N_T^i $[million]$
G1	1.000	23.35	33.17
G2	1.173	14.47	24.29
G3	1.443	7.77	17.59
G4	1.807	3.96	13.78

Table 5.2: Computational grids and the corresponding relative grid sizes used in the verification study.

vided in Table 5.3. The smallest temporal spacing is denoted as T1 while the largest is T4. t_j is the relative time increment defined by Eq. (2.29), and the real time increment is denoted by Δt_j. The last column is the time steps needed for the wind turbine to rotate a full cycle, e.g., $t_j = 2.0$ corresponds to a 1.0° rotation per time step in the simulations. In each of the simulations, 7 turbine revolutions were simulated to ensure a "periodic stage" is reached. The values of C_T and C_P are then calculated by averaging the results in the last two revolutions.

Time increments	t_j	Δt_j [s]	No. time steps per revolution
T1	1.0	0.000065	720
T2	2.0	0.00013	360
T3	3.0	0.000195	240
T4	4.0	0.00026	180

Table 5.3: Time increments and the corresponding relative time steps used in the verification study.

5.1.3.1 Verification Study

iterative convergence

In the CFD simulations of the current study, two kinds of iterations are used for solving the incompressible Navier-Stokes equations, i.e., the inner iterations and outer iterations. The inner iterations are used to iteratively solve the individual equations, i.e., the momentum equations, the pressure equation, and the turbulence equations, while the outer iterations are used to achieve

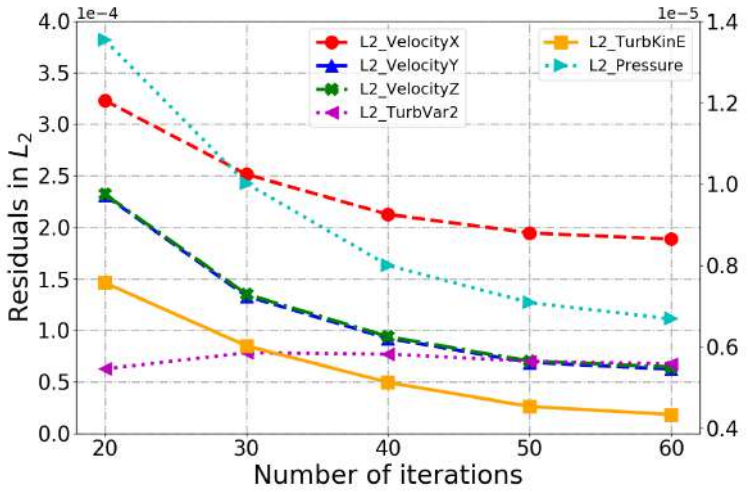

Figure 5.4: L_2-norm of the residuals at the end of every time step within the last two turbine revolutions versus the numbers of outer iterations.

the velocity-pressure coupling to maintain the incompressibility of the fluid. In practice, a large number, e.g. several hundred, is used and a low convergence criterion is set for the inner iterations, while relatively fewer iterations were used for the outer one due to the limitation in computational time. Therefore, a test is conducted first to determine the optimal number of outer iterations. The result is presented in Fig. 5.4. As shown in the figure, 5 different numbers of outer iterations are used and the L_2-norm of the residuals in the simulations are plotted. It can be seen that although the residuals are decreasing with the increase of the outer iterations, residuals are not reduced prominently when the number of outer iterations is larger than 40. Therefore, 40 outer iterations will be used in the ReFRESCO simulations.

The iterative convergence of a CFD simulation is represented by the level of residuals in that simulation. Typically, the residuals are higher in simulations with larger Courant numbers [96]. The Courant number is defined as:

$$Co = u\frac{\Delta t}{\Delta x} \tag{5.1}$$

For a wind turbine simulation, the largest theoretical Courant number will appear at the blade

tip where the velocity is the largest while the cells are the finest. Therefore, the Courant numbers at the blade tip for each of the 16 cases are calculated and listed in Table 5.4.

	G1	G2	G3	G4
T1	19.2	16.4	13.3	10.6
T2	38.4	32.7	26.6	21.2
T3	57.6	49.1	39.9	31.9
T4	76.8	65.5	53.2	42.5

Table 5.4: Largest theoretical Courant numbers for all 16 simulations. The Courant numbers are calculated at the tip of the blade for each of the simulations.

As can be observed in the table, case G1T4 has the largest Courant number while G4T1 has the smallest. First, the time histories of C_T and C_P for those two cases in the last two simulated revolutions are shown in Fig. 5.5. The vertical red lines indicate the instances in which the turbine blades "overlap" with the tower (the observer is positioned in front of the wind turbine and looking toward the downstream direction). Therefore, the spacings between two consecutive vertical red lines represent a 120° rotation of the wind turbine and in total two full revolutions are shown.

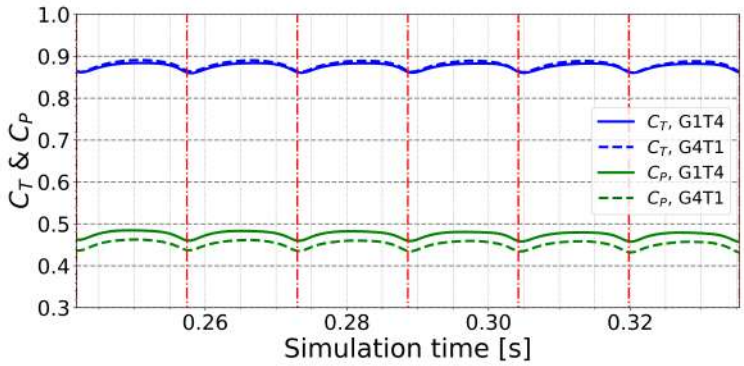

Figure 5.5: Values of C_T and C_P in the last two revolutions for cases G1T4 and G4T1.

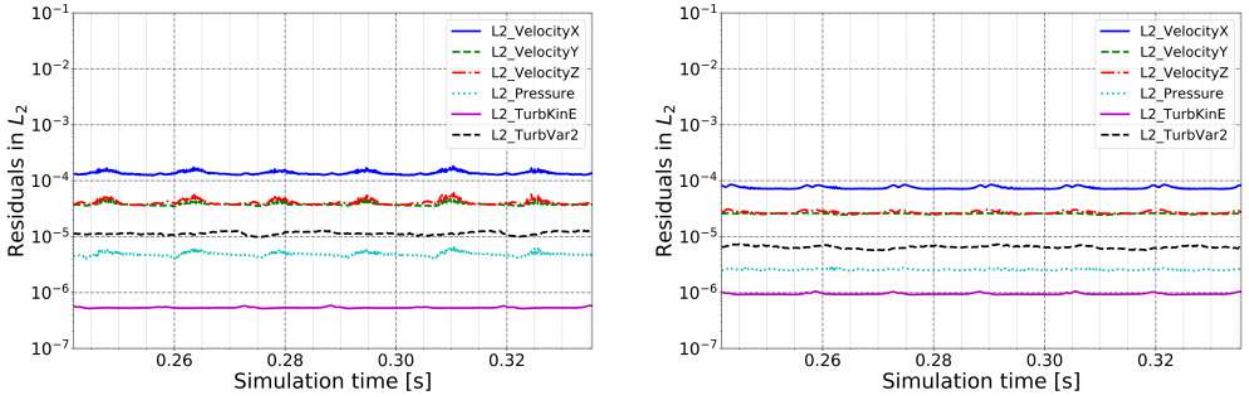

(a) L_2-norm of the residuals for G1T4 case.

(b) L_2-norm of the residuals for G4T1 case.

Figure 5.6: L_2-norm of the residuals for the cases with the largest and the smallest theoretical Courant numbers.

The residuals representing the iterative convergence of cases G1T4 and G4T1 are then presented in Fig. 5.6. It can be observed that the L_2-norm of the residuals for both simulations dropped to or under the level of 10^{-4} in the simulations. This indicates that the simulations are well converged and the iterative errors ϵ_{it} in the simulations are small and thus can be legitimately neglected in the estimation of numerical uncertainties.

The surface pressure of the NTNU BT1 wind turbine at different rotation angles obtained by using G2T2 is shown in Fig. 5.7. Note that the rotation angle is defined as the angle between the tower and the blade which points vertically downward in Fig 5.7c. It can be observed that the pressure on the tower is changing with the rotation of the blades. When the blade overlaps with the tower, i.e. rotation angle = $0°$, the pressure in the overlap region is the lowest among the four blade positions. In contrast, as the rotation angle increases, as shown in Figs 5.7d and 5.7e, the pressure in that region recovers. This implies an interaction between the blades and the tower, which is in accordance with the C_T and C_P curves shown in Fig. 5.5.

discretization uncertainty

First, the predicted values of C_T and C_P from all 16 simulations are presented in Figs. 5.8 and 5.9, respectively. The results are rendered in two ways for clarity: 1) the results are grouped by

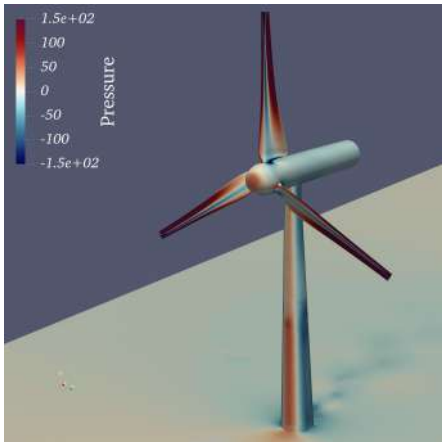

(a) Rotation angle = $-60°$

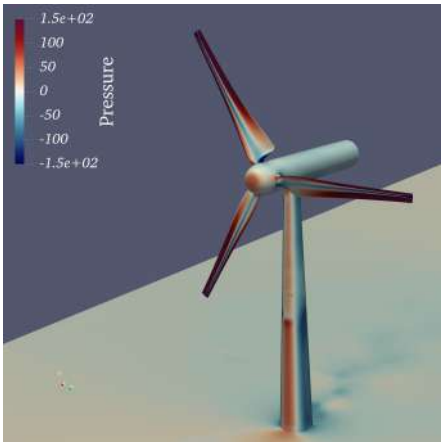

(b) Rotation angle = $-30°$

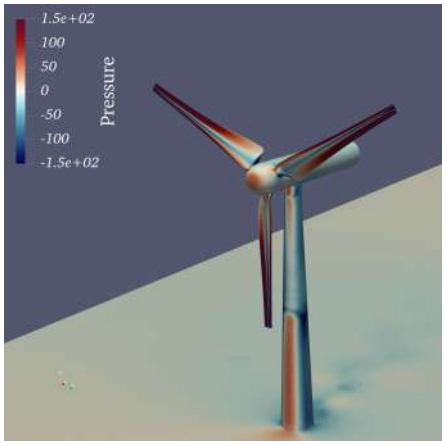

(c) Rotation angle = $0°$

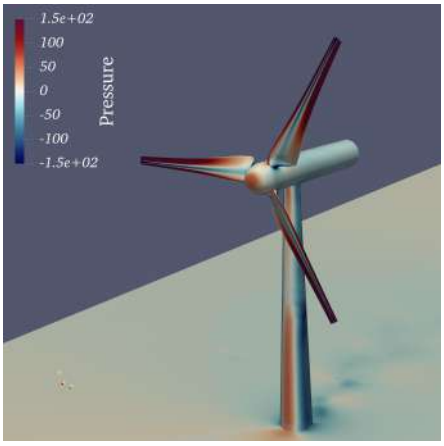

(d) Rotation angle = $30°$

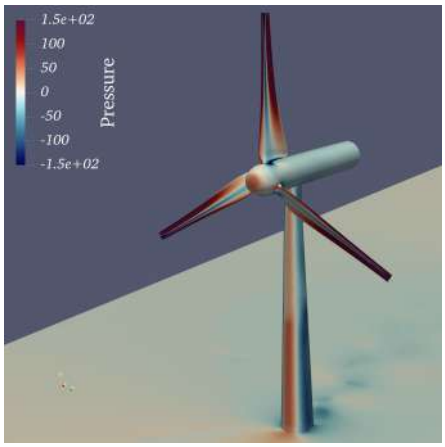

(e) Rotation angle = $60°$

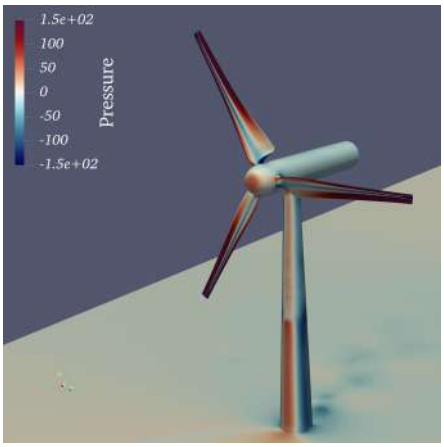

(f) Rotation angle = $90°$

Figure 5.7: Surface pressure of the NTNU BT1 wind turbine at different rotation angles.

the relative time increments and plotted as a function of the relative grid size, as shown in Figs. 5.8a and 5.9a; 2) the results are grouped by the relative grid sizes and plotted as a function of the relative time increment as shown in Figs. 5.8b and 5.9b. In Fig. 5.8a, it can be observed that C_T decreases with the refinement of the grid from G3 to G1, while increases from G4 to G3 for time increments T2, T3, and T4. In Fig. 5.8b, however, the values of C_T monotonically decrease with the refinement of temporal spacing for each of the four grids. In general, the effect of the h_i and t_j on the C_T is both clearly visible.

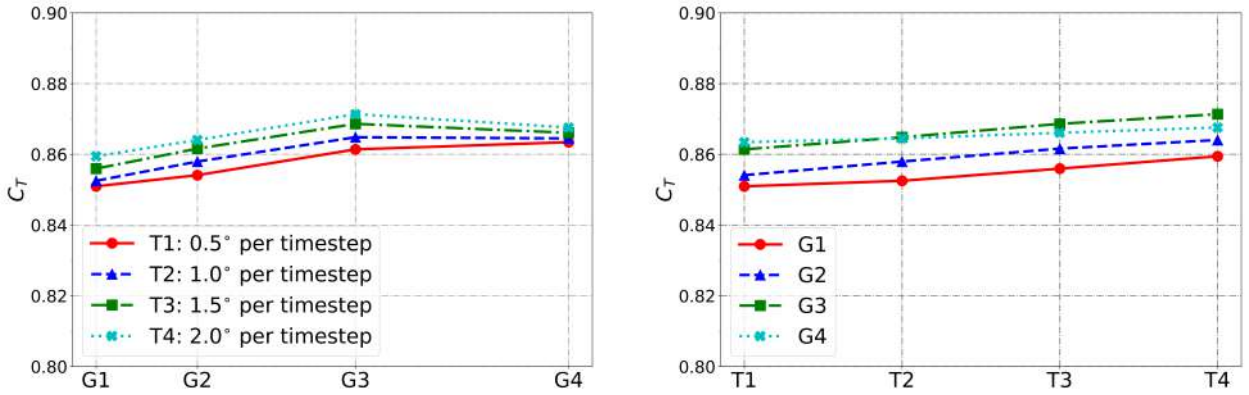

(a) Values of C_T obtained from different time increments as functions of relative grid size.

(b) Values of C_T obtained from different grids as functions of relative time step.

Figure 5.8: Predicted C_T from all 16 cases. Note that the labels on the $x-axis$ are placed according to the relative grid sizes h_i or relative time steps t_j as listed in Tables 5.2 and 5.3, respectively.

In contrast to the predicted values of C_T, the values of C_P are less sensitive to the temporal spacing. This can be seen in Fig. 5.9a in which the four groups of C_P overlap with each other, and Fig. 5.9b where the four groups of C_P are almost flat. However, a large deviation of C_P is observed when grid G4 is used, while a consistent trend of C_P which decreases with the refinement of the grid from G3 to G1 is observed. C_P obtained by using G4, on the other hand, decreases dramatically for all the four time increments. This may be an indication that the grid resolution of G4 is not fine enough to be used in the CFD simulations for the wind turbine geometry adopted in the present study.

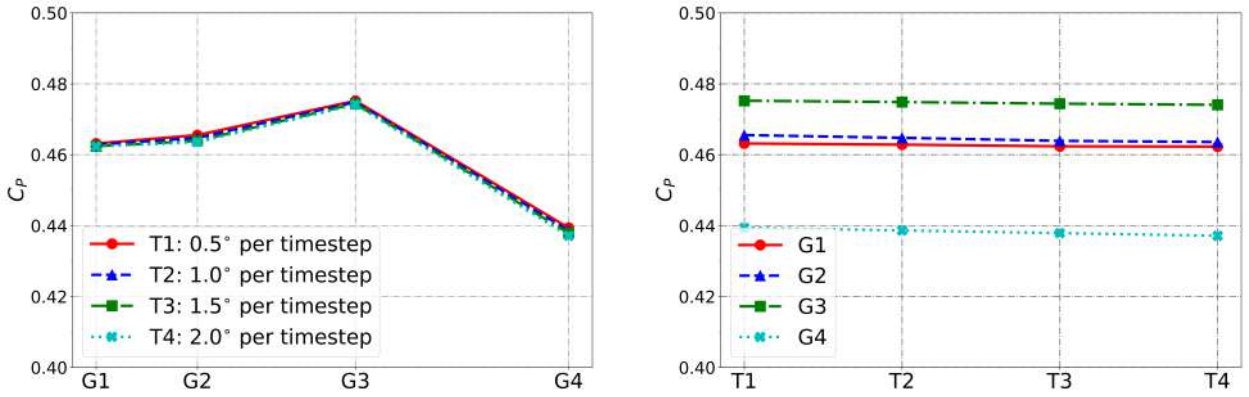

(a) Values of C_P obtained from different time increments as functions of relative grid size.

(b) Values of C_P obtained from different grids as functions of the relative time step.

Figure 5.9: Predicted C_P from all 16 cases. Note that the labels on the $x-axis$ are placed according to the relative grid sizes h_i or relative time steps t_j as listed in Tables 5.2 and 5.3, respectively.

Specifically, the grid resolution of G4 in the tip regions of the wind turbine may be too coarse to accurately capture the tip regions. As a result, C_P will be affected more significantly than C_T due to the fact that C_P is calculated from the torque of the blades while C_T is from the force. In the torque calculations, the forces of a blade cross-section are "weighted" by the distance between that cross-section and the turbine rotating axis, i.e. higher "weights" are assigned to the blade tips. Therefore, the grid resolution in the tip regions will have a larger impact on C_P than on C_T. This explanation can be confirmed by the observation that the values of C_T are less sensitive to the change of grid resolution compared to the values of C_P, as shown in Figs. 5.9a and 5.8a. A similar phenomenon was also reported by Ye et al. [97], although the grid strategy in that work is different from the one in the current study. In general, the values of C_T and C_P obtained by using G1T1, G1T2, G2T1, and G2T2, i.e., the finest settings for grids and time steps, are close to each other. Therefore, as a compromise between accuracy and computational resource, G2T2 is selected for the following validation study and thus only the uncertainties for this case will be presented in the verification study.

Then, the verification procedure adopted in this study is applied to the obtained data sets. As shown in Fig. 5.10, the fitting planes are highly distorted when using all 16 cases (Figs. 5.10a

and 5.10d), and the uncertainty bars in those two figures are extremely long, indicating that the uncertainties for C_T and C_P are high. After excluding the cases which use the coarsest grid G4, a significant improvement is obtained. As shown in Figs. 5.10b and 5.10e, the fitting planes become smooth and the uncertainty bars shorten obviously. However, further improvement in uncertainties is not achieved by further excluding the cases which use the coarsest time increment T4. As shown in Figs. 5.10c and 5.10f, no significant changes in the curvature of the fitting planes and the uncertainty bars are observed.

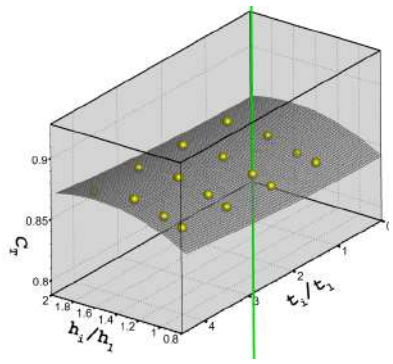

(a) Estimation of ϵ_ϕ and U_ϕ for C_T. Data points from all 16 cases are used.

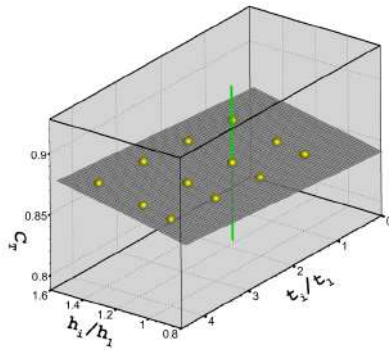

(b) Estimation of ϵ_ϕ and U_ϕ for C_T using 12 cases. Cases using G4 are excluded.

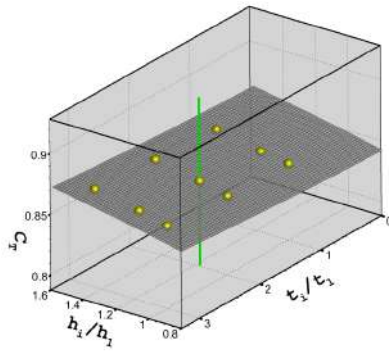

(c) Estimation of ϵ_ϕ and U_ϕ for C_T using 9 cases. Cases using G4 or T4 are excluded.

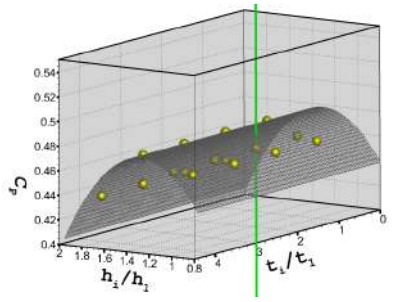

(d) Estimation of ϵ_ϕ and U_ϕ for C_P. Data points from all 16 cases are used.

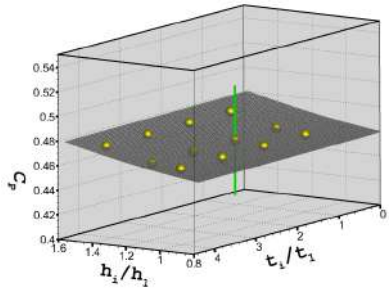

(e) Estimation of ϵ_ϕ and U_ϕ for C_P using 12 cases. Cases using G4 are excluded.

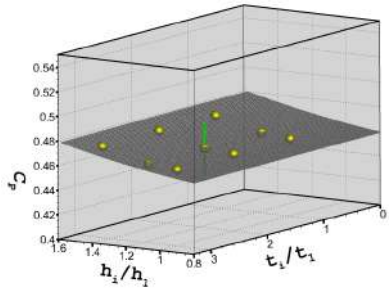

(f) Estimation of ϵ_ϕ and U_ϕ for C_P using 9 cases. Cases using G4 or T4 are excluded.

Figure 5.10: Discretization error (ϵ_ϕ) and uncertainty (U_ϕ) estimation by using different data sets. Only the uncertainties for the results obtained from grid G2 and time increment T2 are presented. The green lines represent the discretization uncertainties.

The above discussion is clear when looking at Tables 5.5 and 5.6. In those two tables, the error ϵ_ϕ is simply the absolute difference between the CFD solution and the extrapolated value, and the uncertainty is estimated by assigning a safety factor to the error based on the quality of the fitting procedure. Due to the scatter of the data points, i.e. the results from cases using grid G4, large safety factors were assigned to the errors for both predicted values of C_T and C_P when all 16 cases were used in the estimation. The uncertainty of the predicted C_T is 28.6% when using all 16 cases. For C_P, the uncertainty even jumps up to over 100% while the predicted C_P is in fact unchanged. This implies that the abnormally high uncertainty range is due to the scatter of the data points, and as discussed earlier, those data points may be caused by the insufficient grid resolution for the blade-tip regions when using grid G4, thus will be discarded in the verification study.

Sets	Extrapolated value, ϕ_0	Solution of G2T2, ϕ_{22}	Error ϵ_ϕ [%]	Uncertainty U_ϕ [%]
All cases	0.777	0.858	10.5	28.6
No G_4	0.807	0.858	6.3	7.3
No G_4 & T_4	0.803	0.858	6.8	8.0

Table 5.5: Effect of different data sets selected for the verification study on the estimation of discretization error and uncertainty for C_T obtained by G2T2. The errors are given in percentage based on the extrapolated value ϕ_0.

Sets	Extrapolated value, ϕ_0	Solution of G2T2, ϕ_{22}	Error ϵ_ϕ [%]	Uncertainty U_ϕ [%]
All cases	0.213	0.465	118.3	181.6
No G_4	0.453	0.465	2.6	9.4
No G_4 & T_4	0.452	0.465	1.8	4.4

Table 5.6: Effect of different data sets selected for the verification study on the estimation of discretization error and uncertainty for C_P obtained by G2T2. The errors are given in percentage based on the extrapolated value ϕ_0.

Although 4 cases were not included, it should be noted that 12 cases are still enough for the

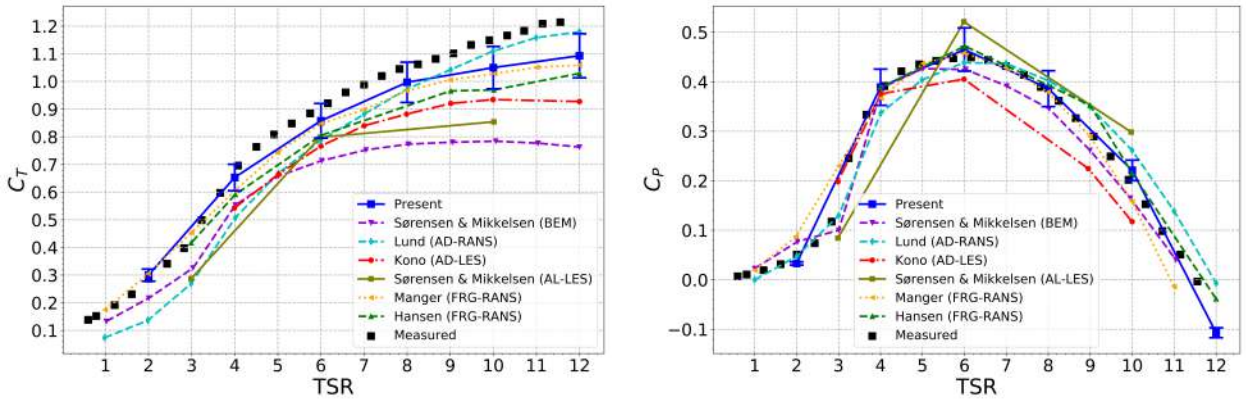

(a) Values of C_T at different TSR values.

(b) Values of C_P at different TSR values.

Figure 5.11: C_T and C_P of the NTNU BT1 wind turbine at different TSR values.

error and uncertainty estimation according to Eq. (2.30), in which only 5 unknowns are to be determined. Therefore, the discretization uncertainty for C_T and C_P obtained by G2T2 is determined according to the estimation based on the 12 cases, which are 7.3% and 9.4%, respectively. Further, since the iterative uncertainties in the simulations were two orders of magnitudes lower than the discretization uncertainty, the total numerical uncertainty is thus assumed to be contributed solely by the discretization uncertainty. Finally, these uncertainty ranges will be adopted in the following validation study.

5.1.3.2 Validation study

Grid G2 and time increment T2 are adopted in the CFD simulations for the validation study. CFD calculations are performed for a range of different TSR values, i.e. 2, 4, 8, 10, and 12. The results of C_T and C_P are obtained and compared against the experimental data with the uncertainties obtained from the verification study. The curves of C_T and C_P are shown in Figs. 5.11a and 5.11b, respectively. Results from other methods (as reported in [3]) are also provided in the figures for comparison purposes. The details of the selected numerical results are presented in Table 5.7.

For the thrust coefficient C_T, the present results agree with the experimental data in trend. The experimental data is within the range of uncertainty bars until the value of TSR increases to 8. For larger TSR values, i.e. the runaway state, the predicted values of C_T are significantly lower

Numerical Results	Rotor	Tower	Gov. Eq.	Turb. Closure	CFD Solver
Sørensen & Mikkelsen (BEM)	BEM	No	-	-	-
Lund (AD-RANS)	AD	No	RANS	$k-\omega$ SST	OpenFOAM
Kono (AD-LES)	AD	No	LES	Sub-grid	Front Flow/red
Sørensen & Mikkelsen (AL-LES)	AL	No	LES	Sub-grid	EllipSys3D
Manger (FRG-RANS)	FRG	Yes	RANS	$k-\omega$ SST	Ansys Fluent
Hansen (FRG-RANS)	FRG	No	RANS	$k-\omega$ SST	STAR CCM+

Table 5.7: Details of the different numerical methods. The numerical methods adopted by the participants are denoted as: BEM - blade element method, AD - actuator disc, AL - actuator line, and FRG - fully resolved geometry.

than the measured data, and thus the validation is not achieved in this range. This is, however, in accordance with the results obtained by other methods. As shown in Fig. 5.11a, all the methods except for Lund (AD-RANS) have a similar trend in the prediction of the C_T curve in which the values of C_T were significantly under-predicted in the high TSR region. The result obtained from Lund (AD-RANS), nevertheless, has the largest value of C_T at $TSR = 10$ and 12, while significantly under-predicts the value in the low TSR region (TSR ≤ 4). For the power coefficient C_P, as shown in Fig. 5.11b, the predicted values of C_P from the present study are in good agreement with the measured C_P over the entire TSR range. All the measured values of C_P are within the uncertainty range, hence the validation is achieved for the predicted values of C_P.

In the high TSR range, the deviation between the predicted C_T and the experimental data could be owing to the following issues:

- Blockage effect of the wind tunnel. The wind tunnel boundary layers were not resolved in the present study to save computational resources, and the blockage of the wind tunnel was assumed to have a negligible effect on the performance of the wind turbine. This simplification in the simulations could be a factor that is responsible for the deviation. However, as discussed by Krogstad and Lund [5], the rotor swept area was 11.8% of the wind tunnel cross-section in the NTNU BT1 experiment, and the author concluded that the blockage effect in the experiment is "expected to be small." In addition, although not presented in this paper, test CFD simulations were performed by using a grid in which the boundary layers of

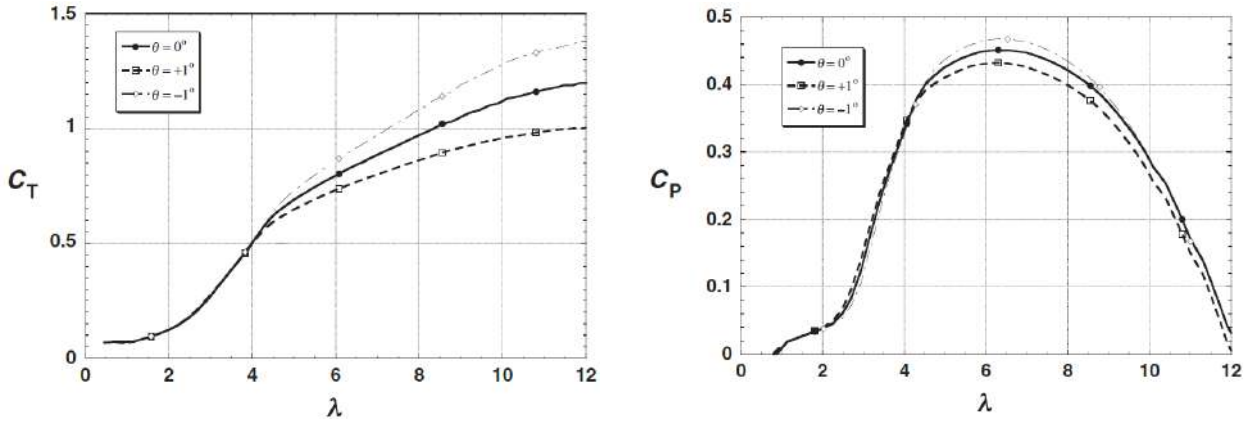

Figure 5.12: Effect of blade pitch misalignment on the wind turbine performance, adopted from [5].

the wind tunnel walls were resolved. However, less than 1% difference was observed in the obtained results.

- Blade pitch misalignment. As discussed by Krogstad and Lund [5], due to the small scale of the model wind turbine and the complicated shape of the blades, accurately setting the blade pitch is difficult. Both C_T and C_P will be affected even when the blade pitch misalignment is small. The effect of the blade pitch misalignment of the NTNU BT1 wind turbine was also investigated by Krogstad and Lund [5]. Two figures in that literature [5] are adopted here for illustration purposes, as shown in Fig. 5.12. It can be observed that the misalignment affected the values of C_T significantly, especially in the high TSR region. The values of C_P, however, are less sensitive to the blade pitch misalignment in the low and high TSR range while being affected most significantly at the design TSR of 6. These trends are in accordance with the results shown in Fig. 5.11. Although a special alignment rig was made for the experiment, an uncertainty of the pitch angle of $0.25°$ was still present [5]. Therefore, this uncertainty of the blade pitch is expected to have a certain degree of influence on the performance of the wind turbine.

- The uncertainties in the experiment are unknown. Since the details of the experiment were not reported, e.g. whether the experiment was repeated, we do not know the uncertainty

ranges of the C_T and C_P obtained from the experiment. As a result, the contribution of the experimental uncertainties was not taken into account. This assumption may be incorrect and thus undermine the results of the validation study.

5.2 FANS Simulations

In this section, the simulations targeting the performance of the NTNU BT1 wind turbine performed by using FANS are presented. The structure of this section is the same as the previous section. First, the computational domain and the grid generation are described. Then, a systematic V&V study aiming at the CFD-predicted obtained by FANS will be performed. Similar to the performance V&V performed in the last section by using ReFRESCO simulations, a simulation matrix used in the FANS simulations will be introduced first. Then, the discretization uncertainties will be quantified and the validation study will be carried out.

The CFD simulations for this study using FANS are performed on the Grace cluster of the HPRC at TAMU with the Intel Xeon E5-2680 v4 2.40 GHz 14-core processors. 52 cores are used for each of the simulations and the computational time ranges from roughly 1 day to 3 days for a single case. More details on the consumed computational resources will be given in Section 5.3.

5.2.1 Computational Domain and Grid Generation

The computational domain used in the FANS simulations is illustrated in Fig. 5.13. The size of the computational domain is the same as the one used in the ReFRESCO simulations, therefore no repeated introductions will be provided here.

Structured overset grid blocks are then generated in the computational domain for the FANS simulations. For the current simulations targeting the performance of the NTNU BT1 wind turbine, 3 different grids with varying resolutions in the near-field of the rotor are generated. Each of the 3 grids has 93 grid blocks in total, including 3 phantom grid blocks for hole-cutting purposes. To get a better idea of the structure of the computational grid, an overview of the computational grid and the grid blocks covering the surfaces of the wind turbine are shown in Fig. 5.14.

As only the grid resolution in the vicinity of the rotor is crucial for calculating the performance

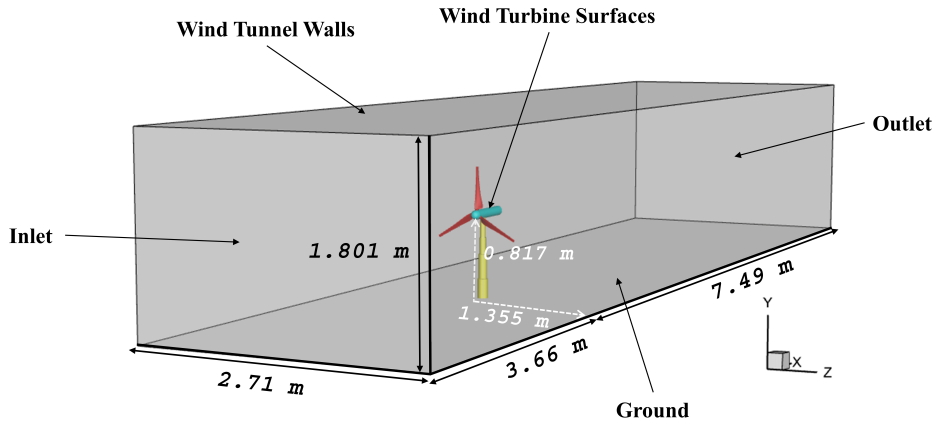

Figure 5.13: Illustration of the computational domain used in the FANS simulations aiming at the performance of the NTNU BT1 wind turbine.

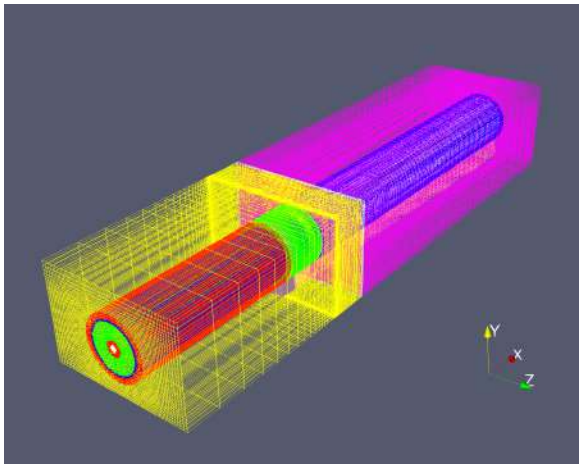

(a) Overview of the overset grid blocks used in the FANS simulations of the current study.

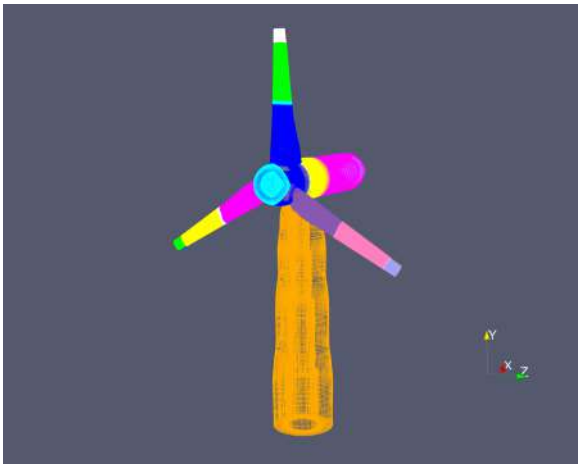

(b) Grid blocks covering the surfaces of the wind turbine.

Figure 5.14: Computational grid generated for the FANS simulations of the NTNU BT1 wind turbine.

of the wind turbine, only the grid blocks near the rotor will be refined for the V&V study. The grid blocks that need to be refined are highlighted, i.e., colored in red (boundary-layer blocks), cyan (intermediate blocks), and yellow (background disc blocks), in Fig. 5.15.

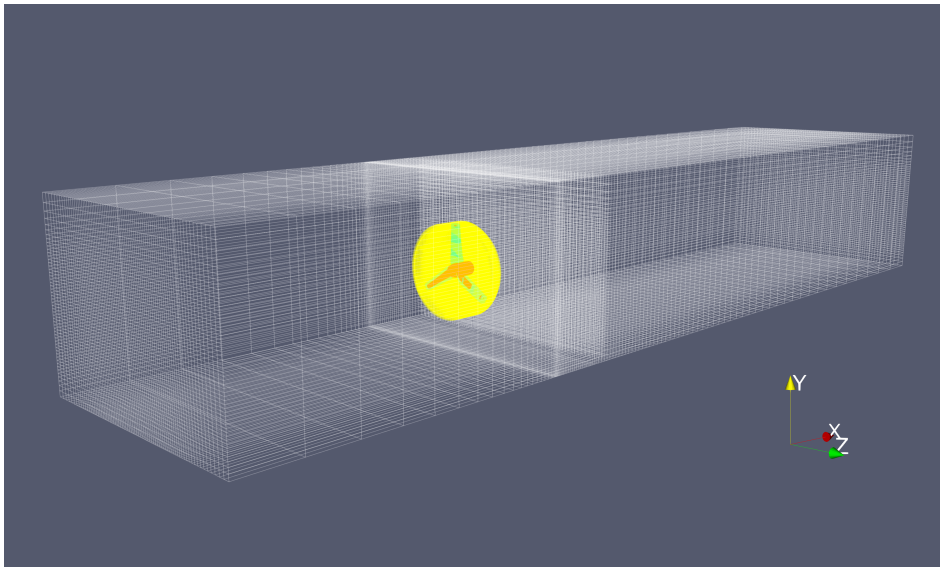

Figure 5.15: Computational blocks that are refined in the V&V study. The red blocks are the boundary layer blocks; the yellow blocks are the background disc blocks

It should be mentioned that for FANS simulations, grid cells from different blocks should approximately be of the same size in the overset regions to ensure a smooth exchange of fluid information between the different overset blocks. Therefore, between the boundary-layer blocks (colored in red) and the background disc blocks (colored in yellow), intermediate blocks are generated. Cross-sectional views are provided to show the details of the overset-grid structure, as shown in Fig. 5.16.

5.2.2 Numerical Settings

A uniform inflow is specified at the inlet, and the linear-extrapolation boundary condition in FANS is specified at the outlet. No-slip condition is applied to the surfaces of the wind turbine including blades, hub, nacelle, and tower. For the wind tunnel walls, a slip-wall condition is used.

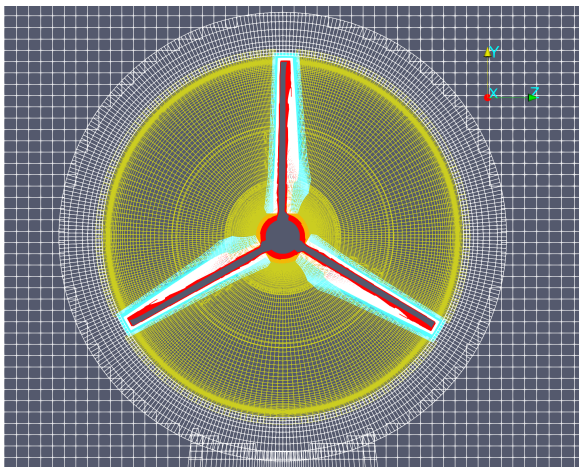

(a) Computational cells around the blade at half blade span.

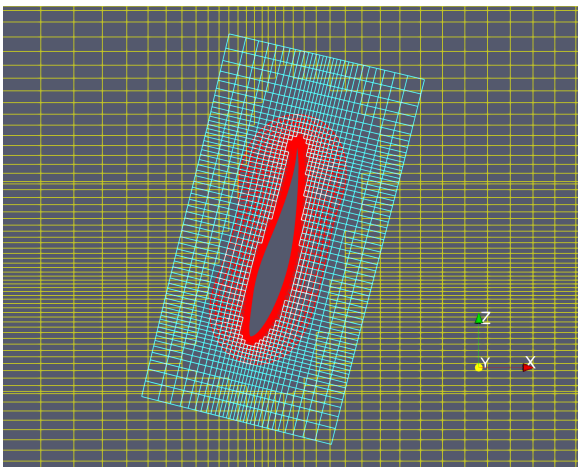

(b) Surface meshes at the connection between the blade and the hub.

Figure 5.16: Cross-sectional views of the computational grids used in the FANS simulations.

The boundary condition for the surfaces of overset grid blocks that overlap with other blocks is set to "interior boundary surfaces". Interpolation will be performed using the flow information from the donor grids. The two-layer $k-\epsilon$ turbulence model is adopted for the turbulence closure, as described in 2.3.2.

5.2.3 V&V Study for the Turbine Performance

5.2.3.1 Verification Study

As mentioned earlier, three different computational grids with systematically refined near-field blocks are generated for the verification study. The three computational grids are denoted as G1, G2, and G3. Following the convention used in the ReFRESCO simulations, G1 represents the finest grid while G3 is the coarsest. The information regarding the three computational grids is summarized in Table 5.8. The number of grid points in the refined blocks is denoted by N_R^i, and the total number of grid points of a computational grid is denoted by N_T^i. The corresponding relative grid size, h_i, will also be given in the table.

Further, three different time increments are used in the verification study, as shown in Table 5.9. The smallest temporal spacing is denoted as T1 while the largest is T3. t_j is the relative

Grids	h_i	N_R^i $[million]$	N_T^i $[million]$
G1	1.00	10.47	14.78
G2	1.20	6.03	10.22
G3	1.44	3.48	7.58

Table 5.8: Computational grids and the corresponding relative grid sizes used in the verification study.

time increment while the real time increment is denoted by Δt_j. The last column is the time steps needed for the wind turbine to rotate a full cycle, e.g., $t_j = 2.0$ corresponds to a 4.0° rotation per time step in the simulations.

Time increments	t_j	Δt_j [s]	No. time steps per revolution
T1	1.0	0.00026	180
T2	1.5	0.00039	120
T3	2.0	0.00052	90

Table 5.9: Time increments and the corresponding relative time steps used in the verification study.

It is worth pointing out that in Eq. (2.27) and Eq. (2.30), only 5 unknowns exist. However, according to the recommendation [79], one more data set is preferred in the verification procedure. Therefore, unlike in the previous one presented in Section 5.1.3 in which a full simulation matrix is established and simulations were performed for every combination of h_i and t_j, in the current V&V study, CFD simulations will be performed for only 6 combinations of h_i and t_j to save computational resources. An illustration of the selected combinations of h_i and t_j is provided in Table 5.10.

iterative convergence

As discussed earlier (see 5.1.3.1), the optimal number of outer iterations needs to be determined first. Fig. 5.17 presents the change of residuals with the increase of the outer iterations in FANS simulations. It can be observed that the residuals decrease with the increase of outer iterations and

	T1	T2	T3
G1		✓	
G2	✓	✓	✓
G3	✓		✓

Table 5.10: Selected combinations of the grid and time step size used in the verification study.

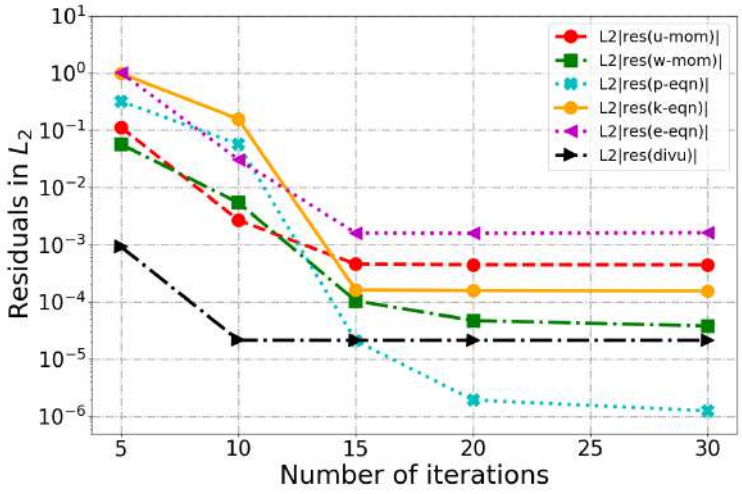

Figure 5.17: L_2-norm of the residuals versus the numbers of outer iterations in the FANS simulations.

no more obvious decrease is identified when the number of iterations reaches 20. Therefore, 20 outer iterations will be used in the FANS simulations. Fig. 5.18 shows the L_2-norm of the residuals in the G2T2 case obtained by FANS.

discretization uncertainty

The predicted values of C_T and C_P from all 6 simulations are presented in Figs. 5.19 and 5.21, respectively. Again, the results are rendered in two ways for clarity: 1) the results are grouped by the relative time increments and plotted as a function of the relative grid size, as shown in Figs. 5.19a and 5.21a; 2) the results are grouped by the relative grid sizes and plotted as a function of the relative time increment as shown in Figs. 5.19b and 5.21b.

In Fig. 5.19a it can be observed that C_T decreases with the refinement of the grid from G3 to

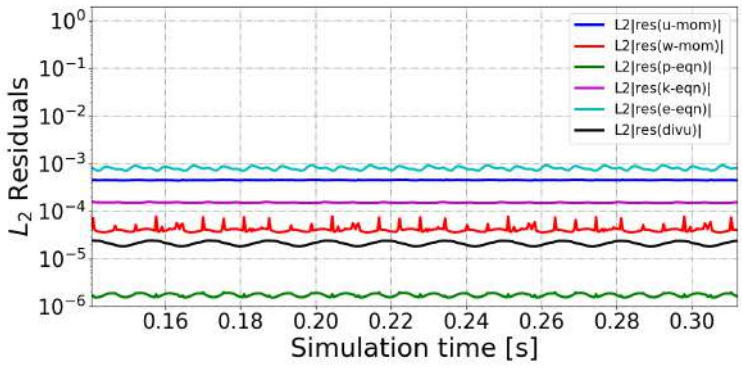

Figure 5.18: L_2-norm of the residuals in the G2T2 case.

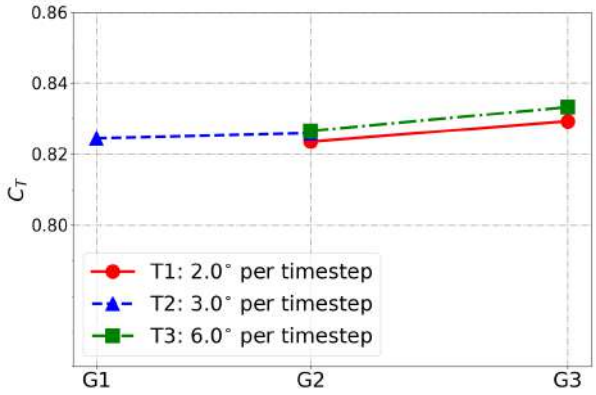

(a) Values of C_T obtained from different time increments as functions of relative grid size.

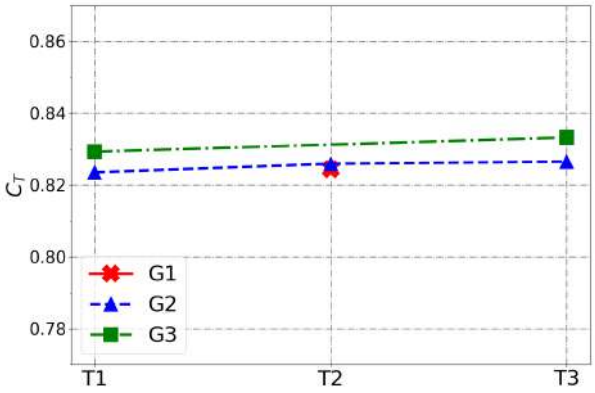

(b) Values of C_T obtained from different grids as functions of relative time step.

Figure 5.19: Predicted C_T from all 6 cases. Note that the labels on the $x - axis$ are placed according to the relative grid sizes h_i and the relative time steps t_j as listed in Tables 5.8 and 5.9, respectively.

G1. And in Fig. 5.19b, the values of C_T also decrease with the refinement of temporal spacing. As a trade-off between accuracy and computational time, results obtained in case G2T2 are selected for the following validation study, and thus only the uncertainties for this case will be presented in the verification study.

Then, the verification procedure adopted in this study is applied to the predicted values of C_T, as shown in Fig. 5.20 in which the green line represents the discretization uncertainty for the result obtained by the G2T2 case. The result of the fitting procedure is summarized in Table 5.11. The

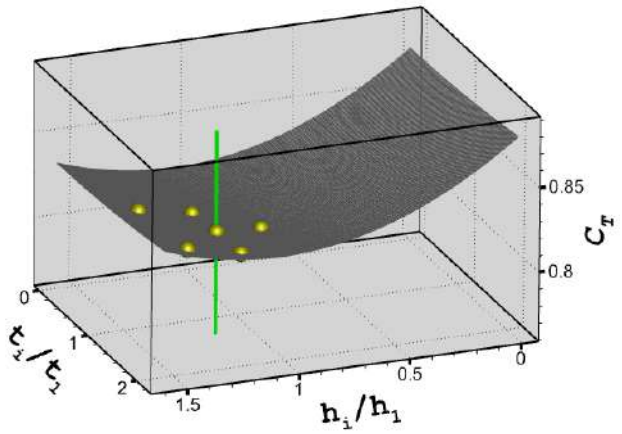

Figure 5.20: Discretization uncertainty (U_ϕ) estimations of C_T for case G2T2. The green line represents the discretization uncertainty.

final error and the discretization uncertainty of the result obtained by case G2T2 are 5.4% and 7.3%, respectively.

Quantity	Extrapolated value, ϕ_0	Solution of G2T2, ϕ_{22}	Error ϵ_ϕ [%]	Uncertainty U_ϕ [%]
C_T	0.873	0.826	5.4	7.3

Table 5.11: Discretization error and uncertainty for C_T obtained by G2T2. The errors are given in percentage based on the extrapolated value ϕ_0.

In Fig. 5.21a it can be observed that C_P increases with the refinement of the grid from G3 to G1. And in Fig. 5.21b, the values of C_P decrease with the refinement of temporal spacing. As a trade-off between accuracy and computational time, C_P obtained in case G2T2 is selected for the following validation study and thus only the uncertainties for this case will be presented in the verification study.

Afterward, the verification procedure is applied to the predicted values of C_P, as shown in Fig. 5.22. The green line represents the discretization uncertainty of the result obtained by case G2T2. The result of the fitting procedure is summarized in Table 5.12. The final error and the discretization uncertainty of C_P obtained by case G2T2 are 6.8% and 8.1%, respectively.

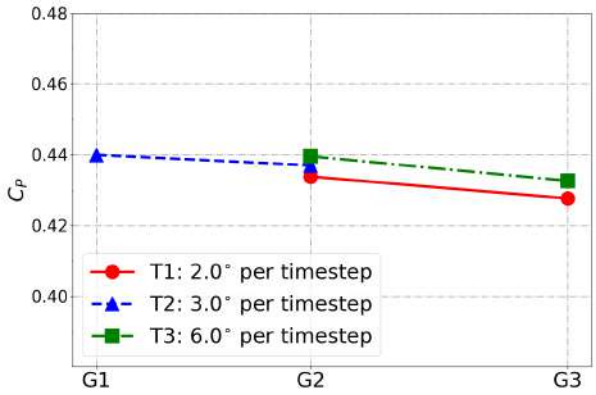

(a) Values of C_P obtained from different time increments as functions of relative grid size.

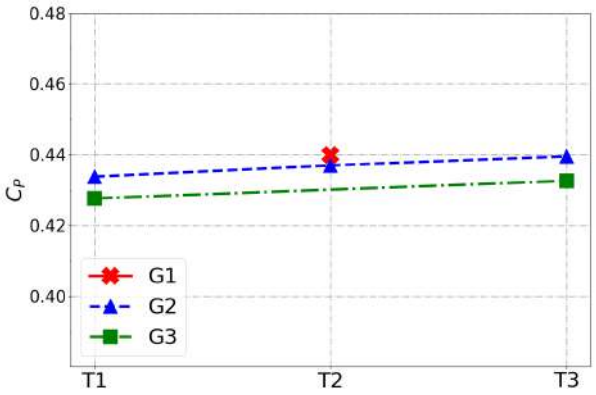

(b) Values of C_P obtained from different grids as functions of relative time step.

Figure 5.21: Predicted C_P from all 6 cases. Note that the labels on the $x - axis$ are placed according to the relative grid sizes h_i and the relative time steps t_j as listed in Tables 5.8 and 5.9, respectively.

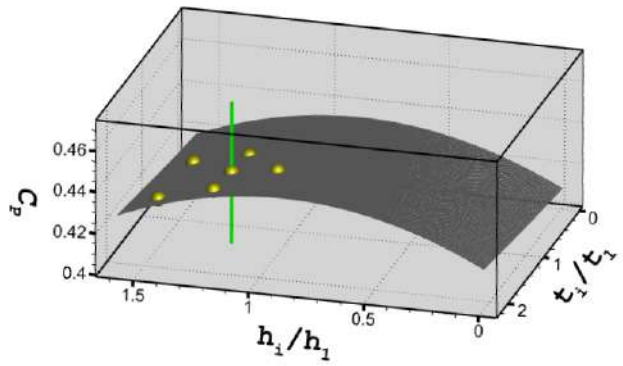

Figure 5.22: Discretization uncertainty (U_ϕ) estimations of C_P for case G2T2. The green lines represent the discretization uncertainties.

Quantity	Extrapolated value, ϕ_0	Solution of G2T2, ϕ_{22}	Error ϵ_ϕ [%]	Uncertainty U_ϕ [%]
C_P	0.409	0.437	6.8	8.1

Table 5.12: Discretization error and uncertainty for C_T obtained by G2T2. The errors are given in percentage based on the extrapolated value ϕ_0.

The surface pressure on the wind turbine and the corresponding velocity field in the rotor plane at different rotation angles are shown in Fig. 5.23. Note that the rotation angle is defined as 0° when the blade overlaps the tower in the yOz plane, as shown in Fig. 5.23e.

5.2.3.2 Validation Study

Grid G2 and time increment T2 are then adopted in the CFD simulations for the validation study. CFD calculations are performed for a range of different TSR values, i.e. 2, 4, 8, 10, and 12. The results of C_T and C_P are obtained and compared against the experimental data with the uncertainties obtained from the verification study. The curves of C_T and C_P are shown in Figs. 5.24a and 5.24b, respectively. Selected numerical results from other methods (as reported in [3]) including the ReFRESCO results are also provided in the figures for comparison purposes. For the details of the different numerical results, please refer to Table 5.7.

For the thrust coefficient C_T, the FANS results agree with the experimental data in trend while being slightly smaller than the ReFRESCO results. The experimental data is within the range of uncertainty bars until the value of TSR increases to 8. For smaller TSR values, i,e., $TSR \leqslant 8$, the FANS prediction agrees with the measurement reasonably well. However, for larger TSR values, i.e., $TSR \geqslant 8$, the predicted values of C_T are significantly lower than the measured data, and thus the validation is not achieved in this range. This phenomenon was also observed in the ReFRESCO results, and its potential cause has been discussed earlier in Section 5.1.3.2. For brevity, no more discussion will be provided here. For the power coefficient C_P, as shown in Fig. 5.24b, the predicted values of C_P from the present study are in good agreement with the measured C_P over the entire TSR range.

5.3 Chapter Summary

In this chapter, the CFD simulations were performed targeting the performance, i.e., C_T and C_P, of the NTNU BT1 wind turbine by using ReFRESCO and FANS. Systematic verification and validation study were applied respectively for the ReFRESCO and FANS predictions. For ReFRESCO simulations, a simulation matrix consisting of 16 cases was constructed by using 4

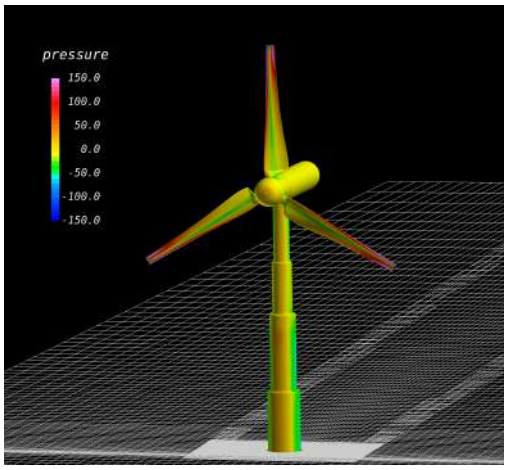

(a) Surface pressure at a rotation angle of $-180°$

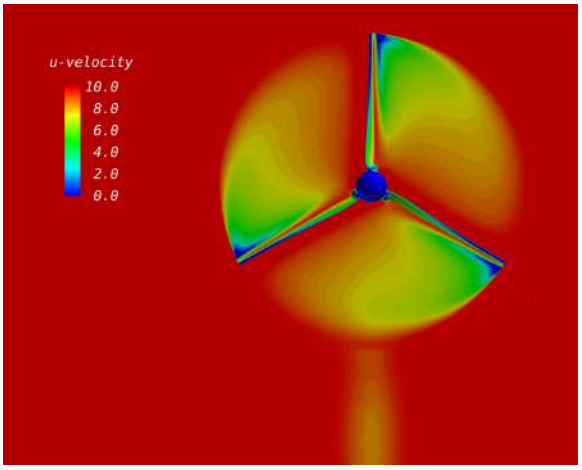

(b) Velocity field in the rotor plane at a rotation angle of $-180°$

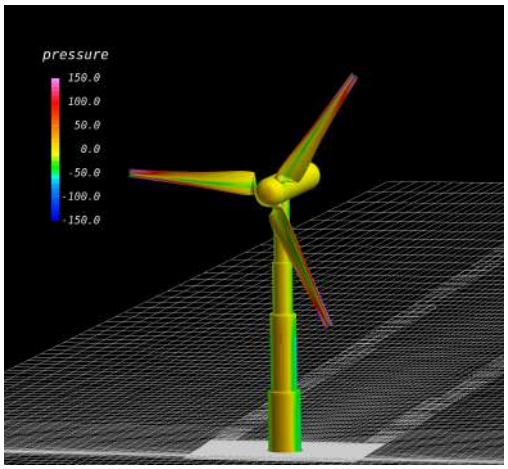

(c) Surface pressure at a rotation angle of $-84°$

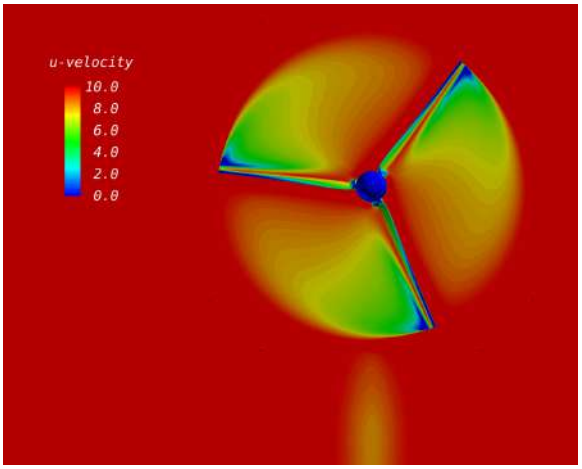

(d) Velocity field in the rotor plane at a rotation angle of $-84°$

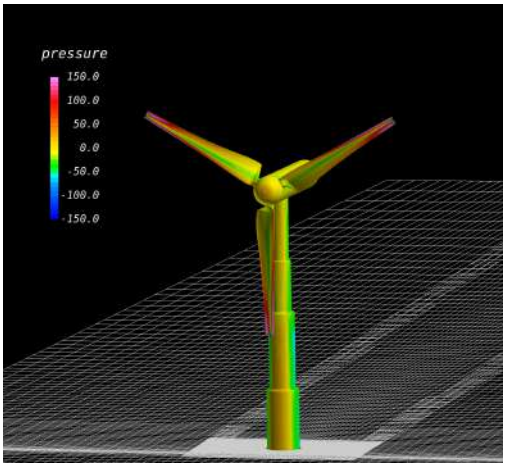

(e) Surface pressure at a rotation angle of $0°$

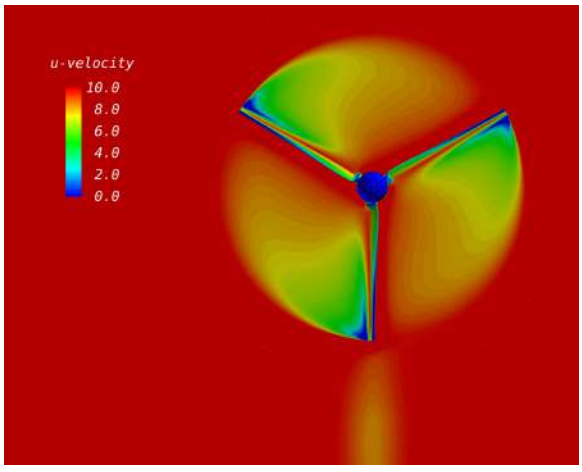

(f) Velocity field in the rotor plane at a rotation angle of $0°$

Figure 5.23: Surface pressure of the NTNU BT1 wind turbine at different rotation angles.

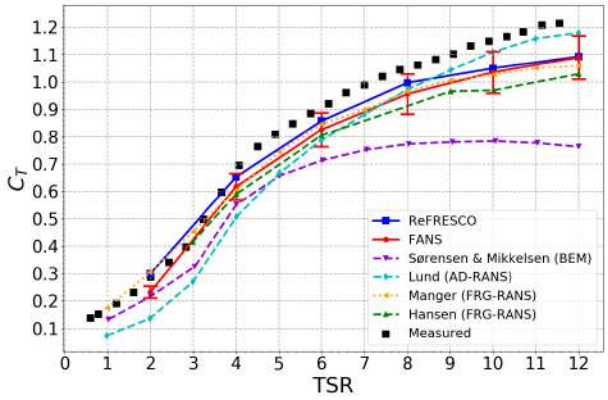

(a) Values of C_T at different TSR values obtained from FANS simulations.

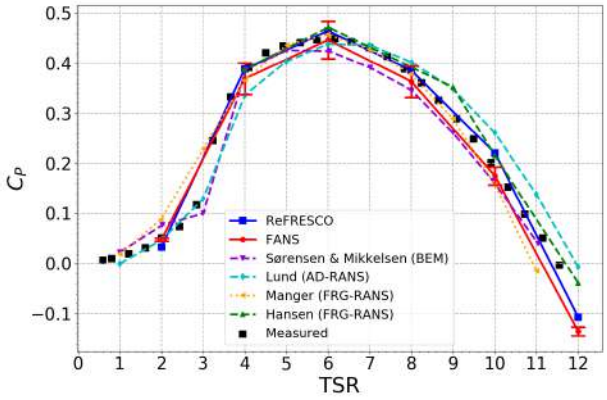

(b) Values of C_P at different TSR values obtained from FANS simulations.

Figure 5.24: C_T and C_P of the NTNU BT1 wind turbine at different TSR values obtained from FANS simulations. For the details of the different numerical results, please refer to Table 5.7.

different time grids and 4 different time increments. Then, the adopted verification procedure was applied to the CFD predictions and the obtained numerical uncertainty was used in the validation. For FANS simulations, 6 cases were constructed by using 3 different time grids and 3 different time increments. The adopted verification procedure was applied to the obtained data sets and the validation study is also performed. It was found that the numerical predictions of C_T agree with the experimental data in trend while having relatively large deviations from the measurement in the high TSR range. For the predicted values of C_P, the numerical results match the measurement well.

For reference purposes, Table 5.13 presents the detailed computational resources of selected cases, i.e., the G2T2 case in ReFRESCO simulations and the G2T2 case in FANS simulations. The total estimated computational resources consumed by the ReFRESCO and FANS simulations aiming at the performance of the NTNU BT1 wind turbine are approximately 2 million and 100 thousand service units (SUs), respectively, funded by TAMU HPRC.

	ReFRESCO					**FANS**				
Cases	No. Cells	Cores	deg/ts	Time	SUs	No. Points	Cores	deg/ts	Time	SUs
	$[Million]$	[/]	$[Deg]$	$[Hour]$	[/]	$[Million]$	[/]	$[Deg]$	$[Hour]$	[/]
G2T2	24.2	588	1.0	15.1	8879	10.22	52	3	37.35	1942

Table 5.13: Computational resources of selected cases used in the CFD simulations targeting the performance of the NTNU BT1 wind turbine. Note: "deg/ts" is the abbreviation for "degrees per time step".

6. CFD SIMULATIONS FOR THE WAKE CHARACTERISTICS OF THE NTNU BT1 WIND TURBINE *

6.1 ReFRESCO Simulations

In this section, first, a thorough V&V study is performed for the predicted wake characteristics of the BT1 wind turbine. Then, the flow details of the CFD prediction are illustrated and discussed.

The CFD simulations for this study using ReFRESCO are performed on the Terra cluster of the HPRC at TAMU with the Intel Xeon E5-2680 v4 2.40 GHz 14-core processors. 616 cores are used for each of the simulations and the computational time for a single simulation ranges approximately from 6 days to 15 days. More details on the consumed computational resources will be given in Section 6.3.

6.1.1 Computational Domain and Grid Generation

The computational grids are constructed by leveraging the multi-block technique. The computational domain is decomposed into three separate domains: 1) the inner rotating domain which is a short cylinder containing the rotor; 2) the stationary wake domain which is behind the rotor and extends to the outlet; 3) the stationary outer domain which is generated to match the wind tunnel in the experiment. In the simulations, the inner rotating domain will rotate while the wake and outer domains remain stationary. Those domains are connected by sliding interfaces through which the solution of a domain is extrapolated to pass the flow information to the neighboring domains. By this decomposition, we can refine an individual part without changing the others. This strategy enables us to perform a systematic verification study specifically for the wake region.

An illustration of the computational domain is provided in Fig. 6.1. As shown in the figure, the coordinate system is defined as follows: the origin of the coordinate system is placed at the rotor center, the positive $x - axis$ points from inlet to outlet and $y - axis$ from bottom to top, and the

*Reprinted with permission from "High-fidelity CFD simulations for the wake characteristics of the NTNU BT1 wind turbine" by Ye, Maokun, Hamn-Ching Chen, and Arjen Koop, 2023. *Energy*, 265 (2023): 126285, Copyright [2023] by Elsevier.

$z - axis$ is thus defined according to the right-hand rule.

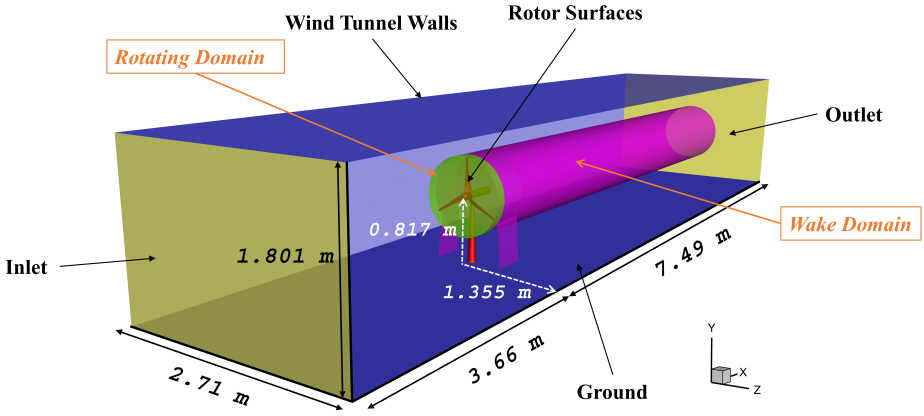

Figure 6.1: Computational domain used in the ReFRESCO simulations aiming at the wake characteristics of the BT1 wind turbine.

Then, two different grid generation techniques are applied to those three domains: unstructured hexahedral cells are generated for the inner rotating domain which contains the highly twisted blade geometry, while structured grids are generated for the wake and outer domains. For the wind turbine wall boundaries, including the blades, hub, nacelle, and tower, viscous layers are generated with the criterion of $y^+ < 1$, and the cell expansion ratio normal to the wall is 1.2. High refinement levels are applied to the leading and trailing edges and other high-skew regions of the turbine blades. In addition, the meshes at the tip and root regions are further refined to capture the tip and root vortices. Illustrations of the computational grids of the inner rotating domain and the stationary wake domain are shown in Fig. 6.2. It is worth mentioning that in the following verification study, only the grid in the wake domain is refined while the other parts are unchanged. The grid resolution of the inner rotating domain is determined based on the performance V&V as described in Chapter 5.

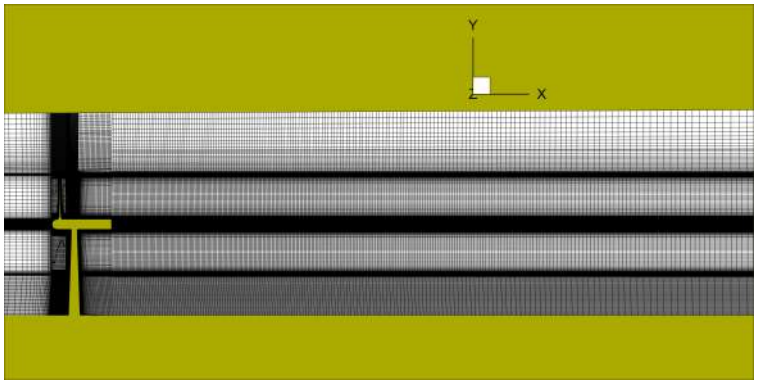

Figure 6.2: Illustration of the computational grid of the wake domain.

6.1.2 Numerical Settings

A uniform inflow velocity of 10 m/s and a TI of 0.3% are specified at the inlet, and a fixed pressure boundary condition is adopted at the outlet. The no-slip condition is applied to all the wall boundaries. The interfaces between the different domains are set as BCInterface in ReFRESCO, which allows the flow information to be transferred from one to another. Unsteady RANS calculations are performed, and an implicit three time-level scheme [98] is used for the time marching.

6.1.3 V&V Study for the Wake Characteristics

6.1.3.1 Verification

To quantify the spatial and temporal discretization uncertainties, a simulation matrix consisting of 3 systematically refined computational grids coupled with 3 different time increments is established. It is worth mentioning again that only the computational cells in the wake domain are refined, while the grids in the other domains remain unchanged. Those 3 computational grids are denoted as G1 to G3, in which G1 represents the finest grid while G3 is the coarsest. The numbers of cells in each direction, i.e. the axial, radial, and circumferential direction of the computational grids in the wake domain are summarized in Table 6.1. As shown in the table, the number of cells in the circumferential direction ranges from 180 to 360, indicating that the resolution in this direction changes from 2 cells to 1 cell per degree from G3 to G1.

	Axial	Radial	Circumferential
G1	281	101	360
G2	200	85	256
G3	140	51	180

Table 6.1: Number of cells in each direction of the computational grids in the wake region.

The basic information of the 3 computational grids used in the verification study is summarized in Table 6.2. h_i denotes the relative grid size and is defined by Eq. (2.28), N_W^i is the number of cells in the wake region, and N_T^i is the total number of cells in the computational grids. Note that the meshes in the outer domain are also refined accordingly in the $x - axis$ direction to ensure a smooth transition of the flow information through the sliding interfaces.

Grids	h_i	N_W^i [million]	N_T^i [million]
G1	1.000	10.17	34.15
G2	1.334	4.28	26.96
G3	2.006	1.26	17.46

Table 6.2: Computational grids and the corresponding relative grid sizes used in the verification study.

The information of the 3 time increments used in the calculations is provided in Table 6.3. The smallest temporal spacing is denoted as T1 while the largest is T3. t_j is the relative time increment defined by Eq. (2.29), and the real time increment is denoted by Δt_j. The last column is the time steps needed for the wind turbine to rotate a full cycle, e.g., $t_j = 1.0$ corresponds to a 0.75° rotation per time step in the simulations.

iterative convergence

The iterative convergence of a CFD simulation is represented by the level of residuals. Typically, the residuals are higher in simulations with larger Courant numbers [96]. Here, we define a

Time increments	t_j	Δt_j [s]	No. time steps per revolution
T1	1.000	0.0000975	480
T2	1.333	0.00013	360
T3	2.000	0.000195	240

Table 6.3: Time increments and the corresponding relative time steps used in the verification study.

local Courant number which is calculated based on the cells in the wake domain:

$$Co_w = U_x \frac{\Delta t}{\Delta x_w} \tag{6.1}$$

where U_x is the streamwise velocity, Δt is the time increment, and Δx_w is the minimum cell size of the wake region in the $x-$direction.

The Courant numbers for the 9 cases are summarized in Table 5.4. It can be observed that the G1T3 case has the largest Courant number while the G3T1 case has the smallest. The residuals of case G1T3 and case G3T1 are then presented in Fig. 6.3. Obviously, the L_2-norm of the residuals for both simulations remained at or under the level of 10^{-4} in the simulations. This indicates that the simulations are well converged and the iterative errors ϵ_{it} in the simulations are small and thus can be legitimately neglected in the estimations of numerical uncertainties.

	G1	G2	G3
T1	0.070	0.050	0.035
T2	0.093	0.066	0.046
T3	0.139	0.099	0.070

Table 6.4: Largest theoretical Courant numbers for all 9 simulations.

discretization uncertainties

The normalized mean wake deficit profiles (referred to as "deficit profiles" hereafter) and the normalized mean turbulence kinetic energy (TKE) profiles (referred to as "TKE profiles" hereafter)

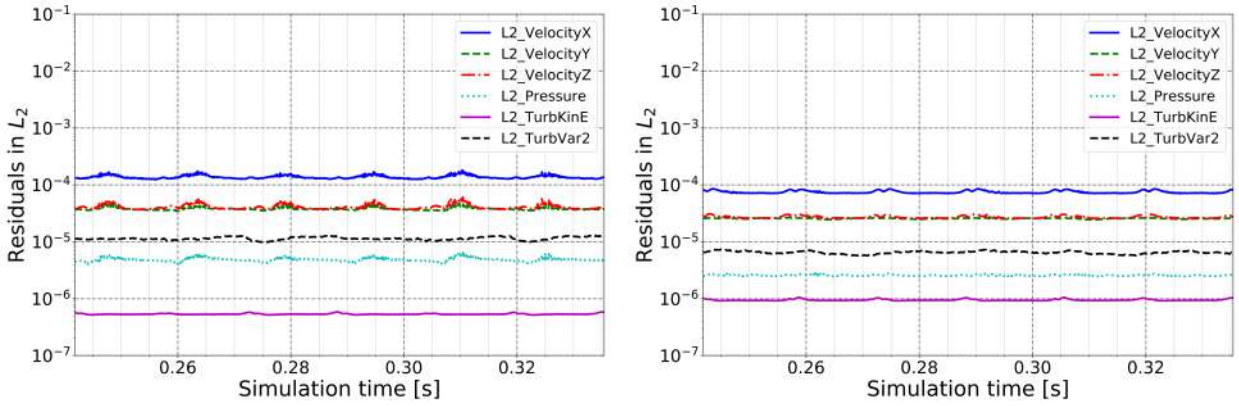

(a) L_2-norm of the residuals for G1T3.

(b) L_2-norm of the residuals for G3T1.

Figure 6.3: L_2-norm of the residuals for the cases with the largest and the smallest theoretical Courant numbers.

obtained from all 9 cases are shown in Figs. 6.4 and 6.5, respectively. Note that in the deficit profiles, as shown in Figs. 6.4a, 6.4c, and 6.4e, peaks in the profiles indicate low streamwise velocity values at the corresponding locations. For example in Fig. 6.4a, there are two peaks near $z/R = \pm 1.0$, indicating the streamwise velocity is low behind the blade tips (referred to as "tip peaks" hereafter). Furthermore, another peak can be identified around $z/R = -0.3$, as indicated by a yellow box. This third peak emerges due to the existence of the tower wake, causing the wake profiles to be asymmetric about the center, i.e. $z/R = 0$. This peak will be referred to as the "asymmetry peak" hereafter. The mechanism behind this phenomenon will be discussed in detail in the following sections. For the reason that the asymmetry in the deficit profiles is the leading challenge and the primary concern in the simulations of the BT1 wind turbine, in the current verification study, we will choose the values of the asymmetry peaks obtained from the different cases as the quantity to be used in the estimations of the discretization uncertainties. As shown in Figs. 6.4a, 6.4c, and 6.4e, the asymmetry peaks in the deficit profiles at different downstream locations are identified and indicated using yellow boxes, and a zoomed-in view is also provided. The asymmetry peaks in the TKE profiles are also indicated by using yellow boxes, as shown in Figs. 6.5a, 6.5c, and 6.5e. Then, as shown in Figs. 6.4b, 6.4d, 6.4f, 6.5b, 6.5d, and 6.5f, the

predicted values of the asymmetry peaks in the deficit and TKE profiles are rendered in two ways for clarity: 1) the results are grouped by the relative time increments and plotted as a function of relative grid size (left); 2) the results are grouped by the relative grid size and plotted as a function of relative time increment (right).

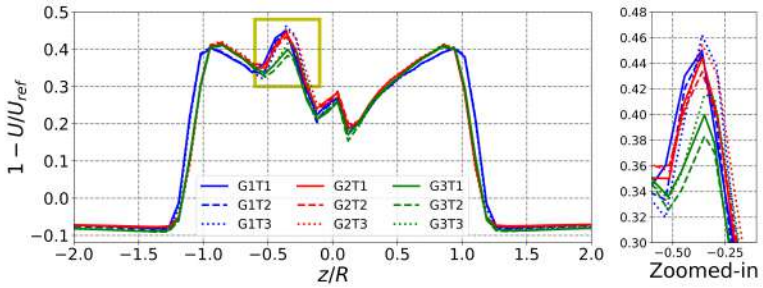

(a) Deficit profiles at 1 D downstream.

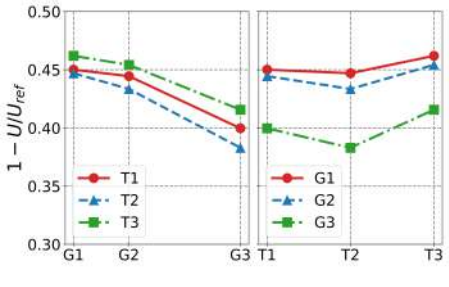

(b) Predicted values of the asymmetry peaks in the deficit profiles at 1 D downstream.

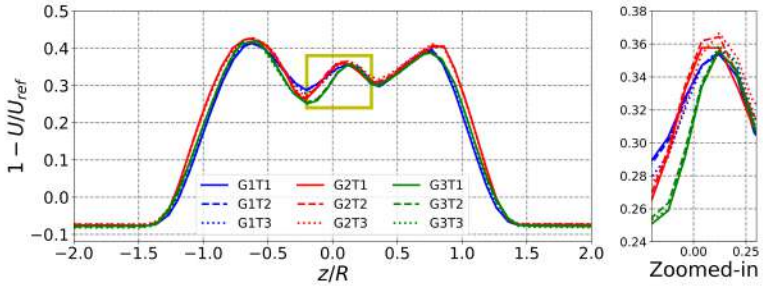

(c) Deficit profiles at 3 D downstream.

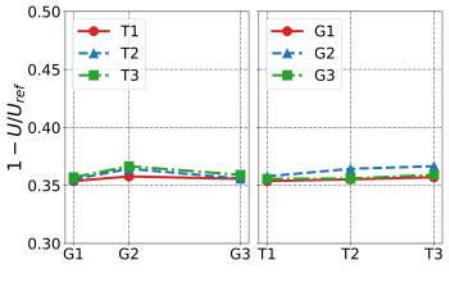

(d) Predicted values of the asymmetry peaks in the deficit profiles at 3 D downstream.

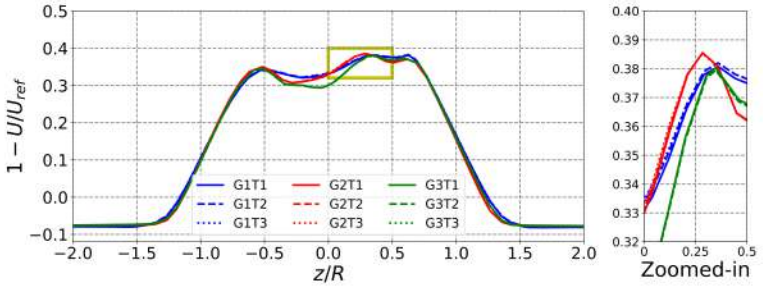

(e) Deficit profiles at 5 D downstream.

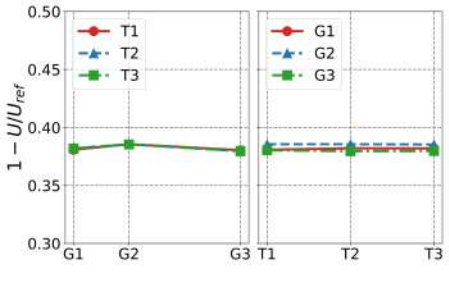

(f) Predicted values of the asymmetry peaks in the deficit profiles at 5 D downstream.

Figure 6.4: Deficit profiles obtained from all simulations.

Fig. 6.4 shows the deficit profiles obtained from all cases. In general, at each of the three downstream distances, the profiles obtained from all 9 cases are asymmetric about the center while being similar to each other. In addition, as shown in Figs. 6.4b, 6.4d, and 6.4f, the values of the asymmetry peaks are more sensitive to the refinement of the grid and time increment at 1

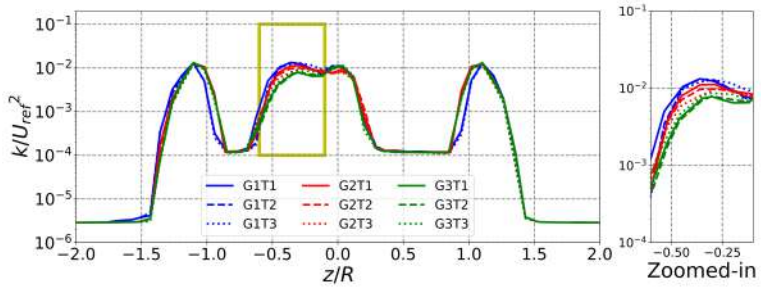

(a) TKE profiles at 1 D downstream.

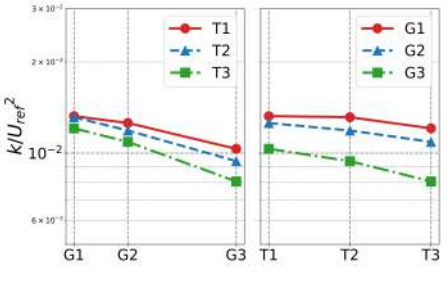

(b) Predicted values of the asymmetry peaks in the TKE profiles at 1 D downstream.

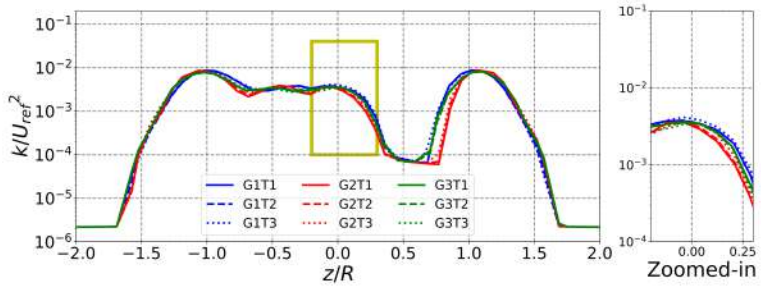

(c) TKE profiles at 3 D downstream.

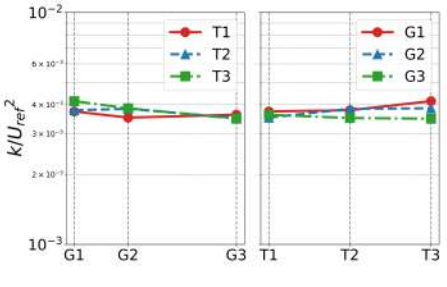

(d) Predicted values of the asymmetry peaks in the TKE profiles at 3 D downstream.

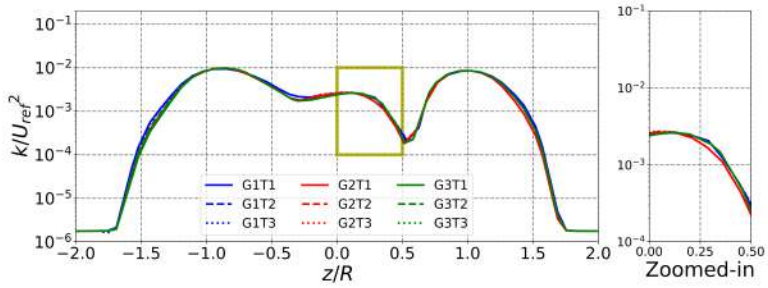

(e) TKE profiles at 5 D downstream.

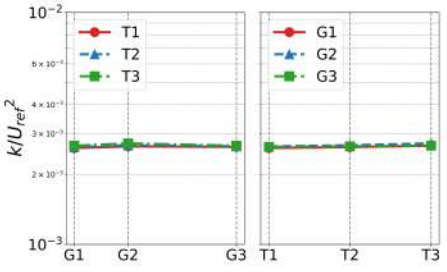

(f) Predicted values of the asymmetry peaks in the TKE profiles at 5 D downstream.

Figure 6.5: TKE profiles obtained from all simulations.

turbine diameter (D) downstream. As the downstream distance further increases, the values of the asymmetry peaks from different cases become close to each other. Fig. 6.5 shows the TKE profiles obtained from different cases. In accordance with the deficit profiles, the predicted TKE profiles are also asymmetric. The values of the asymmetry peaks of the TKE profiles are shown in Figs. 6.5b, 6.5d, and 6.5f. At 1 D downstream, similar to the deficit profiles, the influence of the refinement of the grid and time increment on the asymmetry peaks is clearly visible. However at 5 D downstream, the predicted values of the asymmetry peaks obtained from all cases are almost identical. This trend is in line with the observation from the deficit profiles.

Then, the verification procedure adopted in this study is applied to the obtained data sets, and the fitting planes are visualized in Fig. 6.6.

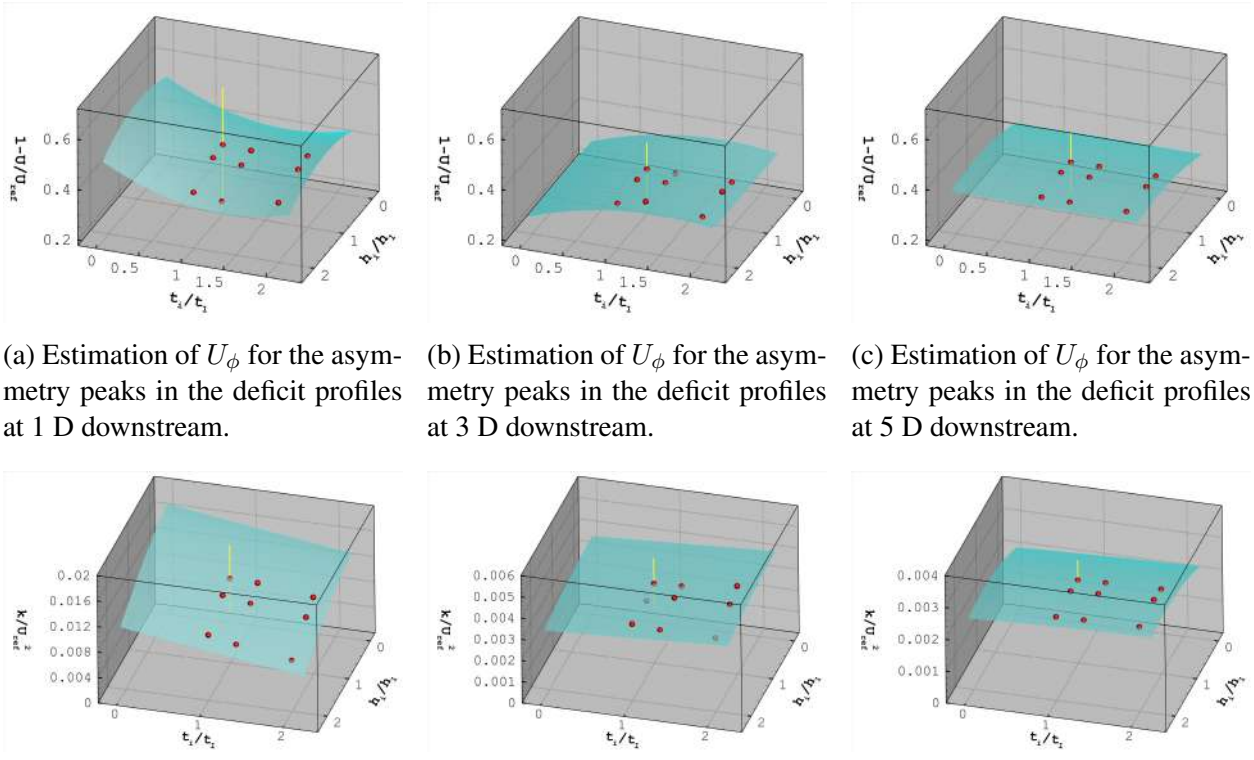

(a) Estimation of U_ϕ for the asymmetry peaks in the deficit profiles at 1 D downstream.

(b) Estimation of U_ϕ for the asymmetry peaks in the deficit profiles at 3 D downstream.

(c) Estimation of U_ϕ for the asymmetry peaks in the deficit profiles at 5 D downstream.

(d) Estimation of U_ϕ for the asymmetry peaks in the TKE profiles at 1 D downstream.

(e) Estimation of U_ϕ for the asymmetry peaks in the TKE profiles at 3 D downstream.

(f) Estimation of U_ϕ for the asymmetry peaks in the TKE profiles at 5 D downstream.

Figure 6.6: Discretization uncertainty (U_ϕ) estimations of the mean wake deficit and mean TKE profiles for case G1T1. The yellow lines represent the discretization uncertainties.

The discretization uncertainties (U_ϕ) are estimated for the results obtained by using G1T1 and are summarized in Tables 6.5 and 6.6. It can be observed in Table 6.5 that the maximum estimated value of U_ϕ for the asymmetric peaks appears at 1 D downstream, which is 50.4%. And then, with the increase of the downstream distance, the values of the numerical uncertainty decrease to around 30%. A similar trend is also observed for the U_ϕ of the TKE, as shown in Table 6.6 in which U_ϕ is 40.0% at 1 D downstream while decreasing to 24.2% at 5 D downstream.

Loc.	Extrapolated value, ϕ_0	Solution of G1T1, ϕ_{11}	Error ϵ_ϕ [%]	Uncertainty U_ϕ [%]
$1D$	0.526	0.450	14.4	50.4
$3D$	0.298	0.354	18.8	29.7
$5D$	0.343	0.381	11.1	30.7

Table 6.5: Summary of discretization uncertainties of the predicted asymmetry peaks in the deficit profiles.

Loc.	Extrapolated value, ϕ_0	Solution of G1T1, ϕ_{11}	Error ϵ_ϕ [%]	Uncertainty U_ϕ [%]
$1D$	1.73×10^{-2}	1.33×10^{-2}	23.1	40.0
$3D$	3.69×10^{-3}	3.74×10^{-3}	1.4	32.1
$5D$	2.10×10^{-3}	2.60×10^{-3}	23.8	24.2

Table 6.6: Summary of discretization uncertainties of the predicted asymmetry peaks in the TKE profiles.

Due to the fact that the residuals in the simulations were two orders of magnitudes lower than the discretization uncertainty, the total numerical uncertainty is thus assumed to be contributed solely by the discretization uncertainty. Therefore, the listed uncertainty ranges in Tables 6.5 and 6.6 will be adopted in the following validation study.

The deficit and TKE profiles obtained from G1T1 are then compared against the measurement, as shown in Fig. 6.7. The results in the present study are plotted as red lines, and the experi-

mental data are plotted as black squares. The uncertainty bars are also indicated by vertical red lines. For comparison purposes, results using other representative modeling approaches reported by Krogstad and Eriksen [3] and Ji et al. [6] are also presented here. Details of the different results are summarized in Table 6.7.

Numerical Results	**Rotor**	**Tower**	**Gov. Eq.**	**Turb. Closure**	**CFD Solver**
FRG-RANS w/o tower [3]	FRG	No	RANS	$k-\omega$ SST	STAR CCM+
FRG-RANS w/ tower [3]	FRG	Yes	RANS	$k-\omega$ SST	Ansys Fluent
AL-LES [3]	AL	No	LES	Sub-grid	EllipSys3D
AL-IB-LES [6]	AL	Yes (IB)	LES	Sub-grid	OpenFOAM

Table 6.7: Details of the different numerical methods compared in the wake simulations. The numerical methods adopted by the participants are denoted as: 1) FRG-RANS w/o tower [3] - RANS calculations using fully-resolved rotor geometry but without the tower; 2) FRG-RANS w/ tower [3] - RANS calculations using fully-resolved rotor geometry including the tower; 3) AL-LES [3] - LES simulations in which the rotor is modeled by the actuator line method and no nacelle or tower effect were accounted for; and 4) AL-IB-LES [6] - LES simulations in which the rotor is modeled by the actuator line method and the nacelle effect is modeled by the immersed boundary method.

6.1.3.2 Validation

At 1 D downstream, as shown in Fig. 6.7a, the present results successfully captured the asymmetry in the deficit profile, whereas all other results predicted symmetric profiles. Specifically, the present result is the only one that captured the asymmetric peak, although the magnitude and its location are slightly different from the measurement. For the TKE profiles, as shown in Fig. 6.7b, the current result matches the measurement in trend while being roughly 1 order of magnitude lower than it, except for in the range of $-0.5 < z/R < 0.2$. The asymmetry in the TKE profile is also successfully predicted. The AL-IB-LES method also predicted an asymmetric TKE profile and its magnitude almost matches the measurement perfectly. This is interesting because the same method failed to capture the asymmetry in the deficit profile. At 1 D downstream, the asymmetry peaks of the deficit and the TKE profiles measured in the experiment are within the estimated

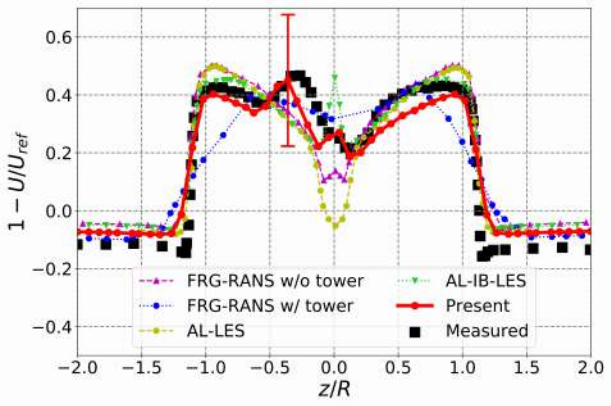

(a) Deficit profiles at 1 D downstream.

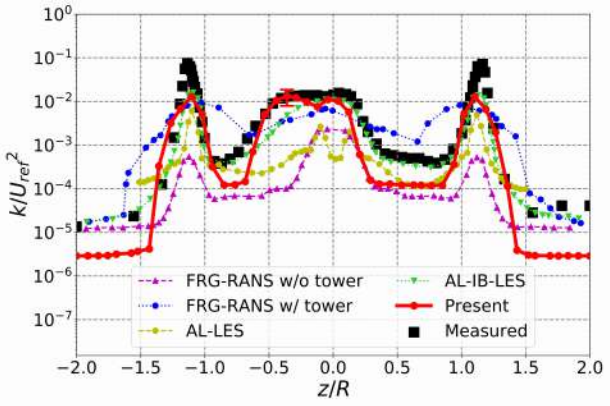

(b) TKE profiles at 1 D downstream.

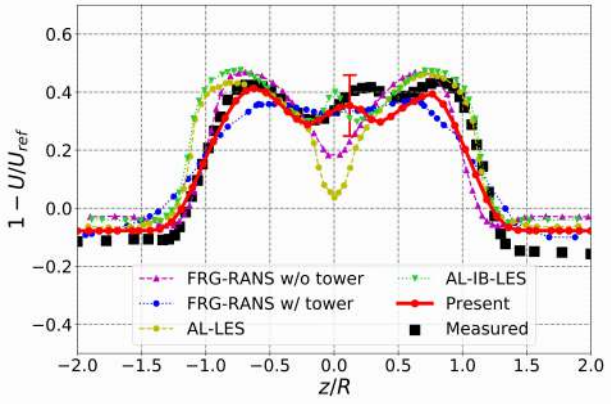

(c) Deficit profiles at 3 D downstream.

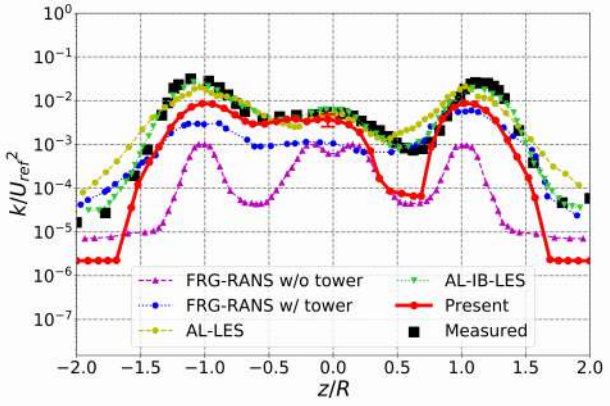

(d) TKE profiles at 3 D downstream.

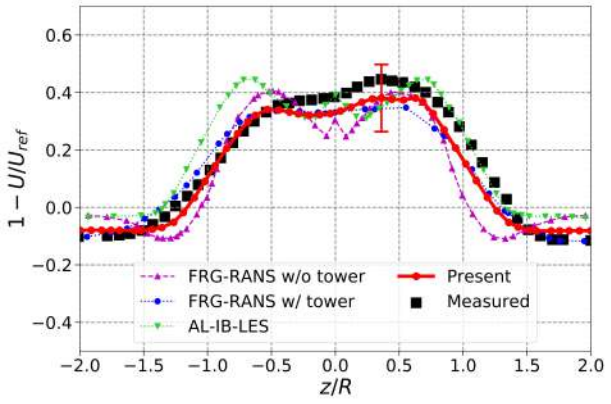

(e) Deficit profiles at 5 D downstream.

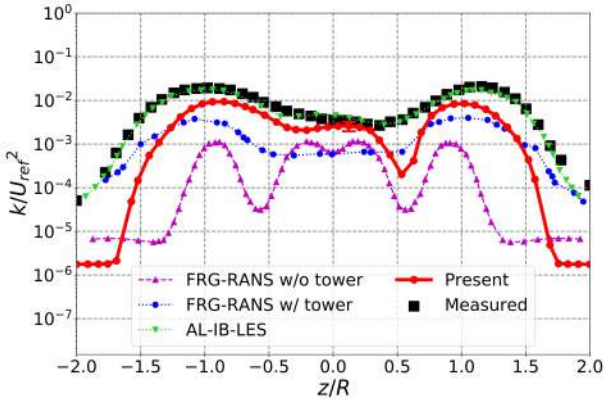

(f) TKE profiles at 5 D downstream.

Figure 6.7: Comparison of mean wake deficit and TKE profiles.

numerical uncertainty ranges, therefore, the numerical results are validated.

At 3 D downstream, as shown in Fig. 6.7c, the present results match the measured data well. The asymmetry in the measurement is captured by the present study while all other numerical results seem to give symmetric profiles. Further, compared to the deficit profile at 1 D downstream, the location of the asymmetry peak at 3 D downstream switches to the right-hand side as shown in the experimental data. This location-switch phenomenon is also successfully captured by the present study. For the TKE profiles, as shown in Fig. 6.7d, the present result matches the measurement in trend. However, an obvious difference is observed in the range of $0.25 < z/R < 0.75$ in which the TKE levels are 1 order of magnitude lower than the measurement. Comparing the measured data at 3 D downstream to the data at 1 D downstream, it suggest that the TKE in that region increases much faster in the experiment than it is in the simulation. A similar trend is found in the other two results obtained also from RANS calculations. However, in the two LES calculations, the TKE profiles at 3 D downstream match the measured data well. This is, again, interesting, because both LES simulations failed to capture the asymmetry in the deficit profiles, while successfully reproducing the TKE levels. At 3 D downstream, the asymmetry peaks of the deficit and TKE profiles measured in the experiment are within the estimated numerical uncertainty ranges, thus the predicted results are validated.

At 5 D downstream, as shown in Fig. 6.7e, the present results match the measured data well. Again, the present result is the only one that successfully captured the asymmetry in the deficit profile. For the TKE profiles, as shown in Fig. 6.7f, the present result matches the measured data in trend. However, an obvious difference still exists in the range of $0.25 < z/R < 0.75$ in which the TKE level is significantly under-predicted. The profile obtained by the AL-IB-LES method, on the other hand, matches the measured TKE profile perfectly while failing to capture the asymmetry in the deficit profile. At 5 D downstream, the asymmetry peaks of the deficit and TKE profiles in the measurement are within the estimated numerical uncertainty ranges, thus the validation of the numerical results is achieved.

By comparing the profiles obtained from CFD simulations, i.e. RANS and LES, against the

experimental data, it suggests that the difference between the present results and the measurement in the TKE profiles may be due to the limitations of the turbulence model used in the present study. The 2-equation turbulence models are based on the Boussinesq hypothesis and the production of the turbulence kinetic energy is assumed to be isotropic. However, due to the rotation of the wind turbine, strong non-isotropy in the turbulence is present thus the 2-equation models may not be able to accurately predict the TKE levels in the wind turbine wake. However, it should also be concluded that even though in some particular regions the TKE levels are under-predicted, the overall profiles obtained by the present study match the experimental data well.

6.1.4 Flow Details

In this section, the instantaneous flow fields are visualized to elucidate the underlying mechanism leading to the observations in the wake profiles, i.e. the asymmetry in the deficit profiles and the location-switch of the asymmetry peaks. The flow field obtained from the G1T1 case will be adopted in the following discussions.

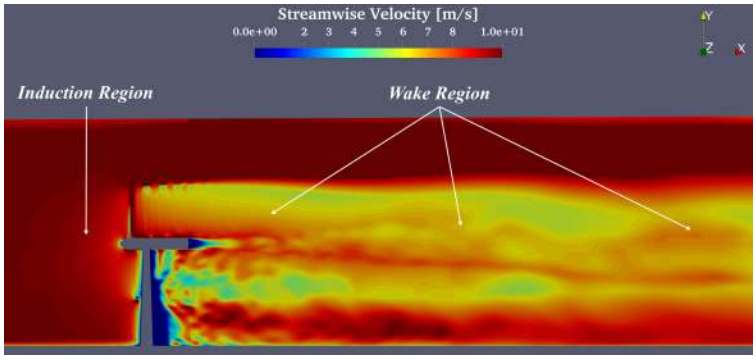

Figure 6.8: Streamwise velocity contours on the xOy-plane.

To provide a general idea of the obtained wind turbine wake, the streamwise velocity contours on the xOy-plane and the vortex structures of the wind turbine wakes are visualized. First, it can be seen in Fig. 6.8 that an induction region, characterized by a low-velocity region, is formed in front of the turbine. In the wake region, the flow velocity is lower than the free stream velocity,

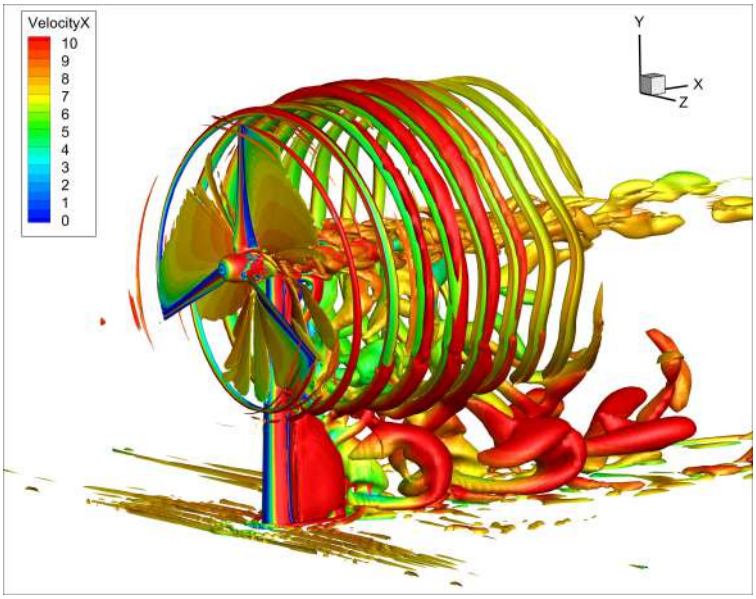

Figure 6.9: Iso-surfaces of $Q = 1000$, colored by streamwise velocity.

and complicated flow structures exist. Then, as shown in Fig. 6.9, iso-surfaces of Q value [99, 100] equals 1000 are presented to show the wake structures. Note that the Q iso-surfaces are colored by streamwise velocity. It can be seen from the figure that the helical blade tip vortex, the blade root/nacelle vortex, and the tower vortex are clearly resolved. The three-dimensional vortex structures provide a good general idea of the wind turbine wakes, however, the details of the interactions between the vortex structures, i.e. the blade-generated wakes (referred to as blade wakes hereafter) and the tower wake, can be hardly identified in this view. Therefore, we will take advantage of the cross-sectional views of the computational domain in the following discussions.

6.1.4.1 Skew of the tower wake

According to Newton's third law of motion, there must be an equal and opposite reaction for every action. In the case of a rotating wind turbine, the flow applies a torque on the wind turbine and makes it rotate, and thus conversely the wind turbine must impart an opposite torque on the flow. Therefore, the flow behind a wind turbine rotates in the opposite direction to that turbine [14, 101]. In the current work, as mentioned earlier, the turbine is rotating in the negative direction about the $x - axis$. Therefore, as a result of the conservation of angular momentum and the fact

that the wind turbine experiences a positive torque at TSR = 6, the blade wakes are forced to rotate in the positive direction about the $x - axis$ as opposed to the wind turbine.

In the case of flow passing a circular cylinder, the vortices shed from the cylinder should follow the streamwise direction. However, in the current study, due to the rotation of the blade wakes, the incoming flow felt by the tower will no longer strictly point to the positive $x - axis$ but will have a transverse component that points to the negative $z - axis$. As a result, the tower wake is skewed and its propagation will have a directional preference.

Fig. 6.10 shows the skewed tower wake at three different vertical locations ($y - axis$). The streamwise velocity contours are plotted on three $y-$normal planes, i.e. $y = -0.1\ m$, $y = -0.2\ m$, and $y = -0.3\ m$, and the center line of each plane is indicated by a black dash-dotted line. For a better understanding of the wake structure, the streamwise velocity contours on the $x-$normal plane at 3 D downstream ($x = 2.682\ m$) are also visualized. In Fig. 6.10, the color of the tower wake is blue and green, indicating its velocity is slower than the blade wakes. It can be clearly seen that the propagation of the tower wake has a directional preference, and this phenomenon will break the symmetry of the downstream wake profiles.

6.1.4.2 Asymmetry of the wake profiles

The instantaneous flow field is shown in Fig. 6.11. For the left-hand side figures, the instantaneous streamwise velocity contours at the 25th revolution are plotted on the $x-$normal planes at different downstream locations. White dashed lines indicate the hub height locations, i.e. $y = 0$. The black arrows represent the velocity vectors on the $x-$ normal planes. In the right-hand side figures, the instantaneous profiles at the hub height are shown as the red solid lines, and the envelopes of the instantaneous profiles are shown as the grey bands. The measured and predicted mean deficit profiles are also plotted. All the figures are shown as if the observer is looking toward the positive direction of the $x - axis$. Therefore, the wind turbine rotates in the counter-clockwise direction and the blade wakes rotate in the clockwise direction in Figs. 6.11a, 6.11c, and 6.11e.

At 1 D downstream, as shown in Fig. 6.11a, a clear wake region is captured. The edge between the turbine wake and the free stream can be clearly identified. It can be observed that the tower

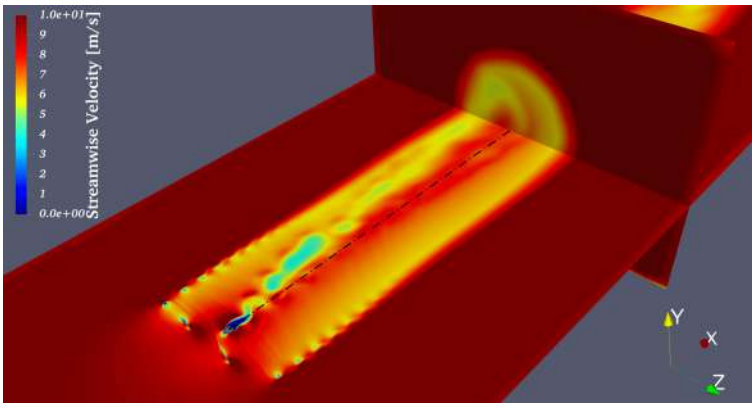

(a) Velocity contours at $y = -0.1\ m$.

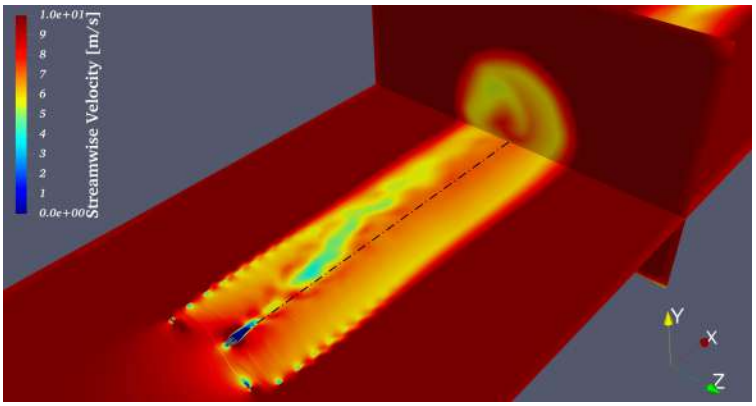

(b) Velocity contours at $y = -0.2\ m$.

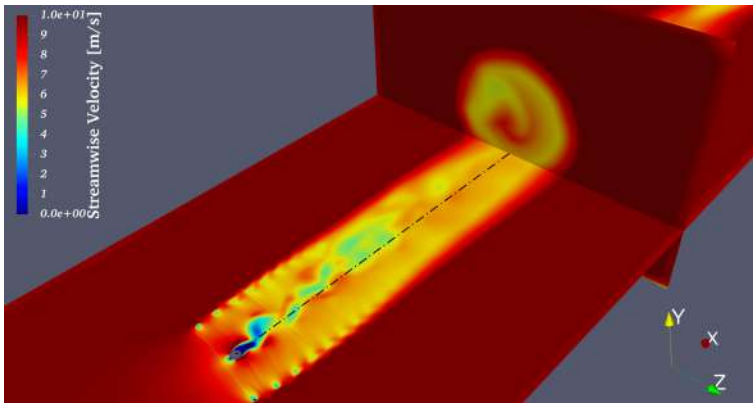

(c) Velocity contours at $y = -0.3\ m$.

Figure 6.10: Skewed tower wake at different vertical locations.

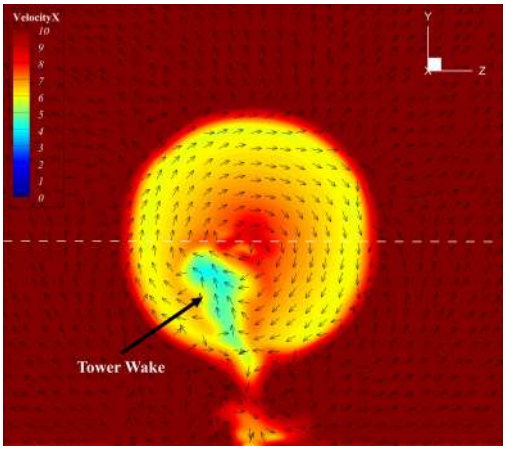

(a) Velocity contours at 1 D downstream.

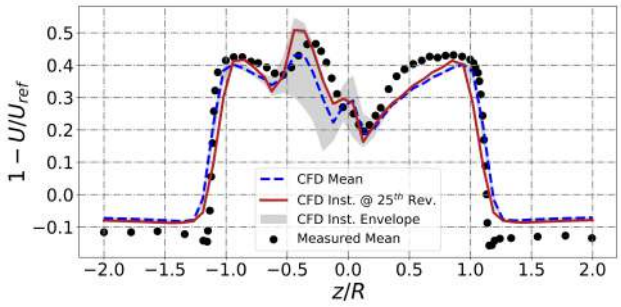

(b) Instantaneous deficit profiles at 1 D downstream.

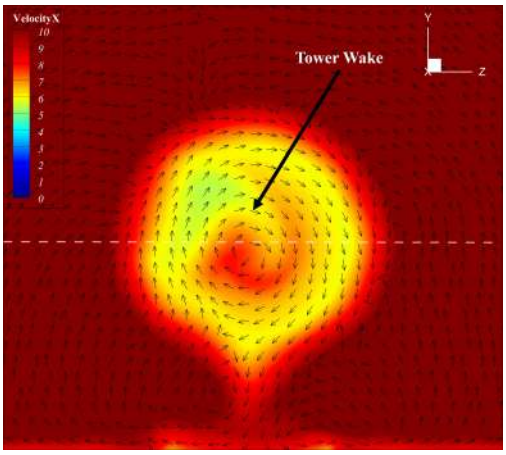

(c) Velocity contours at 3 D downstream.

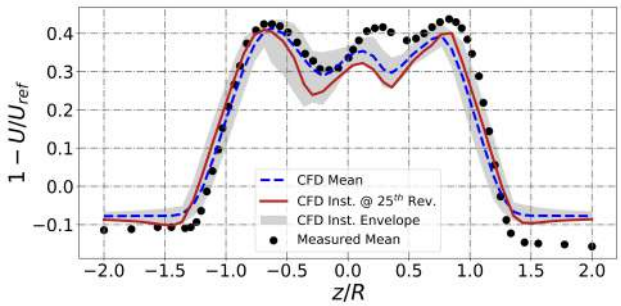

(d) Instantaneous deficit profiles at 3 D downstream.

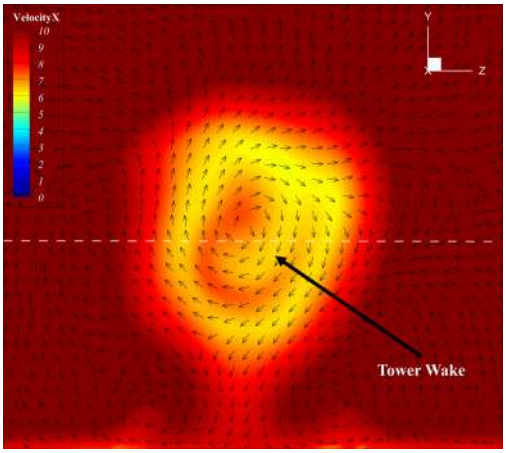

(e) Velocity contours at 5 D downstream.

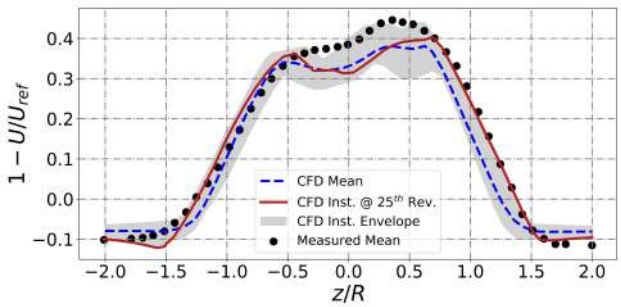

(f) Instantaneous deficit profiles at 5 D downstream.

Figure 6.11: Instantaneous wake contours and profiles.

wake is slower compared to the blade wakes and is on the left of the tower. Although the tower is below the hub, the tower wake is brought to the hub height by the rotating blade wakes. Therefore, a peak in the deficit profile is expected in the corresponding location. As shown in Fig. 6.11b, an asymmetry peak is shown at $z/R = -0.25$, indicating that the velocity at the hub height is significantly affected by the tower wake. In addition, the envelope of the instantaneous profiles has a wider width in the range of $-0.75 < z/R < 0.25$. Compared to the narrow envelope in the range of $0.25 < z/R < 1.0$, it shows that the flow is highly unsteady in the range of $-0.75 < z/R < 0.25$ due to the influence of the tower wake.

At 3 D downstream, the wake characteristics change. The tower wake is carried by the blade wakes to a higher position above the hub height, and its shape is also distorted. Part of the tower wake has merged with the tip wakes and cannot be distinguished. For the deficit profiles, as shown in Fig. 6.11d, comparing the curves in the ranges of $-1.25 < z/R < -0.75$ and $0.75 < z/R < 1.25$, the latter one has a steeper slope than the former. This indicates an enhanced mixing of the turbulence due to the presence of the tower wake on the negative $z-axis$, and thus the momentum inside and outside the wake region exchanges more efficiently. As a result, the velocity deficit in that region will be smoothed sooner as the downstream distance increases compared to that on the positive $z - axis$. Further, the asymmetry peaks are still observed while its location switches to the positive $z - axis$. This location-switch phenomenon can be easily understood by looking at the velocity contour plot, i.e. Fig. 6.11c, in which the tower wake is carried and distorted by the rotating turbine wake.

Finally, Fig. 6.11e shows the velocity contours at $x = 5$ D. The tower wake is still visible at 5 D downstream. By comparing to Fig. 6.11c, it is clear that the tower wake is rotating in the clockwise direction. For the deficit profiles, the slopes of the profiles around the tip locations are further decreased and the profiles are overall smoother than the profiles at 3 D downstream. Although not as apparent as it is at the previous two downstream locations, the effect of the tower wake is still visible and is characterized as the asymmetry peak at around $z/R = 0.25$. The location of the asymmetry peak is in line with the location of the tower wake shown in Fig. 6.11e.

From the above observations and discussions, the following conclusions can be drawn.

- The asymmetry of the deficit profiles is caused by the tower wake. Although the tower is below the hub height ($y < 0$), the tower wake is lifted to upper positions by the rotating blade wakes. As a result, the deficit profiles at the hub height are significantly affected by the slow tower wake. This tower effect is characterized as the asymmetry peaks in the deficit profiles.

- The location-switch phenomenon of the asymmetry peaks is owing to the rotation of the blade wakes. The tower wake is carried by the blade wakes and rotates in the clockwise direction. At 1 D downstream, the tower wake is propagating to the left. However, due to the rotation of the blade wakes, the tower wake is distorted and the position of the wake is changing as the downstream distance increases. As a result, the position of the asymmetry peak changes as the downstream distance increases.

- It is also worth pointing out that although the position of the asymmetry peak changes with downstream distance, at a fixed downstream location, the position of the peak does not vary significantly over time. As discussed earlier, the rotation of the blade wakes is the driving force that makes the tower wake skew, and eventually breaks the symmetry in the downstream wake profiles. Therefore, because the turbine blades are rotating with a constant angular velocity, the blade wakes should also rotate at a steady speed. As a result, the path along which the tower wake propagates is relatively stable and will not vary significantly with time. This can be proved by the envelopes of the instantaneous wake profiles as shown in Figs. 6.11b, 6.11d, and 6.11f. It can be observed that although the magnitudes of the asymmetry peaks are changing over time, the position of which at each of the fixed downstream distances does not vary evidently.

- We confirm that the asymmetry in the wake profiles is physical and it is not a measurement error as discussed and suspected in some previous studies [6].

- We demonstrated that the RANS equations coupled with the $k-\omega$ SST turbulence model adopted in the current study is capable of capturing the asymmetry in the wake characteristics of the BT1 turbine.

6.1.4.3 Wake interactions

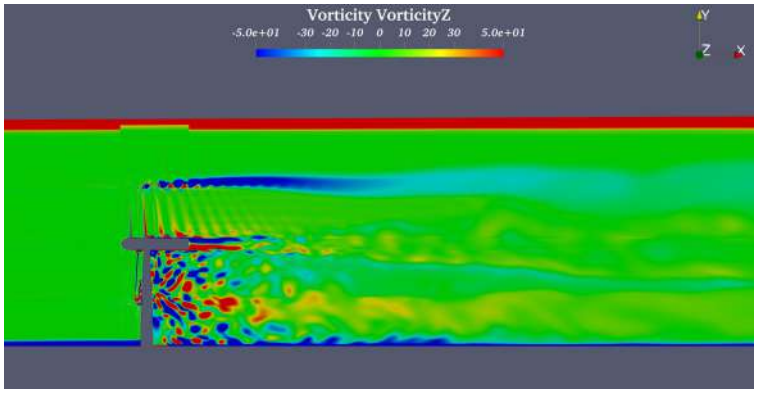

Figure 6.12: Z-Vorticity contours on the xOy-plans.

The wake structure of the wind turbine on the center $z-$normal plane (xOy-plane) is shown in Fig. 6.12. In general, three different flow regions can be identified from this figure. For the flow region above the hub height, i.e. $y > 0$, a steady and clear blade vortex structure can be observed. The blade wakes are visible up to roughly 1.5 D downstream, and then gradually distorted and dissipated. However, for the flow region below the hub height, i.e. $y < 0$, a highly unsteady and disordered flow pattern is presented compared to the flow pattern above the hub height. The blade wakes are not distinguishable in this wake region. This is a result of the interaction between the blade wakes and the tower wake. As can be observed in the figure, the highly complicated vortex structures are observed behind the tower. Further, for the flow region above the ground but below the lowest position of the blade tips ($ground < y < -R$), the vortex structure is solely generated by the tower wake, i.e. no blade wakes, but is only visible in the near wake region. As the downstream distance increases, due to the three-dimensional nature of turbulence, that tower

vortex is distorted by the vortices from upper regions and soon becomes highly unsteady and eventually dissipated.

The above discussions are more transparent by leveraging the cross-sectional slices of the flow field at different y locations. Fig. 6.13 shows the velocity contours at three selected y locations, i.e. $y = +0.5R$, $y = -0.5R$, and $y = -1.5R$, which respectively represent the wake structure consisting of solely the blade wakes, the blade wakes and the tower wake, and solely the tower wake.

In Fig. 6.13a, it can be observed that the blade wakes remain axisymmetric up to about 1.5 D downstream. As the downstream distance increases, as discussed earlier, the tower wake is lifted by the rotating blade wakes, and thus even for the flow region above the hub height, i.e. $y > 0$, interaction between the blade wakes and the tower wake will occur. At $y = -0.5R$, as shown in Fig. 6.13b, the interaction between the blade wakes and the tower wake can be clearly seen, and the propagation of the tower wake has an obvious directional preference, as discussed in the previous sections. However, at $y = -1.5R$ as shown in Fig. 6.13c, the tower wake propagates along the streamwise direction, and no evident directional preference is observed. This is because the tower wake in this flow region is away from the rotating blade wakes, and thus the propagation direction of it will be less affected. These distinctions among the flow structures in the three different flow regions reveal the importance of resolving the tower structure for accurate wind turbine simulations.

6.2 FANS Simulations

In this section, CFD results of the wake characteristics of NTNU BT1 wind turbine obtained by using FANS will be presented. First, the computational domain and grid generation will be discussed and the numerical settings will be introduced. Then the wake profiles of the NTNU BT1 wind turbine at different downstream locations will be presented, and the results will be compared against the experimental data and with other numerical results. Finally, the flow field will be visualized to show the wake structures and contours.

The CFD simulations for this study using FANS are performed on the Grace cluster of the

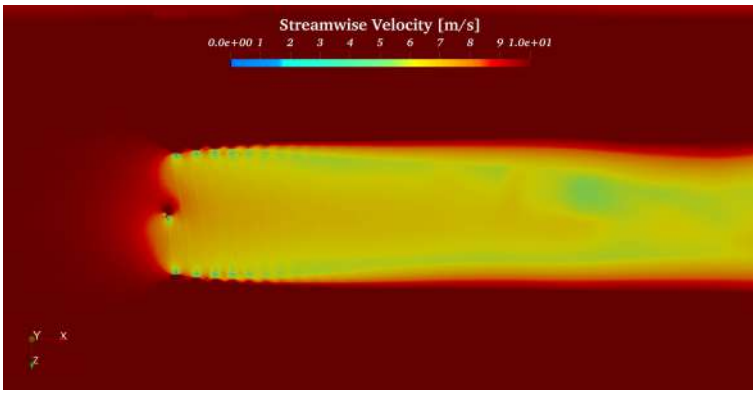

(a) Velocity contours at $y = +0.5R$.

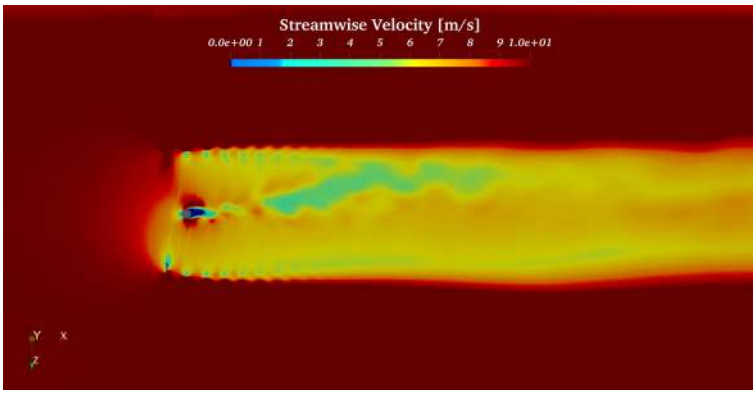

(b) Velocity contours at $y = -0.5R$.

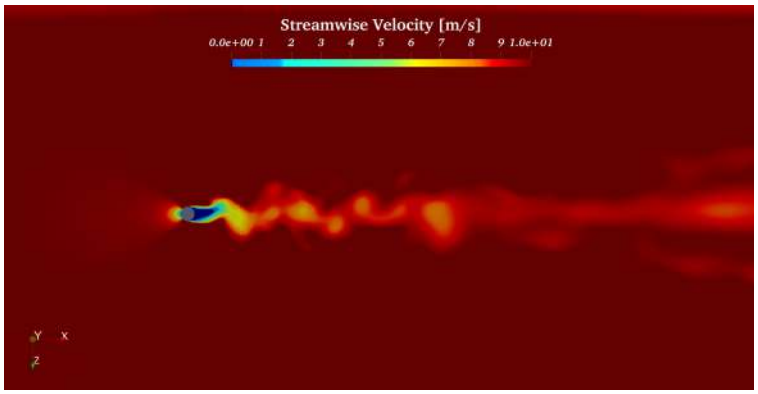

(c) Velocity contours at $y = -1.5R$.

Figure 6.13: Comparison of velocity contours at different y locations.

HPRC at TAMU with the Intel Xeon 6248R (Cascade Lake) 3.0GHz 24-core processors. 64 cores are used for each of the simulations and the computational time for a single simulation is approximately 10 days. More details on the consumed computational resources will be given in Section 6.3.

6.2.1 Computational Domain and Grid Generation

The computational domain and grid structure used in the current FANS simulations have already been introduced in section 5.2.1. For the sake of brevity, no repeated introduction will be given here. Here, in the CFD simulations targeting the wake characteristics of the BT1 wind turbine, grid G1 as described in section 5.2.3 will be adopted, and the only modification of the grid is that the grid resolution in the wake region is significantly increased to capture the wake characteristics of the wind turbine. As a result, the total number of grid points is approximately 24 million.

6.2.2 Numerical Settings

A uniform inflow is specified at the inlet, and the linear-extrapolation boundary condition in FANS is specified at the outlet. No-slip condition is applied to the surfaces of the wind turbine including blades, hub, nacelle, and tower. For the wind tunnel walls, a slip-wall condition is used. The boundary condition for the surfaces of overset grid blocks that overlap with other blocks is set to "interior boundary surfaces". Interpolation will be performed using the flow information from the donor grids. The two-layer $k-\epsilon$ turbulence model is adopted for the turbulence closure, as described in 2.3.2. The time step size is chosen such that the turbine will rotate 3 degrees in each time step.

6.2.3 Wake Profiles

The mean velocity deficit and the TKE profiles at 1, 3, and 5 D behind the wind turbine are shown in Fig. 6.14. The black dots are the measured time-averaged data in the experiment, and the blue lines are the mean velocity deficit profiles (referred to as deficit profiles) and the TKE profiles calculated by FANS. For comparison purposes, results using other representative modeling

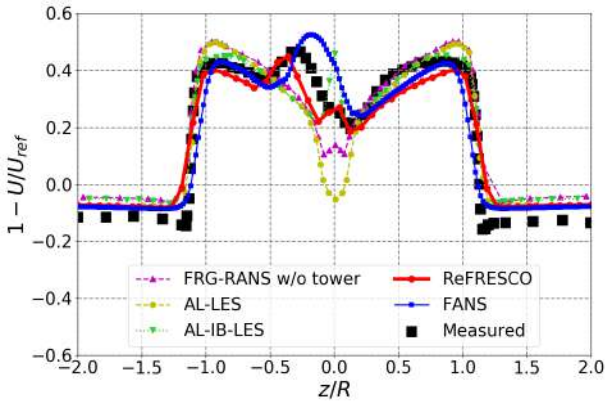

(a) Deficit profiles at 1 D downstream .

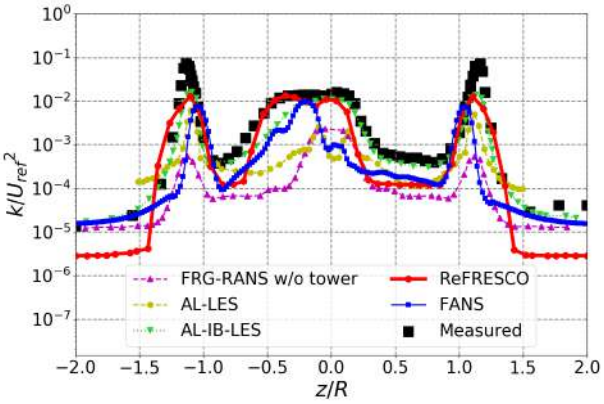

(b) TKE profiles at 1 D downstream.

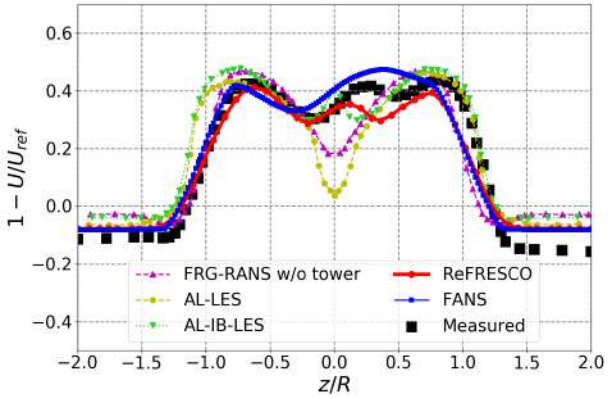

(c) Deficit profiles at 3 D downstream.

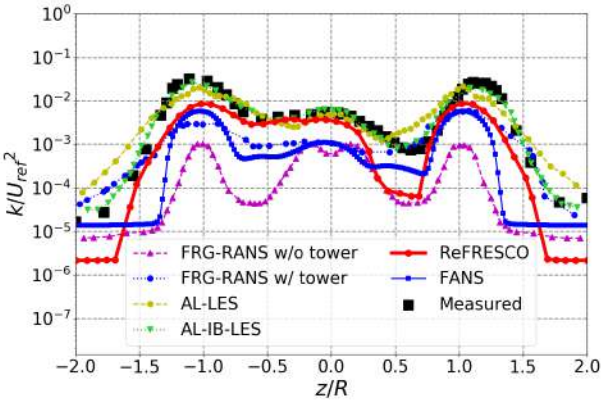

(d) TKE profiles at 3 D downstream.

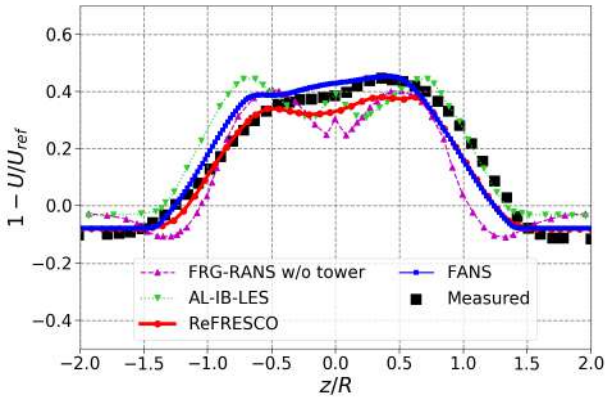

(e) Deficit profiles at 5 D downstream.

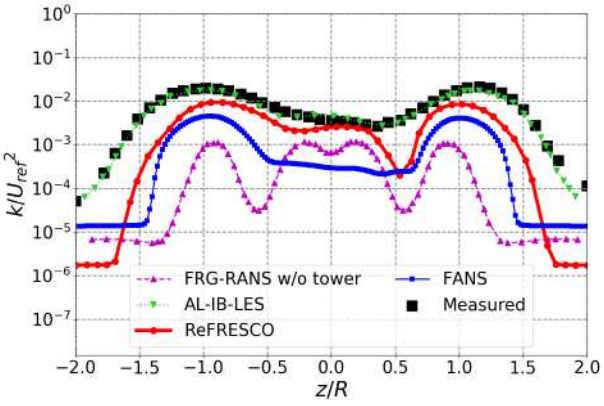

(f) TKE profiles at 5 D downstream.

Figure 6.14: Wake profiles obtained from FANS. The results are compared against the experimental measurement and with other numerical results including ReFRESCO results.

approaches reported by Krogstad and Eriksen [3] and Ji et al. [6] are also presented here. For the details of the different numerical results please refer to Table 6.7. In addition, the results obtained by using ReFRESCO are also plotted here as red lines.

For the deficit profile at 1 D downstream, as shown in Fig. 6.14a, the FANS prediction matches the measurement well. The result successfully captures the asymmetry in the deficit profile while the magnitude and the location of the asymmetry peak slightly deviate from the measurement. As discussed earlier, the ReFRESCO results also predict an asymmetry deficit profile and match the measurement well. For the other methods, i.e., FRG-RANS w/ tower, AL-LES, and AL-IB-LES, the results are all symmetric. For the TKE profiles at 1 D downstream, as shown in Fig. 6.14b, the FANS prediction matches the measurement in trend, i.e., the asymmetry in the TKE profile is successfully captured while being roughly 1 order of magnitude lower than it.

For the deficit profile at 3 D downstream, as shown in Fig. 6.14c, the present results match the measured data in trend. The asymmetry in the measurement is captured in the FANS result while the magnitude and the location of the asymmetry peak are moderately different from the experimental data. Note that as described in ReFRESCO results, the location-switch of the asymmetry peak from 1 D to 3 D downstream in the experimental data is also reproduced in the FANS result. In addition, as can be seen in the figure, FANS slightly over-predicted the magnitude of the asymmetry peak while ReFRESCO under-predicted it. For all the other methods, the predicted deficit profiles are symmetric. The FANS prediction of the TKE profiles at 3D downstream, as shown in Figure 6.14d, follows the same trend as the measurement but is approximately one order of magnitude lower. Comparing the FANS result with the measured data at 3 D downstream, it can be concluded that the shape of the predicted TKE profile resembles measurement. The sudden decrease of the TKE level between $0.25 < z/R < 0.75$ predicted by ReFRESCO is not observed in the FANS result.

For the deficit profile at 5 D downstream, as shown in Fig. 6.14e, the present results match the measured data well. The asymmetry in the measurement is successfully captured in the FANS result. For all the other methods except ReFRESCO, the predicted deficit profiles are symmetric.

For the FANS prediction of the TKE profiles at 5 D downstream, as shown in Figure 6.14f, it follows the same trend as the measurement but is, again, roughly one order of magnitude lower. Also, the shape characteristics in the measured profile are reproduced in the FANS prediction.

As discussed earlier in section 6.1.3.2, the deviation between the predicted and the measured TKE profiles in magnitude could be due to the limitation of the two-equation turbulence closure models used in the current study. Detailed discussions regarding this issue have been provided in section 6.1.3.2.

6.2.4 Flow Details

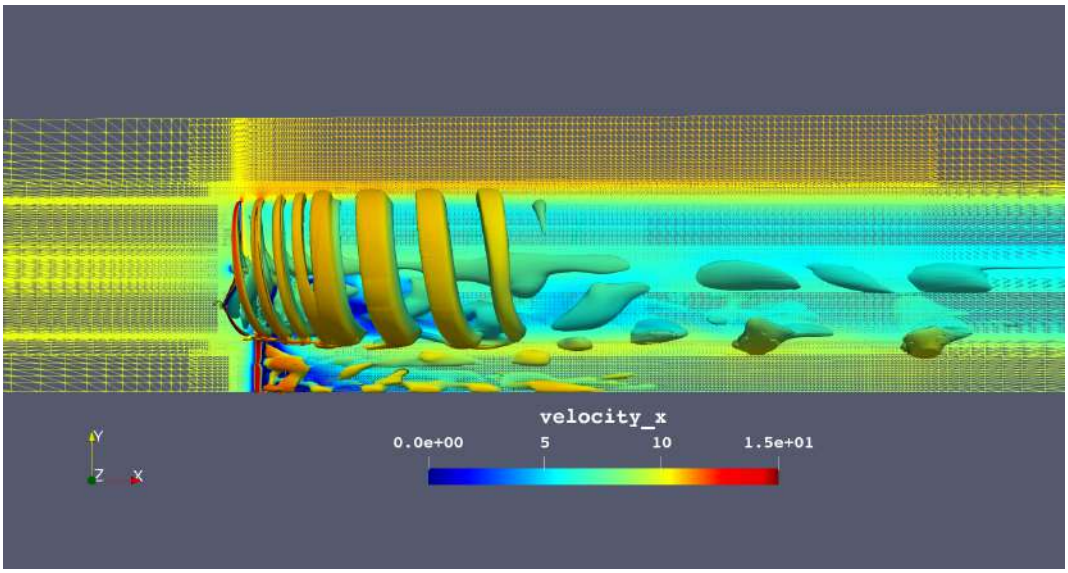

Figure 6.15: Iso-surfaces of Q, colored by streamwise velocity.

As shown in Fig. 6.15, the iso-surfaces of Q are visualized first to give an overview of the wake structure. The cross-section of the domain, i.e., the $y0x$ plane shown in wire-fire is also visualized to illustrate the overset grid structure. It can be seen that the tip helical vortices can be identified until approximately 3 diameters downstream and gradually dissipated. In contrast, the root and nacelle vortices traveled longer further downstream.

Fig. 6.16 also shows the iso-surfaces of Q but the iso-surfaces are presented in wire fires.

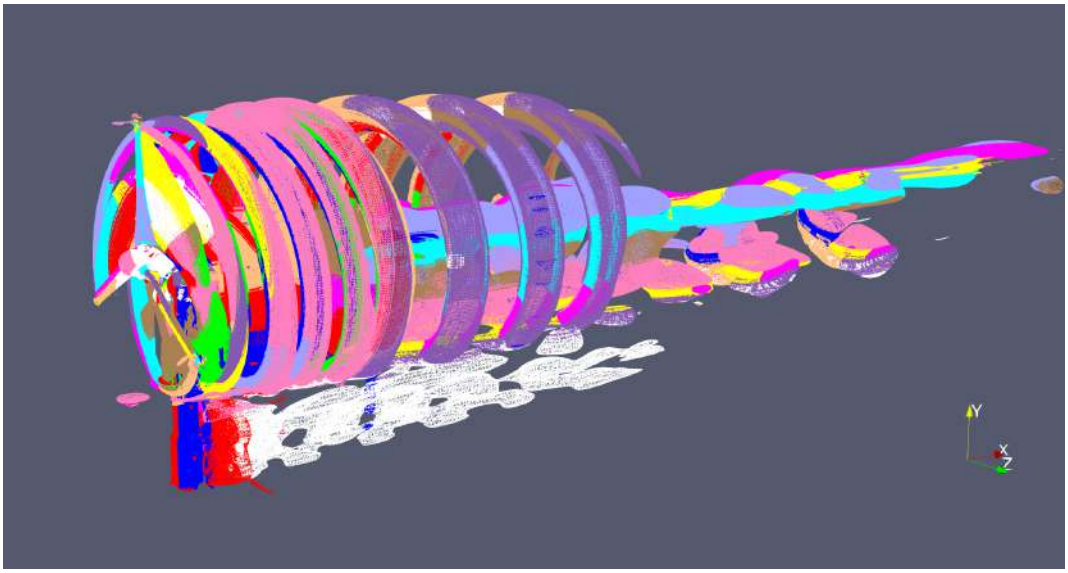

Figure 6.16: Iso-surfaces of Q shown in wire fire. Different colors indicate different overset grid blocks.

Different colors in the figure indicate different overset blocks. It can be observed that the surfaces are continual and smooth reassuring that the interpolation of flow information among different overset grid blocks is correctly performed in FANS simulations.

Fig. 6.17 shows the y normal planes at three different y locations which represent different flow regions, i.e., the flow regions above the hub height ($y = 0.3\,m$), at the hub height ($y = 0\,m$), and below the hub height ($y = -0.3\,m$). It can be observed that in Fig. 6.17b and Fig. 6.17c, the tower wake is skewed by the rotating blade wakes thus the flow profiles downstream the wind turbine will no longer be symmetric.

Fig. 6.18 shows the instantaneous velocity contours and the corresponding deficit profiles at different downstream locations. It can be clearly seen that the tower wake is carried by the rotating blade wakes to different positions as the downstream distance increases. This phenomenon has been thoroughly discussed in Section 6.1.4.2. For the sake of brevity, repeated discussion will not be made here. However, it is worth pointing out that in Fig. 6.18f, the slope of the predicted profile in the range of $-1.5 < z/R < -0.5$ is higher than the experimental data. This is due to the fact that turbulence levels predicted in FANS simulations are one order of magnitude lower than the

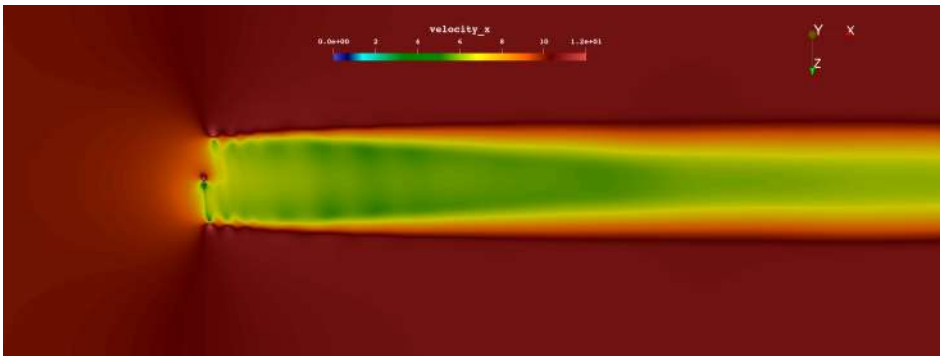

(a) Velocity contours at $y = +0.3\ m$.

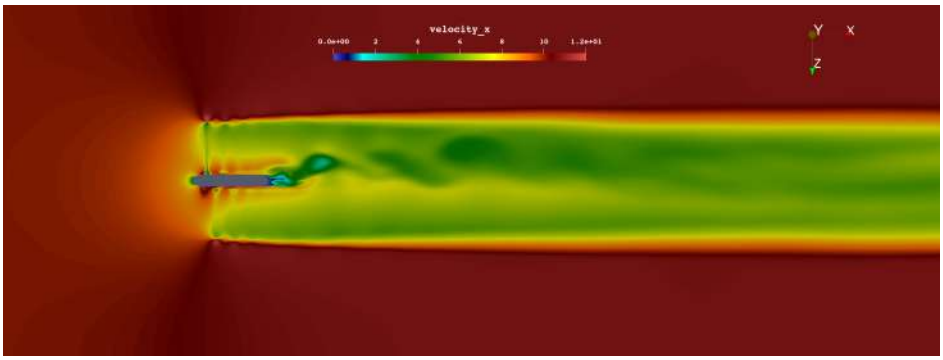

(b) Velocity contours at $y = -0\ m$.

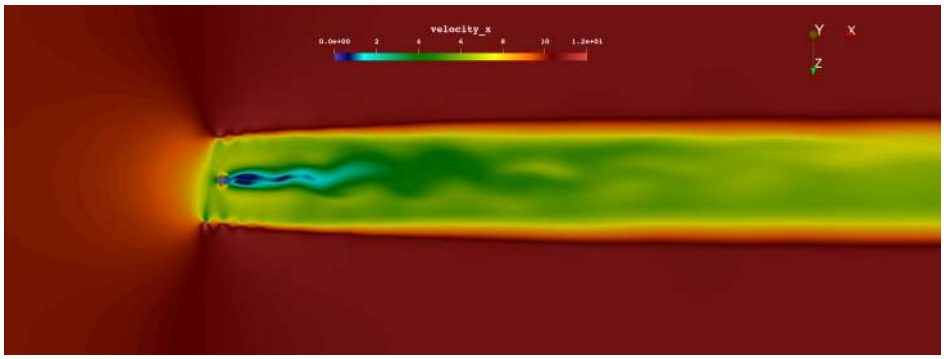

(c) Velocity contours at $y = -0.3\ m$.

Figure 6.17: Skewed tower wake at different vertical locations.

measurement, which leads to insufficient turbulence mixing, and thus the velocity profiles were not smoothed as fast as they were in the experiment.

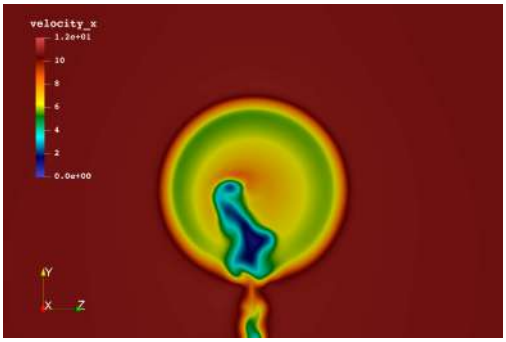

(a) Velocity contours at 1 D downstream.

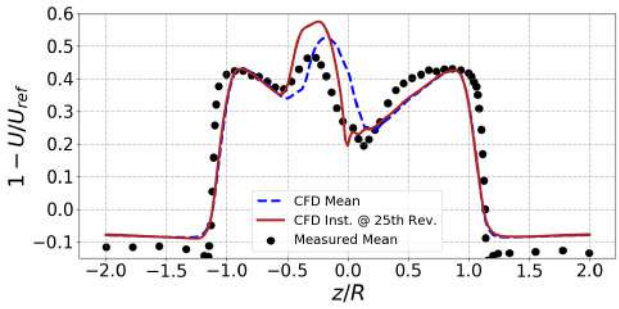

(b) Instantaneous deficit profiles at 1 D downstream.

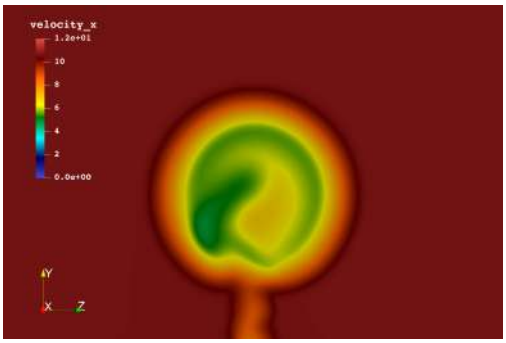

(c) Velocity contours at 3 D downstream.

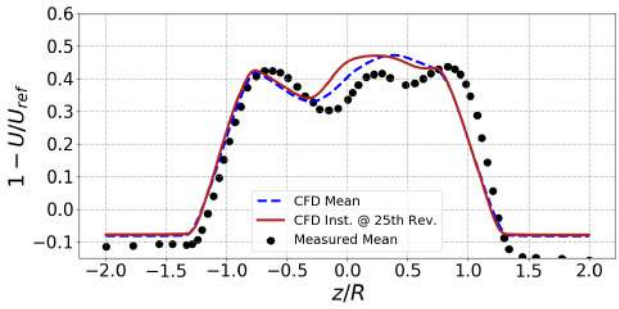

(d) Instantaneous deficit profiles at 3 D downstream.

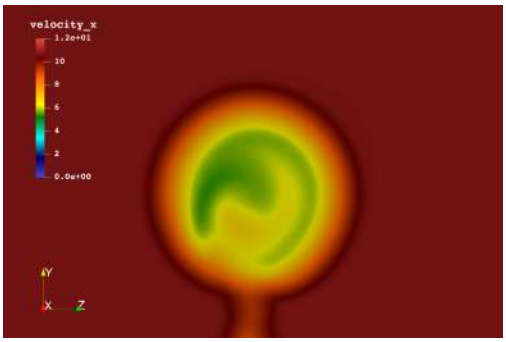

(e) Velocity contours at 5 D downstream.

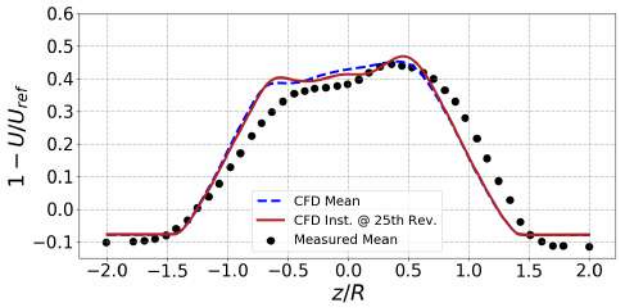

(f) Instantaneous deficit profiles at 5 D downstream.

Figure 6.18: Instantaneous wake contours and profiles.

6.3 Chapter Summary

In this chapter, the CFD simulations were performed targeting the wake characteristics of the NTNU BT1 wind turbine by using ReFRESCO and FANS. The CFD predictions are compared against the experimental data and with the numerical results obtained from other representative methods. In general, it was found that the numerical predictions of the wake characteristics agreed with the experimental data well, while the challenges in predicting the turbulence levels were identified.

The total estimated computational resources consumed in the current study by using ReFRESCO and FANS are approximately 2.3 million and 200 thousand service units (SUs), respectively, funded by TAMU HPRC. For reference purposes, Table 6.8 compares the computational resources used in an individual ReFRESCO and a FANS simulation.

	No. Cells / Grid Points	**Cores**	**Appr. Computational Time**	SUs
	$[Million]$	[/]	$[Day]$	[/]
ReFRESCO	26.96	616	12	177,408
FANS	24.2	64	10	15,360

Table 6.8: Computational resources of a single case used in the CFD simulations targeting the wake characteristics of the NTNU BT1 wind turbine.

7. CFD SIMULATIONS OF THE NTNU BT2 EXPERIMENT

In this chapter, the CFD simulations of the NTNU BT2 experiment are performed by using ReFRESCO and FANS. The CFD results are presented and compared against the experimental data.

7.1 ReFRESCO Simulations

In this section, the CFD predictions of the NTNU BT2 experiment obtained by using ReFRESC are presented and discussed. Three operating conditions, i.e., test cases A, B, and C, in the experiment, are simulated and the CFD results are compared against the measurements.

7.1.1 Computational Domain and Grid Generation

The multi-block technique used in the grid generation of the NTNU BT1 simulations is adopted here for the BT2 simulations. The computational domain is decomposed into three separate domains: 1) the inner rotating domains which are two short cylinders containing the upstream and the downstream rotors, respectively; 2) the stationary outer domain which is generated to match the wind tunnel in the experiment. In the simulations, the inner rotating domains will rotate while the outer domain remains stationary. Those domains are connected by sliding interfaces through which the solution of a domain is extrapolated to pass the flow information to the neighboring domains.

An illustration of the computational domain is provided in Fig. 7.1. The coordinate system is defined as follows: the origin of the coordinate system is placed at the center of the downstream wind turbine, the positive $x - axis$ points from inlet to outlet and $y - axis$ from bottom to top, and the $z - axis$ is thus defined according to the right-hand rule.

For the wind turbine wall boundaries, including the blades, hub, nacelle, and tower, viscous layers are generated with the criterion of $y^+ < 1$, and the cell expansion ratio normal to the wall is 1.2. For the outer stationary block, the high resolution of the grid is maintained up to 4 diameters downstream of the downstream turbine, and further refinement was performed 1 diameter down-

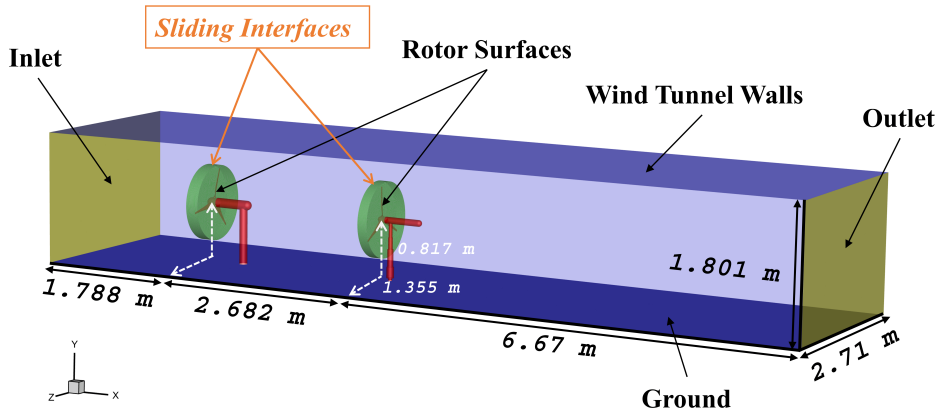

Figure 7.1: Computational domain for the BT2 simulations using ReFRESCO.

stream of both turbines. 7.2 shows the cross-sectional view of the generated computational grid. The total number of cells in the computational grid is 32.4 million.

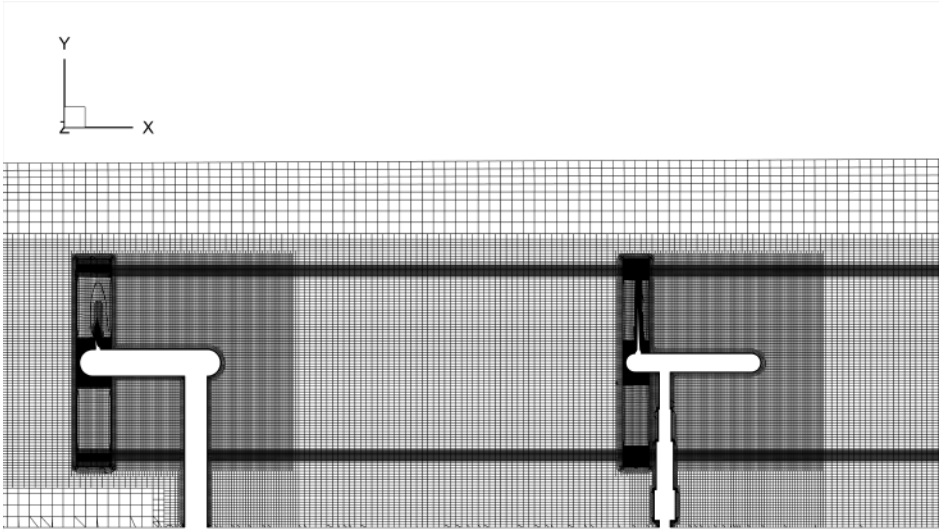

Figure 7.2: Computational grid for the BT2 simulations using ReFRESCO. View of the mesh on the xOy plane

7.1.2 Numerical Settings

The boundary conditions are set as follows. A uniform inflow velocity and turbulence intensity are specified at the inlet boundary, and the fixed pressure boundary condition is defined at the outlet boundary. The slip-wall boundary condition is applied to the four wind-tunnel side walls. The interfaces between the inner rotating and outer stationary regions are set as BCInterface in ReFRESCO, which allows the flow information to be transferred from one to another. Further, the no-slip condition is applied to the wind turbine surfaces including the blades, hubs, nacelles, and towers. The Implicit three-time-level scheme is used for the time marching.

For all the simulations in the present study, a uniform inflow wind velocity of 10 m/s and a turbulence intensity of 0.3% are used. The upstream turbine is operating at a TSR of 6, which will be denoted as $\lambda_1 = 6$, in all three test cases. The TSR values of the downstream turbine, λ_2, are 4.0, 7.0, and 2.5 in test cases A, B, and C, respectively.

7.1.3 CFD Results

7.1.3.1 Test Case A

In test case A, the value of TSR for the upstream turbine is $\lambda_1 = 6.0$, and for the downstream turbine is $\lambda_2 = 4.0$.

The normalized velocity (U/U_{ref}) and the turbulent fluctuation (u^2/U_{ref}^2) profiles at 1, 2.5, and 4 diameters (downstream turbine, denoted as D) behind the downstream turbine for test case A are shown in Fig. 7.3. The black dots are the measured time-averaged data in the experiment, and the red lines are the CFD-predicted profiles obtained from ReFRESCO simulations. It can be seen from the figure that, similar to the wake profiles in the BT1 experiment, the measured wake profiles, i.e., the mean wake velocity and turbulent kinetic energy profiles, in the BT2 experiment also exhibit asymmetry. As will be discussed later, the reason for the asymmetry of the wake in BT2 is the same as the reason for the asymmetry of the wake in BT1. It should also be noted here that the streamwise turbulent fluctuation, u^2, is calculated according to the original report [4] of

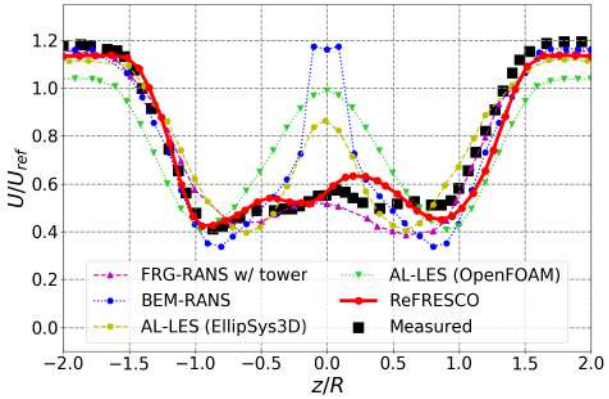

(a) Deficit profiles at 1 D downstream of the downstream turbine.

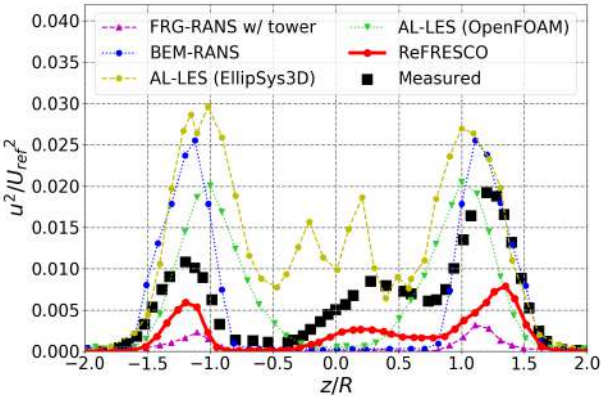

(b) Fluctuation profiles at 1 D downstream of the downstream turbine.

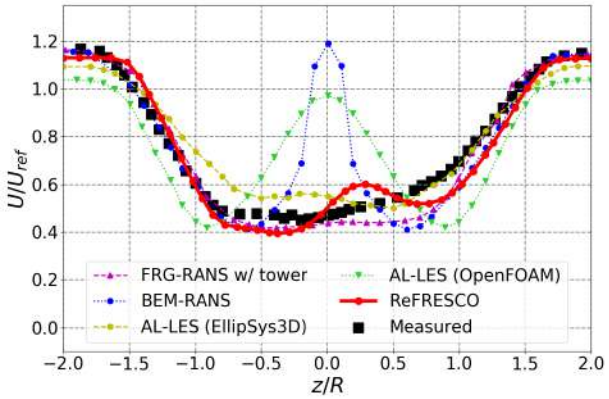

(c) Deficit profiles at 2.5 D downstream of the downstream turbine.

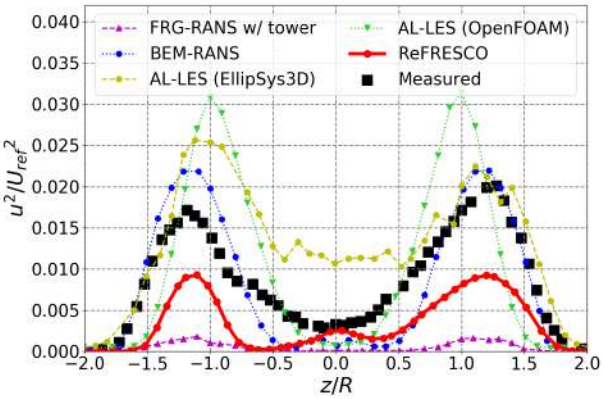

(d) Fluctuation profiles at 2.5 D downstream of the downstream turbine.

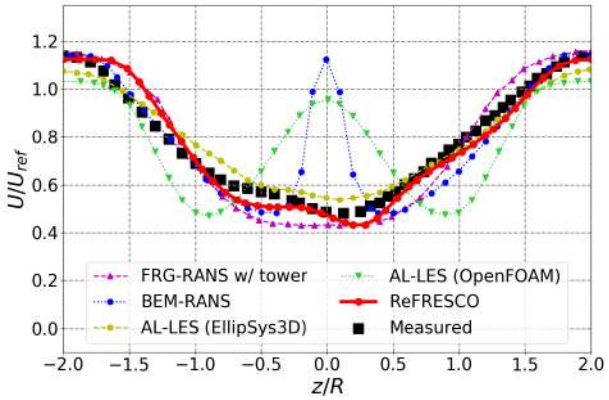

(e) Deficit profiles at 4 D downstream of the downstream turbine.

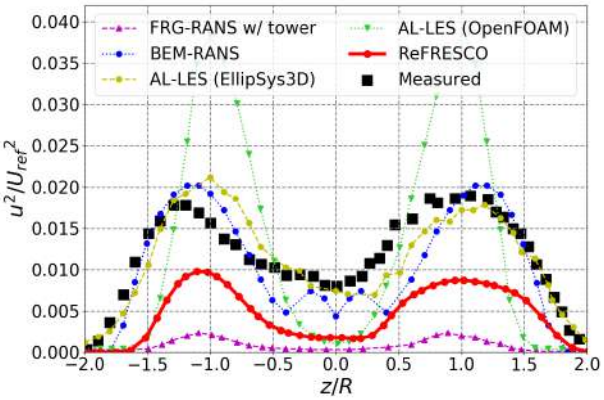

(f) Fluctuation profiles at 4 D downstream of the downstream turbine.

Figure 7.3: Comparison of mean wake velocity and turbulent fluctuation profiles of the NTNU BT2 test case A.

the NTNU BT2 workshop by using the following equation:

$$k \simeq 3u^2/2 \tag{7.1}$$

For comparison purposes, results using other representative modeling approaches reported by Pierella et al. [4] and Sreenivas et al. [91] are also presented here. The details of the different numerical methods are summarized in Table 7.1.

Numerical Results	**Rotor**	**Tower**	**Gov. Eq.**	**Turb. Closure**	**CFD Solver**
FRG-RANS w/ tower [4]	FRG	Yes	RANS	$k-\omega$ SST	Ansys Fluent
BEM-RANS[4]	BEM	No	RANS	Reynolds Stress Closure	Ansys Fluent
AL-LES [4]	AL	No	LES	Sub-grid	EllipSys3D
AL-LES [4]	AL	No	LES	Sub-grid	OpenFOAM
Sreenivas et al. (2016)	FRG	Yes	DES	SST-DES	Tenasi

Table 7.1: Details of the different numerical methods compared in the BT2 simulations. The numerical methods adopted by the participants are denoted as: 1) FRG-RANS w/ tower - RANS calculations using fully-resolved rotor geometry including the tower; 2) BEM-RANS - RANS simulations in which the rotor is modeled by the blade-element method and no nacelle or tower effect were included; and 3) AL-LES - LES simulations in which the rotor is modeled by the actuator line method and no nacelle or tower effect were included. Note that for AL-LES, two results obtained from two different solvers are presented here, i.e., EllipSys3D and OpenFOAM.

At 1 D downstream, as shown in Figs. 7.3a and 7.3b, the ReFRESCO-predicted mean velocity and fluctuation profiles match the experimental data well.

In the wake velocity profile, as shown in Fig. 7.3a, the asymmetry in the velocity profile is successfully captured in the present simulations. The two local maximums in the measured velocity profile, i.e., at approximately $z/R = +0.1$ and $z/R = -0.5$, are captured by the ReFRESCO simulation, while their locations slightly deviate in the numerical predictions. The profile marked as "FRG-RANS w/ tower" also predicts an asymmetry mean velocity profile and matches the measurement well, but it only captures one local maximum while the ReFRESCO result captures two. For other methods, i.e., BEM-LES, AL-LES (EllipSys3D), and AL-LES (OpenFOAM), the re-

sults are symmetric. Further, they all significantly over-predicted the velocity profile in the middle section, and thus the details of the predicted profiles in the range of $-1.0 < z/R < 1.0$ are not physically correct.

In the fluctuation profile, as shown in Fig. 7.3b, the asymmetry of the profile is obtained in the simulation. Although the present result in general under-predicts the magnitude, the shape characteristics in the profile of the experimental measurement are well reproduced. On the contrary, the other three results, i.e., BEM-LES, AL-LES (EllipSys3D), and AL-LES (OpenFOAM), all predict a higher turbulence level, while the shape characteristics in the experimental measurement are not well captured. In addition, for the result labeled as "FRG-RANS w/ tower", although it uses the same numerical framework as the present study, its predicted turbulence level is significantly lower than the measurement and the ReFRESCO prediction.

Similarly, for the velocity profiles, as shown in Figs. 7.3c and 7.3e, at 2.5 D and 4 D downstream, the ReFRESCO predictions match the experimental data well in general. It is also worth pointing out that in Fig. 7.3c, there is an over-prediction of velocity in the ReFRESCO result in the range of $0 < z/R < +0.5$, while the measurement in that range appears smoother. By comparing with the profile at 1 D downstream, i.e., Fig. 7.3a, it seems that the velocity profile was smoothed quicker in the experiment. And this is reasonable due to the fact that lower turbulence levels were obtained in the current simulations with two-equation turbulence models and thus the turbulence mixing in the wake region is lower compared to the experiment.

For the fluctuation profiles, as shown in Figs. 7.3d and 7.3f, at 2.5 D and 4 D downstream, the ReFRESCO predictions match the experimental measurement in trend while under-predict the turbulence level in general. This under-prediction is, again, due to the behavior of the two-equation turbulence models.

Fig. 7.4 shows the flow field of test case A in the ReFRESCO simulations. The velocity contours on the yOx plane are shown in Fig. 7.4a, and the Q iso-surfaces colored by streamwise velocity are utilized to show the vortex structures of the flow, as shown in Fig. 7.4b. It can be observed from the figures that the tip vortices generated by the upstream wind turbine are clear

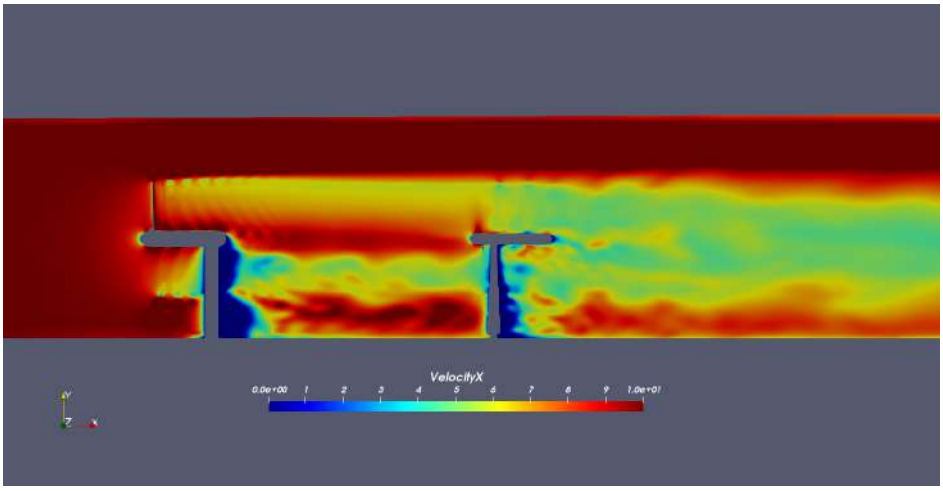

(a) Velocity contours on the yOx plane.

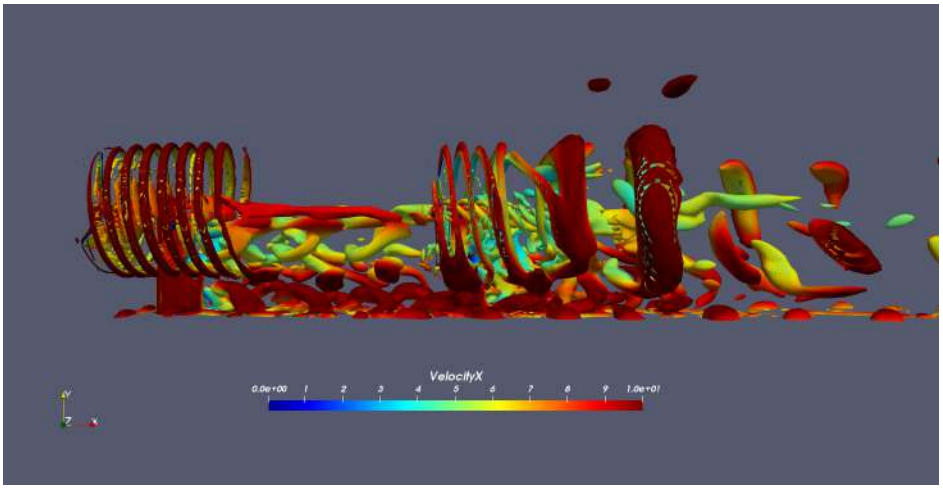

(b) Iso-surfaces of $Q = 1000$, colored by streamwise velocity.

Figure 7.4: Flow field visualization of test case A obtained by ReFRESCO.

and stable. In contrast, the tip vortex structure behind the downstream wind turbine can only be identified within a relatively shorter downstream distance and soon become chaotic due to the interaction with the wake of the upstream turbine.

7.1.3.2 Test Case B

In test case B, the TSR value for the upstream turbine is $\lambda_1 = 6.0$, and for the downstream turbine, it is $\lambda_2 = 7.0$.

The velocity and the turbulent fluctuation profiles at 1, 2.5, and 4 D behind the downstream

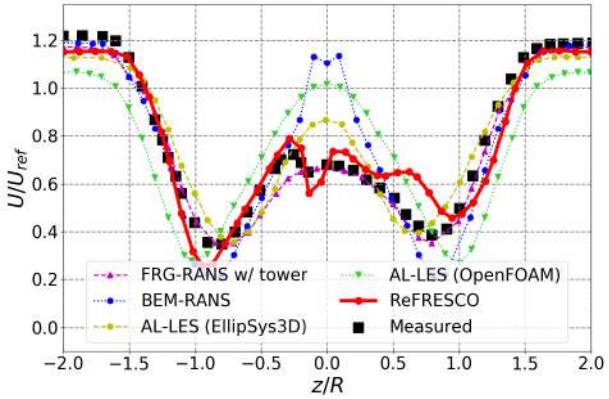

(a) Deficit profiles at 1 D downstream of the downstream turbine.

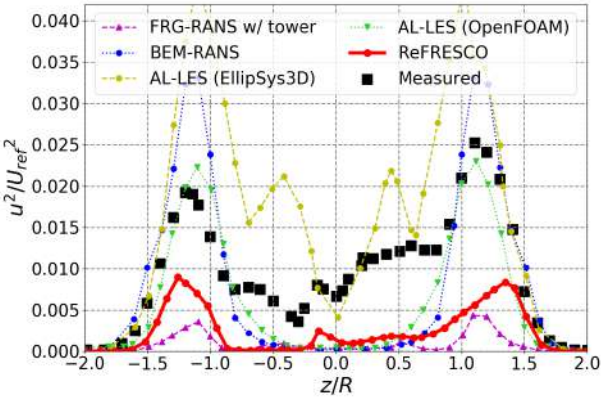

(b) Fluctuation profiles at 1 D downstream of the downstream turbine.

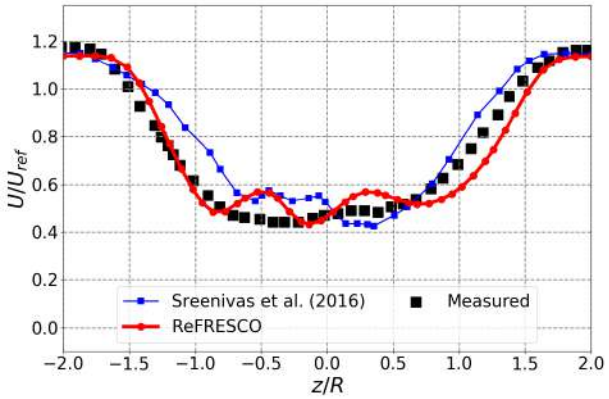

(c) Deficit profiles at 2.5 D downstream of the downstream turbine.

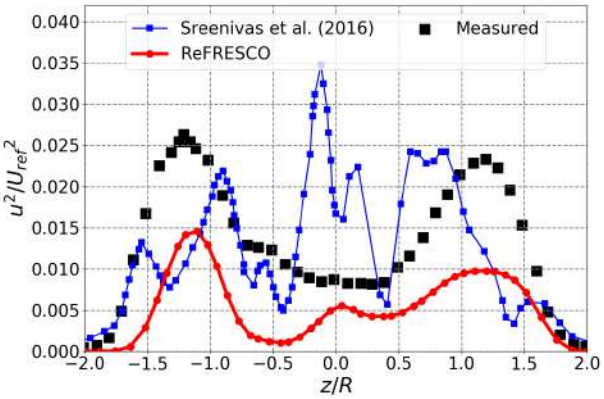

(d) Fluctuation profiles at 2.5 D downstream of the downstream turbine.

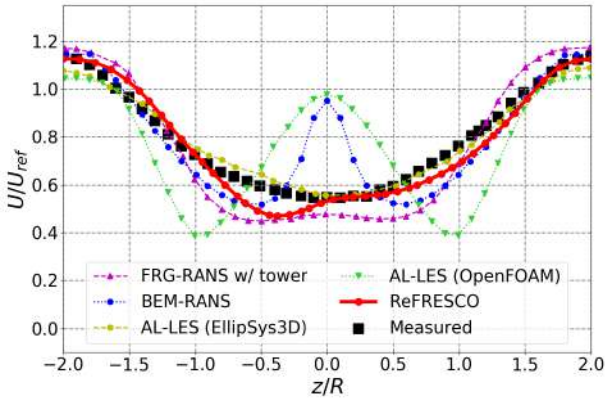

(e) Deficit profiles at 4 D downstream of the downstream turbine.

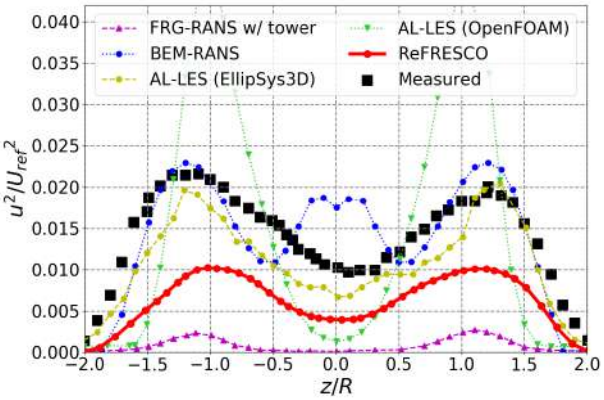

(f) Fluctuation profiles at 4 D downstream of the downstream turbine.

Figure 7.5: Comparison of mean wake velocity and turbulent fluctuation profiles of the NTNU BT2 test case B.

turbine for test case B are shown in Fig. 7.5. The black dots are the measured time-averaged data in the experiment, and the red lines are the ReFRESCO-predicted profiles obtained from simulations. Similar to test case A, results using other representative modeling approaches reported by Pierella et al. [4] are also presented here, i.e. FRG-RANS w/ tower, BEM-LES, AL-LES (EllipSys3D) and AL-LES (OpenFOAM). It should be mentioned that the wake profiles at 2.5 D downstream were not provided in the original report [4], therefore, the results presented by Sreenivas et al. [91] are adopted here for comparison purposes.

For the velocity profiles at 1 D, 2.5 D and 4 D downstream, as shown in Figs. 7.5a, 7.5c, and 7.5e, respectively, the ReFRESCO predictions match the experimental measurement well in general. The results obtained from "FRG-RANS w/ tower" also predict asymmetry mean velocity profiles and match the measurement well. For other methods, i.e., BEM-LES, AL-LES (EllipSys3D), and AL-LES (OpenFOAM), the results are symmetric. This highlights the importance of modeling tower and nacelle structures in the CFD simulations of wind turbines.

For the fluctuation profiles at 1 D, 2.5 D, and 4 D downstream, as shown in Figs. 7.5b, 7.5d, and 7.5f, respectively, the ReFRESCO predictions match the experimental measurement well in trend while under-predict the magnitude. Similar to the results in test case A, although the present results in general under-predict the magnitudes, the shape characteristics in the profile of the experimental measurement are well captured. As a comparison, all the other results did not predict the shape characteristics in the experimental measurement correctly. Also, as discussed in test case A, for the results labeled as "FRG-RANS w/ tower", although it uses the same numerical framework as the present study, its predicted turbulence level is significantly lower than the measurement and the ReFRESCO prediction.

Fig. 7.6 shows the flow field of test case B in the ReFRESCO simulations. The velocity contours on the yOx plane are shown in Fig. 7.6a, and the Q iso-surfaces colored by streamwise velocity are utilized to show the vortex structures of the flow, as shown in Fig. 7.6b. It can be observed from the figures that the tip vortices generated by the upstream wind turbine are clear and stable. Just like in test case A, the tip vortex structure behind the downstream wind turbine in test

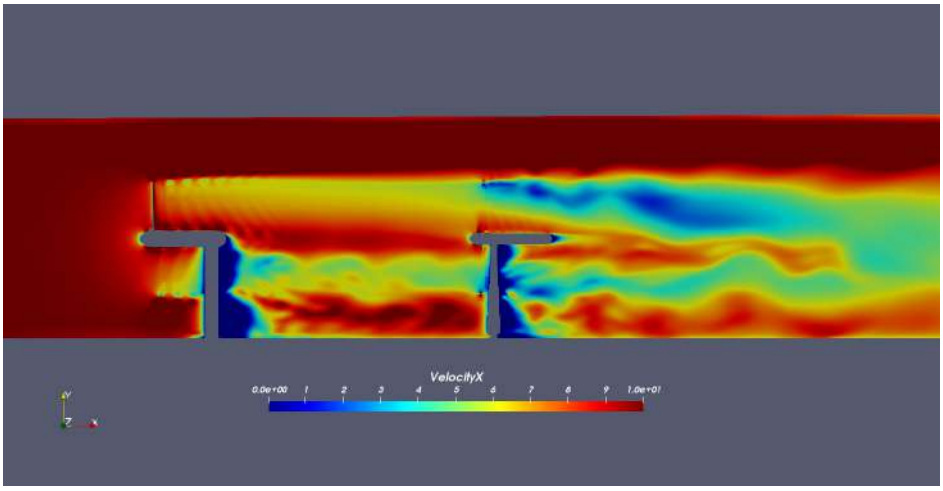

(a) Velocity contours on the yOx plane.

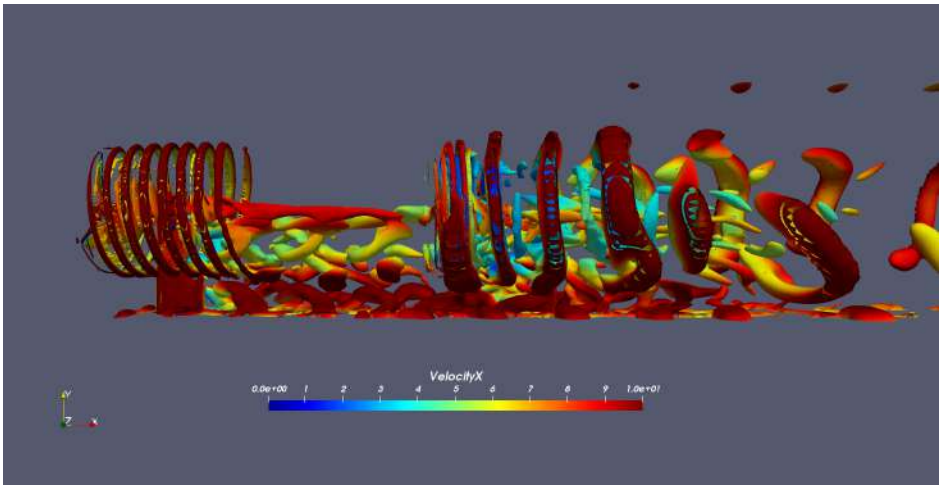

(b) Iso-surfaces of $Q = 1000$, colored by streamwise velocity.

Figure 7.6: Flow field visualization of test case B obtained by ReFRESCO.

case B can only be maintained in a relatively short downstream distance and soon become chaotic due to the interaction with the wake of the upstream turbine.

7.1.3.3 Test Case C

In test case C, the value of TSR for the upstream turbine is $\lambda_1 = 6.0$, and for the downstream turbine is $\lambda_2 = 2.5$.

The velocity and the fluctuation profiles at 1, 2.5, and 4 D behind the downstream turbine for test case C are shown in Fig. 7.7. The black dots are the measured time-averaged data in the ex-

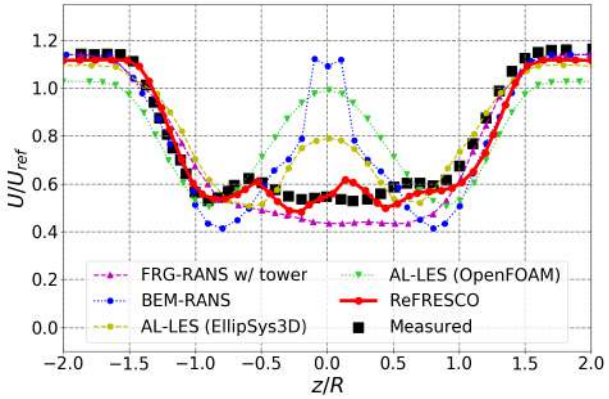

(a) Deficit profiles at 1 D downstream of the downstream turbine.

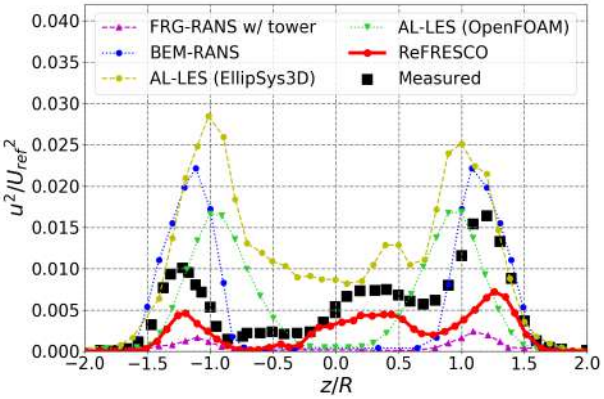

(b) Fluctuation profiles at 1 D downstream of the downstream turbine.

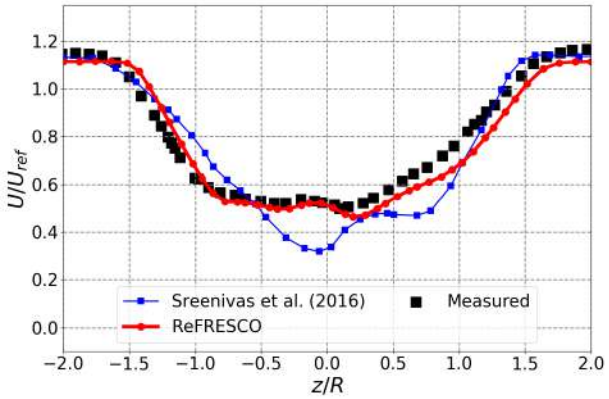

(c) Deficit profiles at 2.5 D downstream of the downstream turbine.

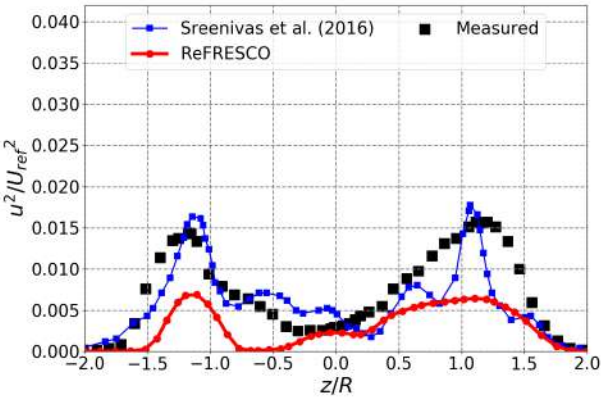

(d) Fluctuation profiles at 2.5 D downstream of the downstream turbine.

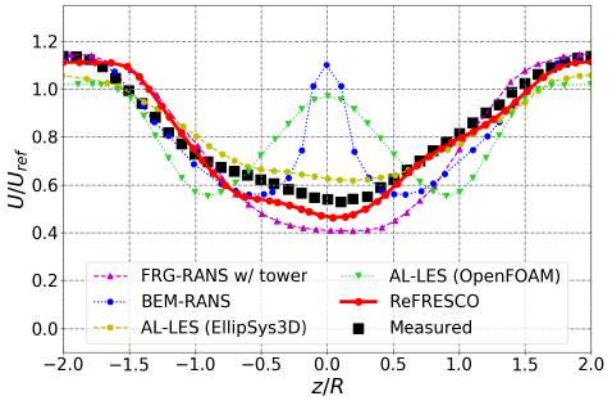

(e) Deficit profiles at 4 D downstream of the downstream turbine.

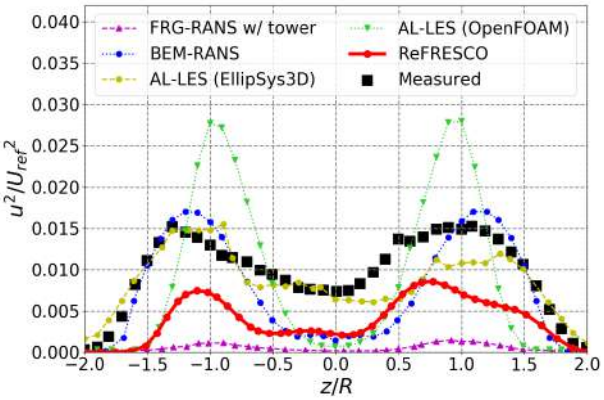

(f) Fluctuation profiles at 4 D downstream of the downstream turbine.

Figure 7.7: Comparison of mean wake velocity and turbulent fluctuation profiles of the NTNU BT2 test case C.

periment, and the red lines are the CFD-predicted profiles obtained from ReFRESCO simulations. Similar to test cases A and B, results using other representative modeling approaches reported by Pierella et al. [4] are also presented here, i.e. FRG-RANS w/ tower, BEM-LES, AL-LES (EllipSys3D) and AL-LES (OpenFOAM). Again, it should be mentioned that the wake profiles at 2.5 D downstream were not provided in the original report [4], therefore, the results presented by Sreenivas et al. [91] are adopted here for comparison purposes.

For the velocity profiles at 1 D, 2.5 D, and 4 D downstream, as shown in Figs. 7.7a, 7.7c, and 7.7e, respectively, the ReFRESCO predictions match the experimental measurement well in general.

The results obtained from "FRG-RANS w/ tower" also predict asymmetry mean velocity profiles and match the measurement well. For other methods, i.e., BEM-LES, AL-LES (EllipSys3D), and AL-LES (OpenFOAM), the results are symmetric and all have an over-prediction in the middle of the wake profiles. Again, this highlights the importance of modeling the tower and nacelle in wind turbine simulations.

For the fluctuation profiles at 1 D, 2.5 D, and 4 D downstream, as shown in Figs. 7.7b, 7.7d, and 7.7f, respectively, the ReFRESCO predictions match the experimental measurement well in trend while, again, under-predict its magnitude. Similar to the results in test cases A and B, although the present results in general under-predict the magnitudes, the shape characteristics in the profile of the experimental measurement are well captured. As a comparison, all the other results did not predict the shape characteristics in the experimental measurement correctly. Also, as discussed in test cases A and B, for the results labeled as "FRG-RANS w/ tower", although it uses the same numerical framework as the present study, its predicted turbulence level is significantly lower than the measurement and the ReFRESCO prediction.

Fig. 7.8 shows the flow field of test case C in the ReFRESCO simulations. The velocity contours on the yOx plane are shown in Fig. 7.8a, and the Q iso-surfaces colored by streamwise velocity are utilized to show the vortex structures of the flow, as shown in Fig. 7.8b. Again, like in test cases A and B, the tip vortices generated by the upstream wind turbine are clear and stable.

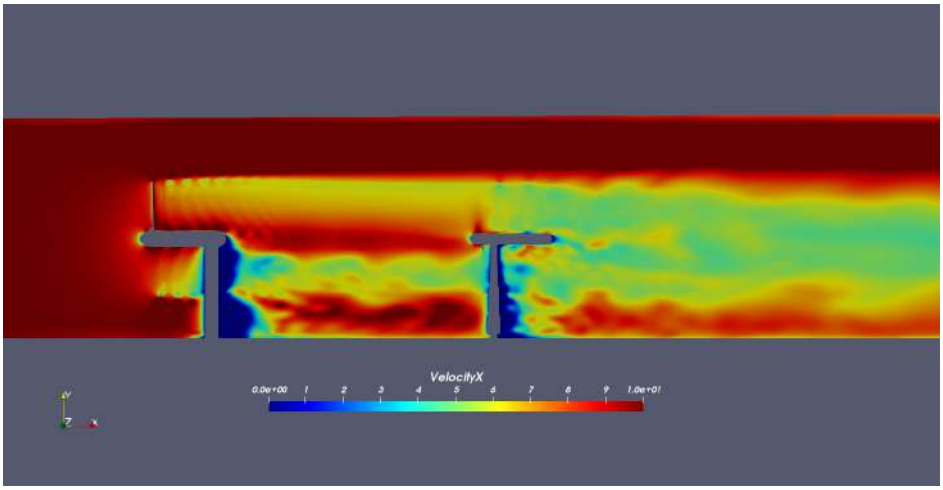

(a) Velocity contours on the yOx plane.

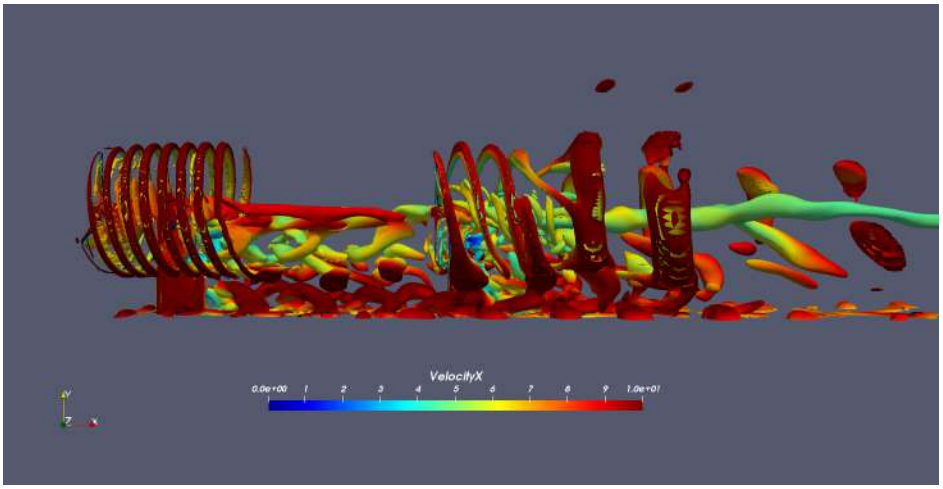

(b) Iso-surfaces of $Q = 1000$, colored by streamwise velocity.

Figure 7.8: Flow field visualization of test case C obtained by ReFRESCO.

For the tip vortex structure behind the downstream wind turbine, the flow field becomes unstable soon due to the interaction with the wake of the upstream turbine.

7.2 FANS Simulations

In this section, CFD simulations are performed for the NTNU BT2 experiment by using FANS. First, the computational domain and the grid generation are described and the numerical settings used in the simulations are introduced. Then, the numerical results for test case A of the NTNU BT2 experiment are presented and discussed.

The CFD simulations for this study using FANS are performed on the Grace cluster of the HPRC at TAMU with the Intel Xeon E5-2680 v4 2.40 GHz 14-core processors. 64 cores are used for the simulations and the computational time is roughly 15 days for a single run. More details of the consumed computational resources will be given in Section 7.3.

7.2.1 Computational Domain and Grid Generation

The computational domain used in the FANS simulations is illustrated in Fig. 7.9. The size of the computational domain is the same as the one used in the ReFRESCO simulations, therefore, for the sake of brevity, no repeated introductions will be provided here.

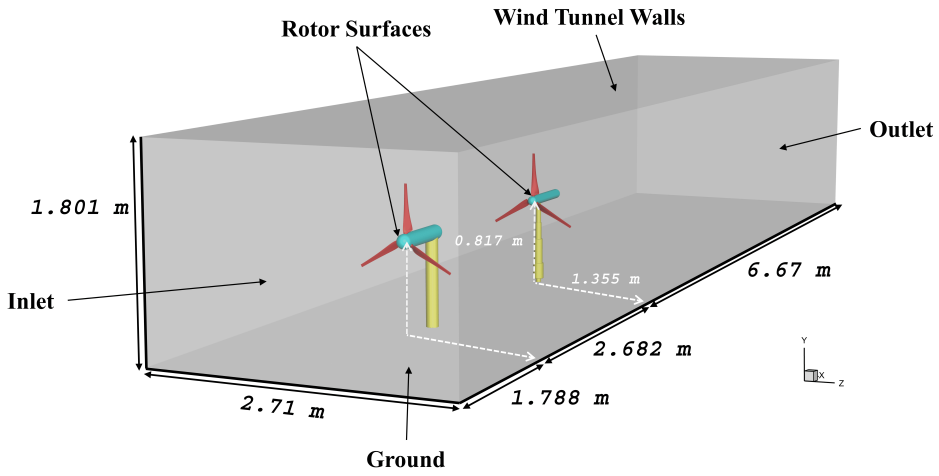

Figure 7.9: Computational domain for the BT2 simulations using FANS.

Structured overset grid blocks are then generated in the computational domain for the FANS simulations. For the current simulations of the NTNU BT2 experiment, in total 142 grid blocks were generated including 11 phantom blocks for hole-cutting purposes. As a result, the total number of grid points in the grid is 32.5 million. To get a better idea of the structure of the computational grid, an overview of the computational grid and the grid blocks covering the surfaces of the two wind turbines are shown in Fig. 7.10. The coordinate system is defined as follows: the origin of the coordinate system is placed at the center of the downstream wind turbine, the positive

$x - axis$ points from inlet to outlet and $y - axis$ from bottom to top, and the $z - axis$ is thus defined according to the right-hand rule.

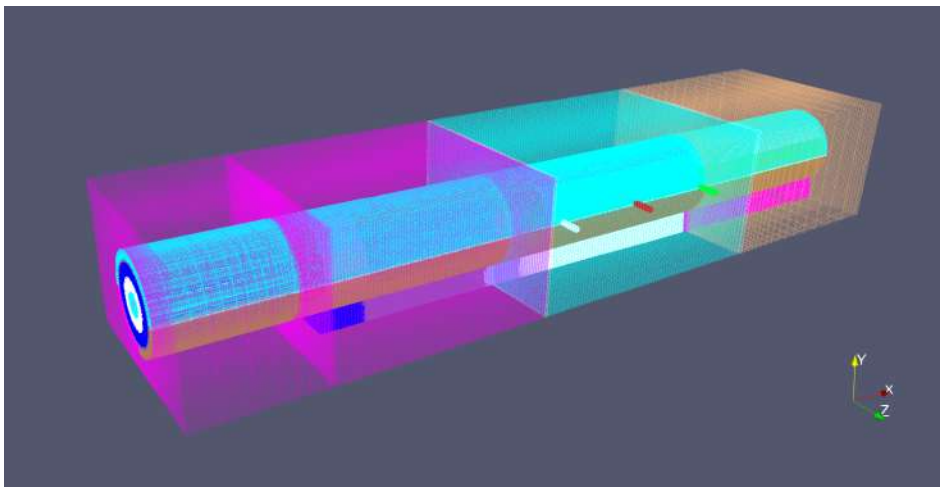

(a) Overview of the overset grid blocks used in the FANS simulations of the current study.

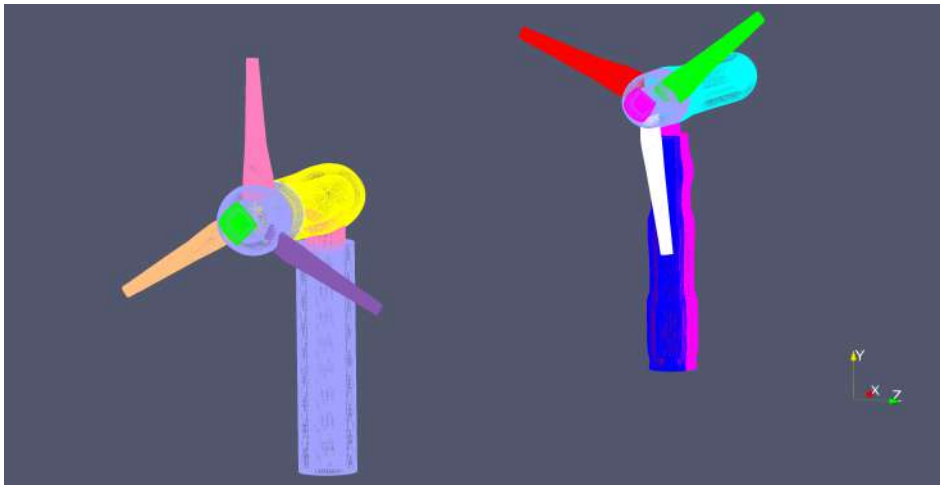

(b) Grid blocks covering the surfaces of the two wind turbines.

Figure 7.10: Computational grid generated for the FANS simulations of the NTNU BT2 experiment.

7.2.2 Numerical Settings

A uniform inflow is specified at the inlet, and the linear-extrapolation boundary condition in FANS is specified at the outlet. No-slip condition is applied to the surfaces of the two wind turbines including blades, hubs, nacelles, and towers. For the wind tunnel walls, a slip-wall condition is used. The boundary conditions for the surfaces of overset grid blocks that overlap with other blocks are set to "interior boundary surfaces". Interpolation will be performed using the flow information from the donor grids. The two-layer $k-\epsilon$ turbulence model is adopted for the turbulence closure, as described in 2.3.2. In test case A, the value of TSR for the upstream turbine is $\lambda_1 = 6.0$, and for the downstream turbine is $\lambda_2 = 4.0$. The temporal spacing is chosen such that in every time step the upstream wind turbine will rotate 3°.

7.2.3 CFD Results

The normalized velocity (U/U_{ref}) and the turbulent fluctuation (u^2/U_{ref}^2) profiles at 1, 2.5, and 4 D behind the downstream turbine for test case A are shown in Fig. 7.11. The black dots are the measured time-averaged data in the experiment, and the blue lines are the mean velocity profile obtained from FANS simulations. For comparison purposes, results using other representative modeling approaches reported by Pierella et al. [4] are also presented here including the ReFRESCO results obtained previously. The details of the different numerical results are listed in Table 7.1.

For the velocity profiles at 1 D, 2.5 D, and 4 D downstream, as shown in Figs. 7.11a, 7.11c, and 7.11e, respectively, the FANS predictions match the experimental measurement well in general. However, for the fluctuation profiles at 1 D, 2.5 D, and 4 D downstream, as shown in Figs. 7.11b, 7.11d, and 7.11f, respectively, the FANS results significantly under-predict the turbulent kinetic energy levels. The turbulence levels predicted by FANS are similar to the ReFRESCO results as shown in the figure.

Fig. 7.12 shows the iso-surfaces of Q and the iso-surfaces are presented in wire fires. Different colors in the figure indicate different overset blocks. It can be observed that the surfaces are

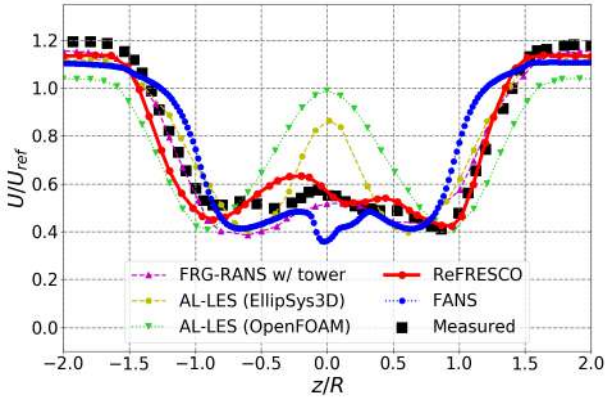

(a) Deficit profiles at 1 D downstream of the downstream turbine.

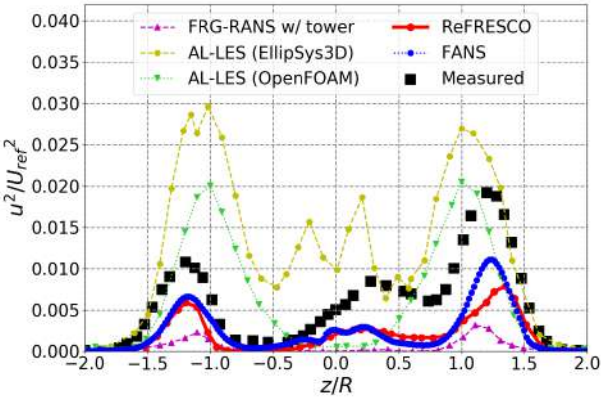

(b) Fluctuation profiles at 1 D downstream of the downstream turbine.

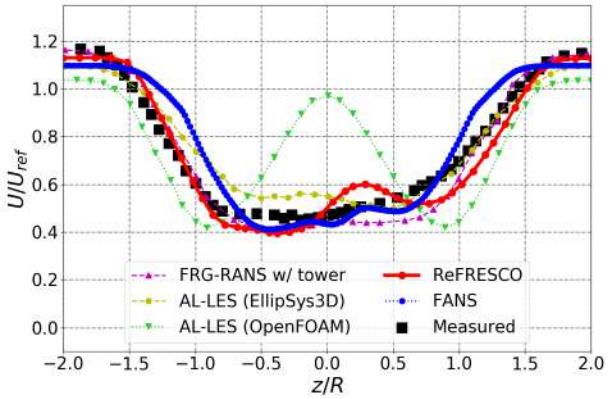

(c) Deficit profiles at 2.5 D downstream of the downstream turbine.

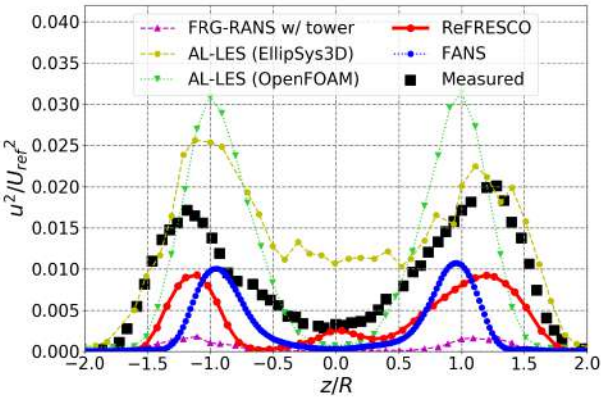

(d) Fluctuation profiles at 2.5 D downstream of the downstream turbine.

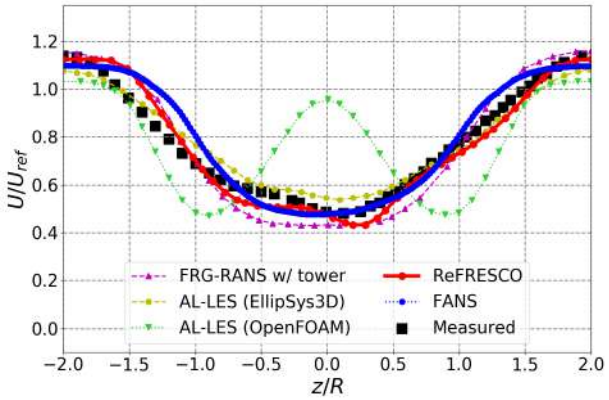

(e) Deficit profiles at 4 D downstream of the downstream turbine.

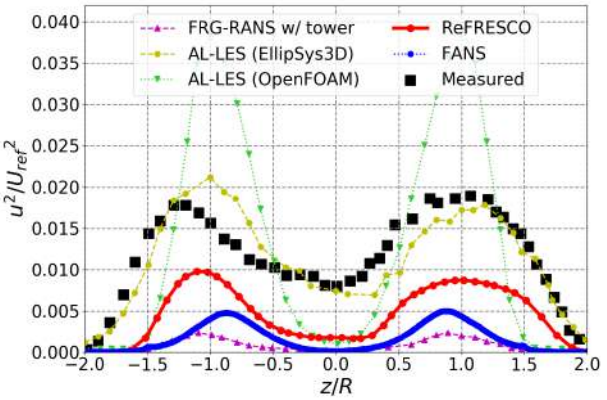

(f) Fluctuation profiles at 4 D downstream of the downstream turbine.

Figure 7.11: Comparison of the mean wake velocity and turbulent fluctuation profiles of the NTNU BT2 test case A.

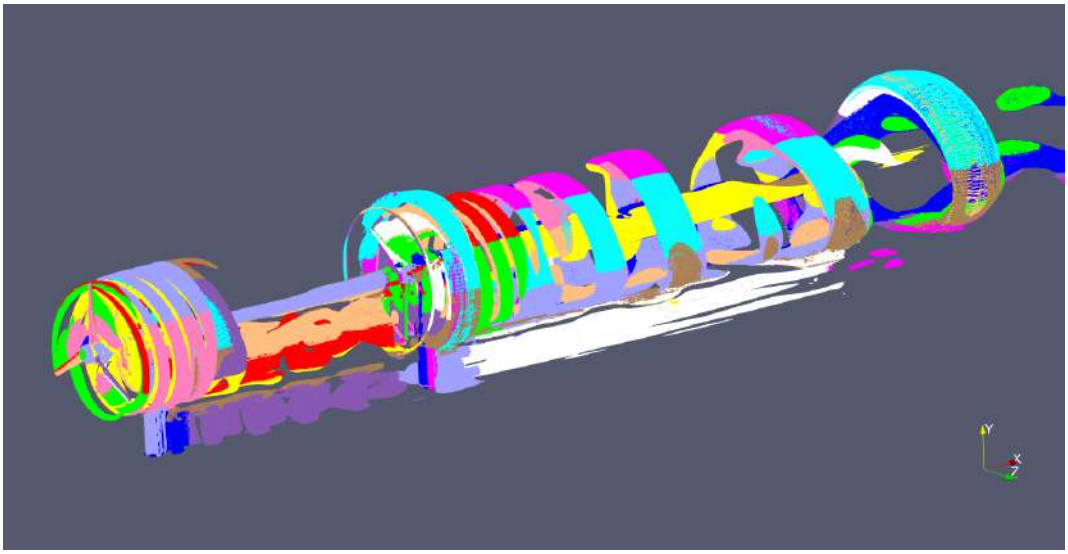

Figure 7.12: Iso-surfaces of Q shown in wire fire. Different colors indicate different overset grid blocks.

continual and smooth which confirms the interpolation of flow information among different overset grid blocks is correctly performed by the interpolation routine in FANS.

Fig. 7.13 shows the flow field of test case A in the FANS simulations. The velocity contours on the yOx plane is shown in Fig. 7.13b, and the Q iso-surfaces colored by streamwise velocity are utilized to show the vortex structures of the flow, as shown in Fig. 7.13a. It can be observed from the figures that the tip vortices generated by the upstream wind turbine are clear and stable. In contrast, the tip vortex structure behind the downstream wind turbine can only be identified within a relatively shorter downstream distance and soon become chaotic due to the interaction with the wake of the upstream turbine.

7.3 Chapter Summary

In this chapter, the CFD simulations were performed for the NTNU BT2 experiment by using ReFRESCO and FANS. The CFD predictions are compared against the experimental data and with the numerical results obtained from other representative methods. In general, it was found that the numerical predictions of the wake characteristics agreed with the experimental data in trend. For the turbulence levels in the wake, the CFD predicted values are significantly lower than the

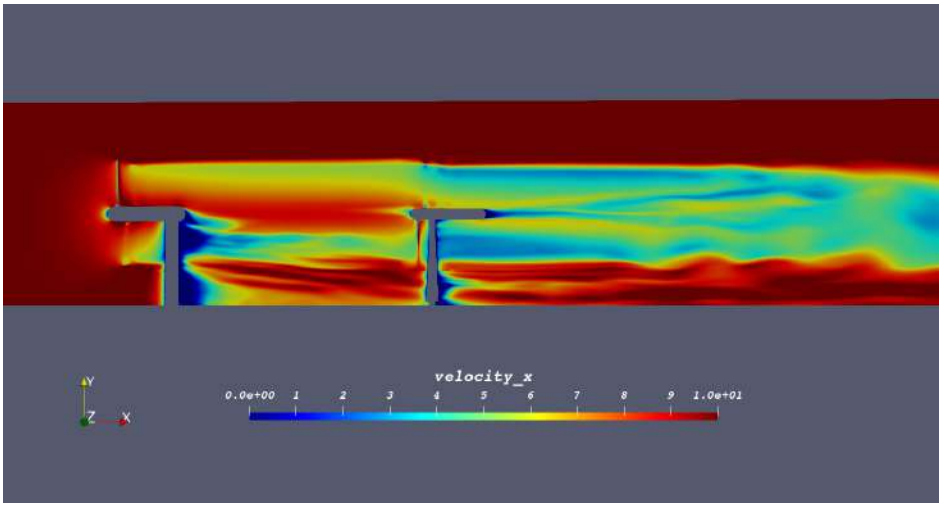

(a) Velocity contours on the yOx plane.

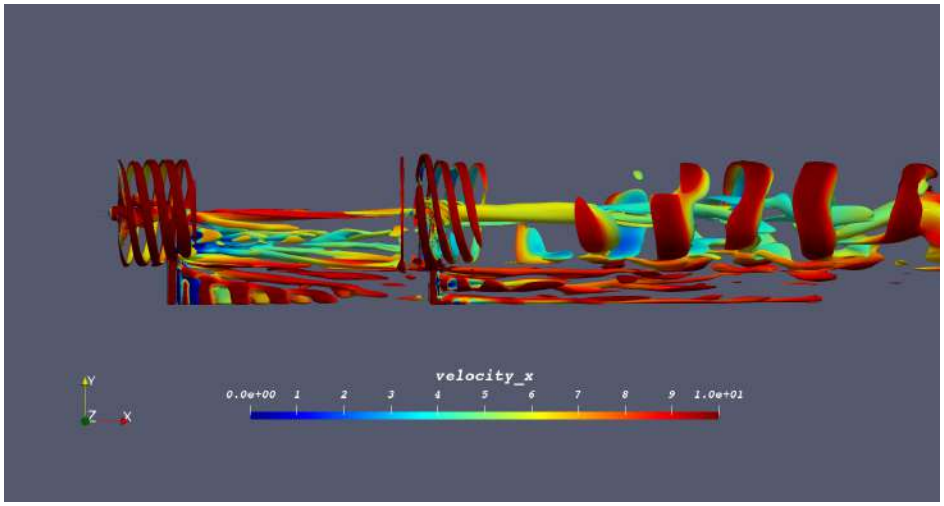

(b) Iso-surfaces of $Q = 1000$, colored by streamwise velocity.

Figure 7.13: Flow field visualization of test case A obtained by FANS.

measurement. However, this is expected due to the limitations of two-equation turbulence closure models.

The total estimated computational resources consumed in the current study by using ReFRESCO and FANS are approximately 800 thousand and 300 thousand service units (SUs), respectively, funded by TAMU HPRC. For reference purposes, Table 7.2 compares the computational resources used in an individual ReFRESCO and a FANS simulation.

	No. Cells / Grid Points	**Cores**	**Appr. Computational Time**	SUs
	$[Million]$	[/]	$[Day]$	[/]
ReFRESCO	32.4	616	16	236,544
FANS	32.5	64	15	23,040

Table 7.2: Computational resources of selected cases used in the CFD simulations of the NTNU BT2 experiment.

8. SUMMARY AND CONCLUSIONS

8.1 Summary and Conclusions

In this dissertation, high-fidelity numerical simulations were performed for the NREL S826, NTNU BT1, and NTNU BT2 experiments by using two CFD codes, i.e., ReFRESCO and FANS.

Because the NTNU BT1 and BT2 wind turbine blades were constructed by utilizing the NREL S826 airfoil along the entire span, as a benchmark case, CFD simulations were first performed for the NREL S826 airfoil by using the two adopted CFD codes. By comparing the pressure distribution on the S826 airfoil obtained from simulations against the measured data at different angles of attack, it was demonstrated that the two CFD codes used in the current study were capable of accurately predicting the pressure distribution on the surface of the airfoil.

Then, CFD simulations were performed targeting the performance of the NTNU BT1 wind turbine by using the two CFD codes. A systematic verification and validation study was performed to quantify the numerical uncertainties in the simulations. Specifically, to quantify the numerical uncertainty relating to the spatial and temporal discretization errors, a novel verification procedure was applied to the CFD predictions. In the ReFRESCO simulations, a simulation matrix consisting of four systematically refined grids combined with four different time increments is established for the verification study. Results from the 16 cases were presented and discussed in detail. The effect of the selection of the data sets used in the verification study on the estimation of the numerical uncertainties was also investigated. According to the investigation, a verification study using 12 cases was proposed. The final numerical uncertainties for C_T and C_P calculated by ReFRESCO were 7.3% and 9.4%, respectively. In the FANS simulations, a simulation matrix with 6 cases was established, and final numerical uncertainties for C_T and C_P calculated by FANS were 7.3% and 8.1%, respectively. In general, the CFD-predicted performance of the NTNU BT1 wind turbine was in good agreement with the experimental measurements. From the extensive study of the numerical uncertainties in the simulations of the NTNU BT1 wind turbine, the following conclusions

can be drawn:

- The verification study for both spatial and temporal resolution is crucial to the wind turbine simulations. Plausible results could be obtained from CFD simulations by using completely incorrect pairs of grid and time spacings.

- The power coefficient C_P tends to be more significantly affected in the grid-refinement process of ReFRESCO simulations. This is an indication that for the unstructured grid used in ReFRESCO when the global grid resolution decreases, the geometry of the tip region may not be accurately captured. In FANS simulations, however, body-fitted structured meshes were generated and thus the tip region was accurately resolved in all the grids. As a result, no sudden variations in the values of C_P were observed when changing the grid resolution in the current study.

Afterward, unsteady RANS calculations with fully resolved turbine geometries were performed aiming at the wake characteristics of the NTNU BT1 wind turbine by using ReFRESCO and FANS. In ReFRESCO simulations, a systematic verification procedure is performed first to estimate the numerical uncertainties in the predicted wake characteristics. A simulation matrix consisting of three systematically refined grids coupled with three different time increments is established. Results from the 9 cases were presented and discussed in detail. The asymmetry peaks in the deficit profiles were identified and selected as the metric to quantify the discretization uncertainties. For FANS simulations, the verification procedure is omitted and calculations were performed directly with the knowledge learned in the previous simulations. The CFD-predicted wake characteristics of the NTNU BT1 wind turbine were then compared against the experimental data. In general, good agreement between the prediction and the measurement was achieved and the numerical results were validated. The predictions were also compared with the results obtained by other representative modeling approaches. It was shown that the asymmetry in the deficit profiles was successfully captured in the present study, whereas all other approaches predicted symmetric deficit profiles. From the discussions, the following conclusion can be drawn:

- The asymmetry of the deficit profiles is caused by the rotating blade wakes and the skew of the tower wake, and the location-switch phenomenon of the asymmetry peaks is owing to the rotation of the blade wakes.

- The asymmetry in the wake profiles is physical and it is not a measurement error as discussed and suspected in some previous studies [6].

- The RANS equations coupled with the $k-\omega$ SST or the two-layer $k-\epsilon$ turbulence model adopted in the current study is capable of capturing the asymmetry in the wake characteristics of the BT1 turbine.

- Both the ReFRESCO and FANS results, under-predicted the TKE levels in certain regions, and it was concluded that the discrepancies between the present predictions and the measured data are owing to the limitations of the 2-equation turbulence models which assume the production of TKE is isotropic. Although differences in magnitudes between the predictions and the measurements were found in the TKE profiles, the numerical results match the experimental data in trend.

Finally, CFD simulations were performed by using ReFRESCO and FANS for the NTNU BT2 experiment in which two turbines were operating in tandem. In ReFRESCO simulations, three test cases were analyzed. The CFD-predicted wake characteristics were compared to the measurement. It was found that the velocity profiles at different downstream distances for the three test cases were in reasonable agreement with the experimental data, while the turbulence levels obtained from the CFD simulations were considerably lower. The same conclusion can be made for the FANS predictions, in which the predicted velocity profiles matched the experimental measurements better than the turbulence levels.

8.2 Recommendations for Future Research

Based on the results and discussions in the current work, the following recommendations are proposed for future research focusing on the CFD simulations of the performance and wake char-

acteristics of floating offshore wind turbines (FOWT):

- The two-equation models used in the current study are based on isotropic turbulence assumptions. However, the wake of a wind turbine is highly non-isotropic in the real world. Ideally, large-eddy simulations with fully resolved turbine geometries should be performed. However, at least in the near future, this is not practical due to the limitations on computational resources. Therefore, bridging models, e.g., the Reynolds-Stress Closure Models in the RANS framework or the Partially-Averaged Navier-Stokes models, are recommended to be implemented in the CFD simulations to improve turbulence predictions.

- The multi-scale nature of the wind turbine flows makes it extremely challenging to resolve all the desired flow details in numerical simulations. Simplifications either for the rotating blades or for the far wake are necessary for real-dimension simulations. However, the currently existing simplified models are questioned to be implemented into the simulations aiming at FOWT, in which the turbines will experience additional six-degrees-of-freedom motions. Therefore, it is recommended to generate surrogate artificial intelligence models using machine learning techniques that represent the responses and near-field flow characteristics of FOWTs based on high-fidelity CFD simulations. Those models can be then coupled with LES solvers to investigate the flows within onshore or offshore wind farms.

REFERENCES

[1] C. Steiness, Wake turbulence in horns rev offshore wind farm, denmark, http://i.imgur.com/qruVcnu.jpg (2008).

[2] J. Bartl, K. F. Sagmo, T. Bracchi, L. Sætran, Performance of the nrel s826 airfoil at low to moderate reynolds numbers—a reference experiment for cfd models, European Journal of Mechanics-B/Fluids 75 (2019) 180–192.

[3] P.-Å. Krogstad, P. E. Eriksen, "blind test" calculations of the performance and wake development for a model wind turbine, Renewable energy 50 (2013) 325–333.

[4] F. Pierella, P.-Å. Krogstad, L. Sætran, Blind test 2 calculations for two in-line model wind turbines where the downstream turbine operates at various rotational speeds, Renewable Energy 70 (2014) 62–77.

[5] P.-Å. Krogstad, J. Lund, An experimental and numerical study of the performance of a model turbine, Wind Energy 15 (2012) 443–457.

[6] R. Ji, K. Sun, J. Zhang, R. Zhu, S. Wang, A novel actuator line-immersed boundary (al-ib) hybrid approach for wake characteristics prediction of a horizontal-axis wind turbine, Energy Conversion and Management 253 (2022) 115193.

[7] P. Veers, K. Dykes, E. Lantz, S. Barth, C. L. Bottasso, O. Carlson, A. Clifton, J. Green, P. Green, H. Holttinen, et al., Grand challenges in the science of wind energy, Science 366 (2019) eaau2027.

[8] B. J. Vanderwende, B. Kosović, J. K. Lundquist, J. D. Mirocha, Simulating effects of a wind-turbine array using les and rans, Journal of Advances in Modeling Earth Systems 8 (2016) 1376–1390.

[9] Y.-T. Wu, F. Porté-Agel, Modeling turbine wakes and power losses within a wind farm using les: An application to the horns rev offshore wind farm, Renewable Energy 75 (2015) 945–955.

[10] D. Willis, C. Niezrecki, D. Kuchma, E. Hines, S. Arwade, R. Barthelmie, M. DiPaola,

P. Drane, C. Hansen, M. Inalpolat, et al., Wind energy research: State-of-the-art and future research directions, Renewable Energy 125 (2018) 133–154.

[11] G. Van Kuik, J. Peinke, R. Nijssen, D. Lekou, J. Mann, J. N. Sørensen, C. Ferreira, J.-W. van Wingerden, D. Schlipf, P. Gebraad, et al., Long-term research challenges in wind energy–a research agenda by the european academy of wind energy, Wind energy science 1 (2016) 1–39.

[12] E. Simley, N. Angelou, T. Mikkelsen, M. Sjöholm, J. Mann, L. Y. Pao, Characterization of wind velocities in the upstream induction zone of a wind turbine using scanning continuous-wave lidars, Journal of Renewable and Sustainable Energy 8 (2016) 013301.

[13] B. Sanderse, S. Van der Pijl, B. Koren, Review of computational fluid dynamics for wind turbine wake aerodynamics, Wind energy 14 (2011) 799–819.

[14] F. Porté-Agel, M. Bastankhah, S. Shamsoddin, Wind-turbine and wind-farm flows: a review, Boundary-Layer Meteorology 174 (2020) 1–59.

[15] S.-P. Breton, J. Sumner, J. N. Sørensen, K. S. Hansen, S. Sarmast, S. Ivanell, A survey of modelling methods for high-fidelity wind farm simulations using large eddy simulation, Philosophical Transactions of the Royal Society A: Mathematical, Physical and Engineering Sciences 375 (2017) 20160097.

[16] J. Thé, H. Yu, A critical review on the simulations of wind turbine aerodynamics focusing on hybrid rans-les methods, Energy 138 (2017) 257–289.

[17] J. N. Sørensen, A. Myken, Unsteady actuator disc model for horizontal axis wind turbines, Journal of Wind Engineering and Industrial Aerodynamics 39 (1992) 139–149.

[18] J. N. Sørensen, K. Nilsson, S. Ivanell, H. Asmuth, R. F. Mikkelsen, Analytical body forces in numerical actuator disc model of wind turbines, Renewable Energy 147 (2020) 2259–2271.

[19] J. N. Sorensen, W. Z. Shen, Numerical modeling of wind turbine wakes, J. Fluids Eng. 124 (2002) 393–399.

[20] W. Z. Shen, J. N. Sørensen, R. Mikkelsen, Tip loss correction for actuator/navier–stokes

computations, J. Sol. Energy Eng. 127 (2005) 209–213.

[21] N. Troldborg, Actuator line modeling of wind turbine wakes, Ph.D. thesis, Technical University of Denmark, 2009.

[22] J. Feliciano, G. Cortina, A. Spear, M. Calaf, Generalized analytical displacement model for wind turbine towers under aerodynamic loading, Journal of Wind Engineering and Industrial Aerodynamics 176 (2018) 120–130.

[23] M. Draper, A. Guggeri, M. Mendina, G. Usera, F. Campagnolo, A large eddy simulation-actuator line model framework to simulate a scaled wind energy facility and its application, Journal of Wind Engineering and Industrial Aerodynamics 182 (2018) 146–159.

[24] W. Tian, K. Zheng, H. Hu, Investigation of the wake propagation behind wind turbines over hilly terrain with different slope gradients, Journal of Wind Engineering and Industrial Aerodynamics 215 (2021) 104683.

[25] R. Zhang, Z. Xin, G. Huang, B. Yan, X. Zhou, X. Deng, Characteristics and modelling of wake for aligned multiple turbines based on numerical simulation, Journal of Wind Engineering and Industrial Aerodynamics 228 (2022) 105097.

[26] M. Calaf, C. Meneveau, J. Meyers, Large eddy simulation study of fully developed wind-turbine array boundary layers, Physics of fluids 22 (2010) 015110.

[27] D. Mehta, A. Van Zuijlen, B. Koren, J. Holierhoek, H. Bijl, Large eddy simulation of wind farm aerodynamics: A review, Journal of Wind Engineering and Industrial Aerodynamics 133 (2014) 1–17.

[28] K. Nilsson, S. Ivanell, K. S. Hansen, R. Mikkelsen, J. N. Sørensen, S.-P. Breton, D. Henningson, Large-eddy simulations of the lillgrund wind farm, Wind Energy 18 (2015) 449–467.

[29] M. Shives, C. Crawford, Adapted two-equation turbulence closures for actuator disk rans simulations of wind & tidal turbine wakes, Renewable Energy 92 (2016) 273–292.

[30] D. Micallef, T. Sant, Loading effects on floating offshore horizontal axis wind turbines in surge motion, Renewable Energy 83 (2015) 737–748.

[31] S. Lee, M. Churchfield, F. Driscoll, S. Sirnivas, J. Jonkman, P. Moriarty, B. Skaare, F. G. Nielsen, E. Byklum, Load estimation of offshore wind turbines, Energies 11 (2018) 1895.

[32] H. Johlas, L. A. Martínez-Tossas, D. Schmidt, M. Lackner, M. J. Churchfield, Large eddy simulations of floating offshore wind turbine wakes with coupled platform motion, in: Journal of Physics: Conference Series, volume 1256, IOP Publishing, 2019, p. 012018.

[33] M. J. Churchfield, S. Lee, J. Michalakes, P. J. Moriarty, A numerical study of the effects of atmospheric and wake turbulence on wind turbine dynamics, Journal of turbulence (2012) N14.

[34] S.-P. Breton, K. Nilsson, H. Olivares-Espinosa, C. Masson, L. Dufresne, S. Ivanell, Study of the influence of imposed turbulence on the asymptotic wake deficit in a very long line of wind turbines, Renewable energy 70 (2014) 153–163.

[35] N. S. Ghaisas, C. L. Archer, S. Xie, S. Wu, E. Maguire, Evaluation of layout and atmospheric stability effects in wind farms using large-eddy simulation, Wind Energy 20 (2017) 1227–1240.

[36] S. Xie, C. L. Archer, A numerical study of wind-turbine wakes for three atmospheric stability conditions, Boundary-Layer Meteorology 165 (2017) 87–112.

[37] G. Cortina, V. Sharma, R. Torres, M. Calaf, Mean kinetic energy distribution in finite-size wind farms: A function of turbines' arrangement, Renewable Energy 148 (2020) 585–599.

[38] L. Tian, Y. Song, N. Zhao, W. Shen, C. Zhu, T. Wang, Effects of turbulence modelling in ad/rans simulations of single wind & tidal turbine wakes and double wake interactions, Energy 208 (2020) 118440.

[39] C. Santoni, K. Carrasquillo, I. Arenas-Navarro, S. Leonardi, Effect of tower and nacelle on the flow past a wind turbine, Wind Energy 20 (2017) 1927–1939.

[40] E. Duque, C. Van Dam, S. Hughes, Navier-stokes simulations of the nrel combined experiment phase ii rotor, in: 37th Aerospace Sciences Meeting and Exhibit, 1999, p. 37.

[41] T. T. Tran, D.-H. Kim, A cfd study into the influence of unsteady aerodynamic interference on wind turbine surge motion, Renewable Energy 90 (2016) 204–228.

[42] B. Wen, Z. Li, Z. Jiang, Z. Peng, X. Dong, X. Tian, Experimental study on the tower loading characteristics of a floating wind turbine based on wave basin model tests, Journal of Wind Engineering and Industrial Aerodynamics 207 (2020) 104390.

[43] N. Sorensen, M. Hansen, Rotor performance predictions using a navier-stokes method, in: 1998 ASME wind energy symposium, 1998, p. 25.

[44] M. Potsdam, D. Mavriplis, Unstructured mesh cfd aerodynamic analysis of the nrel phase vi rotor, in: 47th AIAA Aerospace Sciences Meeting Including The New Horizons Forum and Aerospace Exposition, 2009, p. 1221.

[45] Y. Bazilevs, M.-C. Hsu, I. Akkerman, S. Wright, K. Takizawa, B. Henicke, T. Spielman, T. Tezduyar, 3d simulation of wind turbine rotors at full scale. part i: Geometry modeling and aerodynamics, International journal for numerical methods in fluids 65 (2011) 207–235.

[46] Y. Bazilevs, M.-C. Hsu, J. Kiendl, R. Wüchner, K.-U. Bletzinger, 3d simulation of wind turbine rotors at full scale. part ii: Fluid–structure interaction modeling with composite blades, International Journal for numerical methods in fluids 65 (2011) 236–253.

[47] J.-O. Mo, A. Choudhry, M. Arjomandi, Y.-H. Lee, Large eddy simulation of the wind turbine wake characteristics in the numerical wind tunnel model, Journal of Wind Engineering and Industrial Aerodynamics 112 (2013) 11–24.

[48] M. Make, G. Vaz, Analyzing scaling effects on offshore wind turbines using cfd, Renewable Energy 83 (2015) 1326–1340.

[49] A. C. Aranake, V. K. Lakshminarayan, K. Duraisamy, Computational analysis of shrouded wind turbine configurations using a 3-dimensional rans solver, Renewable Energy 75 (2015) 818–832.

[50] S. Quallen, T. Xing, An investigation of the blade tower interaction of a floating offshore wind turbine, in: The Twenty-fifth International Ocean and Polar Engineering Conference, OnePetro, 2015.

[51] X. Cai, R. Gu, P. Pan, J. Zhu, Unsteady aerodynamics simulation of a full-scale horizontal axis wind turbine using cfd methodology, Energy Conversion and Management 112 (2016)

146–156.

[52] M. Ye, H.-C. Chen, A. Koop, Cfd simulations of a performance-scaled wind turbine, Ocean Systems Engineering 12 (2022) 247–265.

[53] H. Kim, S. Lee, S. Lee, Influence of blade-tower interaction in upwind-type horizontal axis wind turbines on aerodynamics, Journal of Mechanical Science and Technology 25 (2011) 1351–1360.

[54] M.-C. Hsu, Y. Bazilevs, Fluid–structure interaction modeling of wind turbines: simulating the full machine, Computational Mechanics 50 (2012) 821–833.

[55] H. Schümann, F. Pierella, L. Sætran, Experimental investigation of wind turbine wakes in the wind tunnel, Energy Procedia 35 (2013) 285–296.

[56] F. Pierella, L. Sætran, Wind tunnel investigation on the effect of the turbine tower on wind turbines wake symmetry, Wind Energy 20 (2017) 1753–1769.

[57] A. Abraham, T. Dasari, J. Hong, Effect of turbine nacelle and tower on the near wake of a utility-scale wind turbine, Journal of Wind Engineering and Industrial Aerodynamics 193 (2019) 103981.

[58] A. Gómez, J. R. Seume, Aerodynamic coupling of rotor and tower in hawts, in: Proceedings of the European Wind Energy Conference, volume 6, Citeseer, 2009.

[59] S. G. Horcas, F. Debrabandere, B. Tartinville, C. Hirsch, G. Coussement, Rotor-tower interactions of dtu 10mw reference wind turbine with a non-linear harmonic method, Wind Energy 20 (2017) 619–636.

[60] L. Ma, P.-L. Delafin, P. Tsoutsanis, A. Antoniadis, T. Nishino, Blade-resolved cfd simulations of a periodic array of nrel 5 mw rotors with and without towers, Wind 2 (2022) 51–67.

[61] I. Janajreh, I. Talab, J. Macpherson, Numerical simulation of tower rotor interaction for downwind wind turbine, Modelling and simulation in engineering 2010 (2010).

[62] B. Dose, H. Rahimi, B. Stoevesandt, J. Peinke, Fluid-structure coupled investigations of the nrel 5 mw wind turbine for two downwind configurations, Renewable Energy 146 (2020)

1113–1123.

[63] F. Zahle, N. N. Sørensen, J. Johansen, Wind turbine rotor-tower interaction using an incompressible overset grid method, Wind Energy: An International Journal for Progress and Applications in Wind Power Conversion Technology 12 (2009) 594–619.

[64] Y. Li, K.-J. Paik, T. Xing, P. M. Carrica, Dynamic overset cfd simulations of wind turbine aerodynamics, Renewable Energy 37 (2012) 285–298.

[65] C. Lynch, M. Smith, Unstructured overset incompressible computational fluid dynamics for unsteady wind turbine simulations, Wind Energy 16 (2013) 1033–1048.

[66] Y. Liu, Q. Xiao, A. Incecik, C. Peyrard, D. Wan, Establishing a fully coupled cfd analysis tool for floating offshore wind turbines, Renewable Energy 112 (2017) 280–301.

[67] L. Lin, K. Wang, D. Vassalos, Detecting wake performance of floating offshore wind turbine, Ocean Engineering 156 (2018) 263–276.

[68] Y. Liu, Q. Xiao, Development of a fully coupled aero-hydro-mooring-elastic tool for floating offshore wind turbines, Journal of Hydrodynamics 31 (2019) 21–33.

[69] Y. Fang, L. Duan, Z. Han, Y. Zhao, H. Yang, Numerical analysis of aerodynamic performance of a floating offshore wind turbine under pitch motion, Energy 192 (2020) 116621.

[70] T. Toan Tran, D.-H. Kim, B. Hieu Nguyen, Aerodynamic interference effect of huge wind turbine blades with periodic surge motions using overset grid-based computational fluid dynamics approach, Journal of Solar Energy Engineering 137 (2015).

[71] T. T. Tran, D.-H. Kim, Fully coupled aero-hydrodynamic analysis of a semi-submersible fowt using a dynamic fluid body interaction approach, Renewable energy 92 (2016) 244–261.

[72] H. C. Chen, V. C. Patel, S. Ju, Solutions of reynolds-averaged navier-stokes equations for three-dimensional incompressible flows, Journal of Computational Physics 88 (1990) 305–336.

[73] J. Pontaza, H. Chen, J. Reddy, A local-analytic-based discretization procedure for the numerical solution of incompressible flows, International Journal for Numerical Methods in

Fluids 49 (2005) 657–699.

[74] C.-J. Chen, H.-C. Chen, Finite analytic numerical method for unsteady two-dimensional navier-stokes equations, Journal of Computational Physics 53 (1984) 209–226.

[75] F. R. Menter, M. Kuntz, R. Langtry, Ten years of industrial experience with the sst turbulence model, Turbulence, heat and mass transfer 4 (2003) 625–632.

[76] H. Chen, V. Patel, Near-wall turbulence models for complex flows including separation, AIAA journal 26 (1988) 641–648.

[77] B. E. Launder, B. I. Sharma, Application of the energy-dissipation model of turbulence to the calculation of flow near a spinning disc, Letters in heat and mass transfer 1 (1974) 131–137.

[78] B. E. Launder, D. B. Spalding, The numerical computation of turbulent flows, in: Numerical prediction of flow, heat transfer, turbulence and combustion, Elsevier, 1983, pp. 96–116.

[79] L. Eça, M. Hoekstra, A procedure for the estimation of the numerical uncertainty of cfd calculations based on grid refinement studies, Journal of computational physics 262 (2014) 104–130.

[80] P. J. Roache, Fundamentals of verification and validation, hermosa publ., 2009.

[81] L. Eça, G. Vaz, S. Toxopeus, M. Hoekstra, Numerical errors in unsteady flow simulations, Journal of Verification, Validation and Uncertainty Quantification 4 (2019).

[82] H. W. Coleman, F. Stern, Uncertainties and cfd code validation (1997).

[83] S. Zeoli, G. Balarac, P. Bénard, G. Georis, F. Houtin-Mongrolle, L. Bricteux, Large eddy simulation of wind turbine wakes using adaptative mesh refinement, in: Journal of Physics: Conference Series, volume 1618, IOP Publishing, 2020, p. 062056.

[84] G. De Cillis, S. Cherubini, O. Semeraro, S. Leonardi, P. De Palma, Stability and optimal forcing analysis of a wind turbine wake: Comparison with pod, Renewable Energy 181 (2022) 765–785.

[85] Y. Qian, T. Wang, Y. Yuan, Y. Zhang, Comparative study on wind turbine wakes using a modified partially-averaged navier-stokes method and large eddy simulation, Energy 206

(2020) 118147.

[86] A. Mittal, K. Sreenivas, L. K. Taylor, L. Hereth, C. B. Hilbert, Blade-resolved simulations of a model wind turbine: effect of temporal convergence, Wind Energy 19 (2016) 1761–1783.

[87] M. Ye, H.-C. Chen, A. Koop, Comparison of different wind turbine modeling strategies in cfd simulations, in: The 32st International Ocean and Polar Engineering Conference, OnePetro, 2022, pp. 396–403.

[88] L. Oggiano, Cfd simulations on the ntnu wind turbine rotor and comparison with experiments, Energy Procedia 58 (2014) 111–116.

[89] M. S. Siddiqui, A. Rasheed, T. Kvamsdal, M. Tabib, Influence of tip speed ratio on wake flow characteristics utilizing fully resolved cfd methodology, in: Journal of Physics: Conference Series, volume 854, IOP Publishing, 2017, p. 012043.

[90] M. S. Siddiqui, T. Kvamsdal, A. Rasheed, High fidelity computational fluid dynamics assessment of wind tunnel turbine test, in: Journal of Physics: Conference Series, volume 1356, IOP Publishing, 2019, p. 012044.

[91] K. Sreenivas, A. Mittal, L. Hereth, L. K. Taylor, C. B. Hilbert, Numerical simulation of the interaction between tandem wind turbines, Journal of Wind Engineering and Industrial Aerodynamics 157 (2016) 145–157.

[92] A. A. Veisi, M. H. S. Mayam, Effects of blade rotation direction in the wake region of two in-line turbines using large eddy simulation, Applied Energy 197 (2017) 375–392.

[93] X. Duan, J. Wang, D. Wan, Cfd investigations of wake flow interactions in a wind farm with 14 wind turbines, International Journal of Offshore and Polar Engineering 30 (2020) 257–265.

[94] B. Van Leer, Towards the ultimate conservative difference scheme. ii. monotonicity and conservation combined in a second-order scheme, Journal of computational physics 14 (1974) 361–370.

[95] C. Klaij, M. Hoekstra, G. Vaz, Design, analysis and verification of a volume-of-fluid model with interface-capturing scheme, Computers & Fluids 170 (2018) 324–340.

[96] Y. Wang, H.-C. Chen, A. Koop, G. Vaz, Verification and validation of cfd simulations for semi-submersible floating offshore wind turbine under pitch free-decay motion, Ocean Engineering 242 (2021) 109993.

[97] M. Ye, H.-C. Chen, A. Koop, Verification study for cfd simulations of ntnu blind test 1 wind turbine, in: The 32st International Ocean and Polar Engineering Conference, OnePetro, 2022, pp. 275–281.

[98] MARIN, ReFRESCO Theory Manual V2.4.0, Technical Report, Maritime Research Institute Netherlands (MARIN), Wageningen, The Netherlands, 2017.

[99] J. C. Hunt, A. A. Wray, P. Moin, Eddies, streams, and convergence zones in turbulent flows, Studying turbulence using numerical simulation databases, 2. Proceedings of the 1988 summer program (1988).

[100] S. J. Kamkar, A. Jameson, A. M. Wissink, V. Sankaran, Feature-driven cartesian adaptive mesh refinement in the helios code, in: 48th AIAA Aerosciences Conference, 2010, pp. 2010–0171.

[101] J. F. Manwell, J. G. McGowan, A. L. Rogers, Wind energy explained: theory, design and application, John Wiley & Sons, 2010.